Effects of Solar Hybridization on the Performance of a Gas Turbine

by
Christiaan Homann

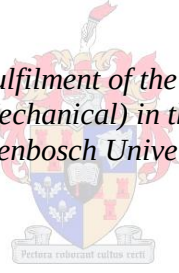

Thesis presented in partial fulfilment of the requirements for the degree of Master of Engineering (Mechanical) in the Faculty of Engineering at Stellenbosch University

Supervisor: Dr. S.J. van der Spuy
Co-supervisor: Prof. T.W. von Backström

December 2015

Declaration

By submitting this thesis electronically, I declare that the entirety of the work contained therein is my own, original work, that I am the sole author thereof (save to the extent explicitly otherwise stated), that reproduction and publication thereof by Stellenbosch University will not infringe any third party rights and that I have not previously, in its entirety or in part, submitted it for obtaining any qualification.

Date: 31 August 2015

Abstract

This study investigates the effect of the solarization of a gas turbine on its performance and details the integration of this gas turbine into a solar power plant.

A Rover 1S/60 gas turbine (Rover, 1966), rated at 45 kW, was modelled in Flownex and validated against a one-dimensional thermodynamic model, at design input conditions. The model of the gas turbine was adapted to incorporate different components of a CSP plant. The solar hybrid gas turbine (SHGT) model simulates the gas turbine performance when subjected to a typical variation in solar resource. A newly designed compressor for the Rover 1S/60 was integrated, both into the original Rover gas turbine model, as well as the SHGT model.

Heat addition due to solar irradiation resulted in a decreased fuel consumption rate and an increased thermal efficiency for the gas turbine. The net power output of the turbine, however, decreased as the solar irradiation increased. This is a consequence of the additional pressure drop over the solar receiver, directly affecting the power produced by the turbine. Results showed that installation of the new compressor could eliminate the adverse pressure effects of the solar components, if implemented.

To aid future experimental work, an interconnection component to direct air out of the Rover gas turbine into the solar receiver, was designed. The velocity and pressure profiles at two potential outlets from the main air casing were inspected by means of CFD simulations. The flow domain in the gas turbine was extracted, by reverse engineering the casing and relevant components. The inlet boundary conditions were adapted to evaluate both the original and the newly designed compressor.

Results at the combustor inlet (outlet 1), implementing the original compressor, compared relatively well to experimental test data. It was found, however, that the flow should rather be redirected to outlet 2 which is a previous modification made to the casing to implement a recuperator. The velocity and pressure flow profiles were more uniform at outlet 2, even when implementing the new compressor.

Two conceptual designs reintroducing the flow into the combustor were evaluated. The chosen concept significantly simplifies the implementation process by replacing the combustion chamber with in-line firing duct burners.

To determine whether SHGTs are feasible on a commercial scale, four industrial gas turbines were investigated. The aperture area required to achieve sufficient heat flux in the solar receiver, in order to replace the thermal energy from combustion, was determined and compared to commercial CSP tower plants, with similar power producing capabilities. Scalability of the gas turbines proved competitive, but the eventual success will depend on future improvements in pressurised air receivers.

Opsomming

Die studie wat volg ondersoek die effek van sonkrag-aanpassings op die werkverrigting van ‘n gasturbine en beskryf die integrasie van ‘n gasturbine in ‘n sonkragstasie.

‘n 45 kW Rover 1S/60 gasturbine is in die vloeinetwerkkode, Flownex, gemodelleer en is teenoor ‘n eendimensionele termodinamiese model by ontwerp invoer toestande gevalideer. Die gasturbine model is aangepas om verskillende komponente van ‘n konsentrerende sonkrag (KSK) stasie, soos ‘n son-ontvanger en heliostaatveld, te inkorporeer. Die aangepaste sonkrag gasturbine (SHGT) model simuleer die gasturbine werkverrigtinge wanneer dit aan ‘n tipiese variasie in son hulpbronne blootgestel word. ‘n Nuut-ontwerpte kompressor vir die Rover 1S/60 is in beide die oorspronklike Rover gasturbine-model en die SHGT model geïntegreer.

Warmte toevoeging weens sonbestraling het gelei tot ‘n afname in die brandstofverbruiks tempo en ‘n verhoogde termiese doeltreffendheid van die gasturbine. Die netto krag van die gasturbine het egter gedaal met die toenemende bydrae van sonkrag. Dit is as gevolg van die addisionele drukval oor die son-ontvanger, wat veroorsaak dat die krag wat deur die turbine geproduseer word afneem. Resultate het getoon dat die nuwe kompressor, indien geïmplementeer, die nadelige druk effekte van die sonkrag-komponente kan kanselleer.

‘n Komponent om lug uit die Rover gasturbine na die son-ontvanger te herlei, is ondersoek om toekomstige eksperimentele werk te steun. Die snelheids- en druk-profiele op twee potensiële uitlaatplekke vanuit die hoof lugomhulsel is deur middel van CFD simulasies geïnspekteer. Die vloeiprofiel deur die gasturbine is verkry deur terugwaartse-ontwikkeling van die omhulsel en relevante komponente. Die inlaat randvoorvaardes is aangepas om beide die oorspronklike en nuut-ontwerpte kompressor te evalueer.

Die resultate by die inlaat van die verbrandingsruim (uitlaat 1), gegewe die oorpronklike kompressor, vergelyk goed met die eksperimentele toets data. Daar is egter bevind dat die vloei eerder na uitlaat 2, ‘n vorige aanpassing aan die omhulsel om ‘n hitte-uitruiler te implementeer, herlei moet word. Die snelheid en druk vloei profiele is meer eenvormig by uitlaat 2, ook met die implementering van die nuwe kompressor.

Twee ontwerpe, wat die vloei in die verbrandingsruim herinvoer, is konseptueel geëvalueer. Die gekose konsep vereenvoudig die implementering van die proses aansienlik, deur die verbrandingskamer met in-lyn afvoer buis-branders te vervang.

Laastens is vier industriële gasturbines ondersoek om te bepaal of SHGT's uitvoerbaar is op 'n kommersiële skaal. Die heliostaat oppervlaktes wat nodig is om voldoende hittevloed in die son-ontvangers te bereik, om sodoende die termiese energie van verbranding te vervang, is bepaal. Daarna is die oppervlaktes met dié van kommersiële KSK-toring stasies, met soortgelyke krag vervaardiging vermoëns, vergelyk. Die skaalbaarheid van die gas turbines blyk om mededingend te wees, maar die sukses daarvan is afhanklik van aansienlike verbeterings in die doeltreffendheid van saamgeperste-lug ontvangers.

Acknowledgements

I would like to express my sincere gratitude to all those who provided assistance and support during the development and completion of my thesis:

Firstly, to my supervisors, Dr. S.J. van der Spuy and Prof. T.W. von Backström. Your understanding and input towards my research was unprecedented. Thank you for your guidance, patience and the opportunity to embark on this endeavour, it is greatly appreciated.

To STERG (Solar Thermal Energy Research Group) for providing an enjoyable environment in which I could conduct my research.

To the NRF (National Research Fund) who funded my first year of Master's.

To the CRSES (Centre of Renewable Energy Studies) who funded my second year of Master's.

To the staff at M-Tech Industrial for their assistance with Flownex.

To all other colleagues and friends, for your assistance however small it seemed.

Finally, to my parents, Hennie and Susan, and my sister Michelle, who supported my endeavour from the beginning to the end. Your unconditional love and tireless motivation is appreciated from the bottom of my heart. We did it.

Table of Contents

List of Figures

List of Tables

Nomenclature

Symbol	Description	Unit
Roman Symbols		
A	Area	[m^2]
c_f	Friction coefficient	
c_p	Specific heat at constant pressure	
D	Diameter	[m]
E	Energy	[J/kg]
E_i	Expected frequency	
f	Friction factor	
h	Enthalpy	[J/kg]
K_L	Loss coefficient	
L	Length	[m]
$\dot{m}$	Mass flow rate	[kg/s]
N	Speed	[rpm]
n	Day number	
O_i	Observed frequency	
P	Pressure	[Pa]
P	Power	[W]
$\dot{Q}$	Heat rate	[W]
q	Heat	[J/kg]
Re	Reynolds number	
r	Radius	[m]
r_b	Ratio of burner geometric sequence	
s	Entropy	[J/K]
T	Temperature	[K]
t	Time	[s]
U	Tip speed	[m/s]
u_τ	Friction velocity	
u_∞	Free stream velocity	[m/s]
V	Velocity	[m/s]
W	Work	[J]
$\dot{W}$	Work rate	[W]
y^+	Y-Plus value	
Z	Number of vanes	
Greek Symbols		
α	Altitude angle	[°]
αε	Coefficient	
γ	Ratio of specific heats	
δ	Declination angle	[°]

Greek Symbols (continued)

ε	Pressure ratio	
ε_r	Roughness	[mm]
η	Efficiency	
θ_z	Zenith angle	[°]
μ	Dynamic viscosity	[kg/ms]
ν	Kinematic viscosity	[m^2/s]
ρ	Density	[kg/m^3]
σ	Slip factor	
Φ	Latitude	
χ^2	Chi-Squared value	
Ψ	Power factor	
ω	Rotational speed	[rpm]
ω_{solar}	Hour angle	[°]

Subscripts

B	Brayton
C	Cold
c	Compressor
cc	Combined Cycle
e	Electric
H	Hot
h	High
l	low
R	Rankine
s	Isentropic
t	Turbine
th	Thermal
0	Total

Abbreviations

CAD	Computer Aided Drawings
CFD	Computational Fluid Dynamics
CSP	Concentrated Solar Power
DNI	Direct Normal Irradiance
DYESOPT	Dynamic Energy System Optimiser
ETA	Engine Test Automation
FAR	Fuel/Air Ratio
GHI	Global Horizontal Irradiance
GTR	Gas Turbine-to-Receiver
GUI	Graphical User Interface
HTF	Heat Transfer Fluid
IFB	Inline Firing Burner
IRP	Integrated Resource Plan

Abbreviations (continued)

KSK	Konsentrerende Sonkrag
LCOE	Levelized Cost Of Electricity
NREC	Northern Research Engineering Corporation
PDF	Probability Density Function
PLC	Programmable Logic Controller
PV	Photovoltaic
SCRAP	Spikey Central Receiver Air Pre-heater
SHGT	Solar Hybrid Gas Turbine
SUNSPOT	Stellenbosch University Solar Power Thermodynamic
TES	Thermal Energy Storage
TDML	Turbine Design Mean Line
TPERF	Turbine Performance

1 Introduction

South Africa's population has increased by approximately 53 % in the last 20 years (World DataBank, 2013). This population growth necessitates an increase in electricity supply, while environmental concerns require a simultaneous reduction in carbon emissions and other greenhouse gases. Furthermore, concerns about the sustainability of fossil fuel supplies have led to an interest in developing local renewable energy resources, thus decreasing the country's future dependency on imported supplies.

Sunlight is the most abundant of all renewable energy resources. There are a number of proposed and installed systems available to convert incident solar irradiation into electricity. A solar hybrid gas turbine (SHGT) cycle is such a prospective system, combining mature gas turbine technology with innovative solar power plant research. The present study evaluates the influence of solar-hybridization on the performance of an existing gas turbine engine.

This chapter presents a brief background on solar resource, solar power technologies and the need for solar hybrid power plants. The study's objectives and a motivation for undertaking the study are given thereafter.

1.1 Background

Sunlight has the biggest potential of all renewable energy resources. More solar energy falls on the earth in 5.7 hours, than the annual consumed energy of the global population (Knies *et al.*, 2007). If only a fraction of this energy could be harvested, the world's electricity demand could be met by a clean and sustainable energy source.

Two of the most common technologies installed to utilise solar energy for power generation are Concentrating Solar Power (CSP) and Photo-Voltaic (PV) systems. Solar power has a disadvantage, in that it can only be harvested during the day, while the peak consumer electricity demand is experienced in the evenings. PV plants convert solar energy directly to electricity and in order to dispatch electricity in the evenings, battery banks have to be installed. This exponentially increases the cost of the plant. Conversely, CSP systems convert concentrated light to heat which is more economical to store (Duffie and Beckman, 1991). The thermal energy can be converted to electricity using a Rankine cycle when needed, but the process, even when utilizing a dry-cooled Rankine cycle, is more water intensive than a gas turbine. This, together with the high capital costs of the overall plant, suggests that further investigation for an alternative power solution is required.

One potential solution is the development of hybrid thermo-solar power plants, more specifically those based on the Brayton gas turbine cycle. SHGT systems are of interest due to their potential low water consumption and high achievable conversion efficiency when implemented in a combined cycle. Additional anticipated advantages are full power dispatchability, system reliability and quick start-up and shut-down times.

The Stellenbosch University Solar Power Thermodynamic (SUNSPOT) cycle, proposed by Kröger (2012), implements a solar hybrid gas turbine Brayton top cycle, thermal storage and bottoming Rankine cycle. The solar hybrid gas turbine uses concentrated solar power to heat pressurised air exiting the compressor. High working fluid temperatures are achieved with a central receiver coupled to a heliostat field. The pressurised, heated air enters the combustion chamber and additional fuel is burnt until the desired turbine inlet temperature is achieved. Fuel combustion can also potentially be used to compensate for fluctuations in solar resource.

Gas turbine technology is mature and well researched, but studies about the performance of gas turbines when integrated into CSP systems are limited. The present study is one of the first of its kind at Stellenbosch University and a model that could aid future development of the SUNSPOT cycle will be established. As a first iteration, the Rover 1S/60 gas turbine engine will be integrated into a CSP system. Site data from Stellenbosch University's testing facility, the Helio100 solar field, will be used to evaluate resource availability and the feasibility of operating gas turbines on solar energy only. The research will be applicable to both current and future developments at the Helio100 solar field.

1.2 Objectives

The objective of the present study is to investigate the effect of the solar-hybridization of a gas turbine; on its performance and its integration in a solar power plant. This is expanded as follows:

- Model the existing Rover 1S/60 gas turbine using the commercial flow network code, Flownex (2014b).
- Design and model a solar hybrid Rover gas turbine based on the SUNSPOT configuration.
- Adapt and re-evaluate both the existing Rover gas turbine and solar hybrid Rover gas turbine models, including a newly designed compressor stage.
- Predict the performance of the solarized Rover gas turbine within the Helio100 solar field.
- Evaluate the main air casing with computational flow analyses to establish the interconnection component's inlet conditions.
- Perform experimental testing on the Rover 1S/60 gas turbine to validate the computational flow model.

- Propose a suitable interconnection design between the Rover 1S/60 gas turbine and a solar receiver.
- Investigate the feasibility of implementing a solar hybrid gas turbine at commercial level.

1.3 Motivation

The South African Integrated Resource Plan (IRP) includes an electricity plan that migrates towards lower carbon energy generation methods. The first iteration of the plan allocated a significant amount towards renewable energy.

However, at present electricity generation from pure thermo-solar input is more expensive than conventional generation technologies (Jamel *et al.*, 2013). With less than 3 GW of installed capacity globally, it is still considered an emerging technology (Gauché *et al.*, 2014) and it is expected that the more mature the technology becomes, the cheaper it will be. According to Kolb *et al.* (2011), the greatest potential for cost reduction in CSP lies in the central receiver system.

A further cost reduction could be realised when exploiting the high efficiency of a combined cycle, ranging between 45 % and 57 %, compared to the efficiency of a Rankine cycle which ranges from 30 % to 35 % (Rao, 2012). Another advantage of a combined cycle power plant is the small timeframe in which the plant can be constructed. Plants larger than 200 MW could be erected in less than 24 months (Rao, 2012).

The SUNSPOT cycle fuses the advantages of SHGT's and combined thermodynamic cycles, theoretically creating a suitable and cost effective cycle for electricity generation. South Africa's solar resource is among the best worldwide, with the majority of the country receiving more than 2100 kW/m^2 of annual Direct Normal Irradiation (DNI) (GeoModel Solar, 2014). This study will align itself by investigating a cost effective solution to supplying clean electricity on a large scale. The present study will provide insight into the adaptation of existing gas turbines for solar hybrid use, and its effects on the gas turbine's performance.

2 Literature Review

The present study combines concentrated solar technologies with gas turbines. This chapter presents a brief overview of solar energy, CSP and gas turbine operation theory. Thereafter the integration of gas turbines into CSP plants and the previous modelling approaches to SHGTs are investigated.

2.1 Solar Energy

Solar energy strikes the surface of the earth at a rate of 120 x 10^{15} W and one day's solar energy can satisfy the entire world's demand for more than 20 years (Chu, 2011). Most of the renewable energy sources, i.e. wind, hydro and even some fossil fuels, have their origin in sunlight and their potential is significantly less than that of solar energy, as seen in Figure 1.

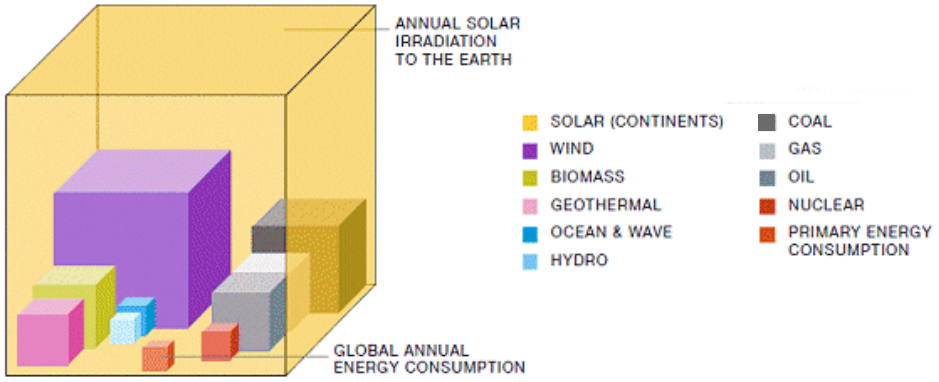

Figure 1: Comparison of potential global energy resources and annual energy consumption (EPIA and Greenpeace, 2011)

Just outside of the earth's atmosphere, solar energy is continuously available at a rate of 1367 W/m^2. However, due to the inclination of the earth's axis relative to a plane through its orbit around the sun, a large percentage of this energy does not reach the earth's surface. The solar irradiation on the earth's surface is mainly dependent on the local climate and position of the sun relative to the local site, primarily because the atmosphere absorbs and scatters some of the incoming irradiance from the sun (Stine and Geyer, 2001).

The incoming irradiation can be classified into two types. DNI is perceived as rays directly from the sun. These are typically the rays that cause shadows to form on a surface, when the sun is blocked by an object. The second type, diffuse irradiance, comes from all directions in the sky and allows us to see in the shade. The sum of these two components makes up what is known as global horizontal irradiance (GHI). The two main technologies that harness solar energy use different types of irradiation. PV plants use both DNI and diffuse irradiation while CSP plants harness DNI only.

2.2 Concentrated Solar Power

South Africa has an abundance of sunshine and, as shown in Figure 2, the annual DNI values are in excess of 2800 kWh/m^2 in the Northern Cape, making it one of the best locations for CSP in the world.

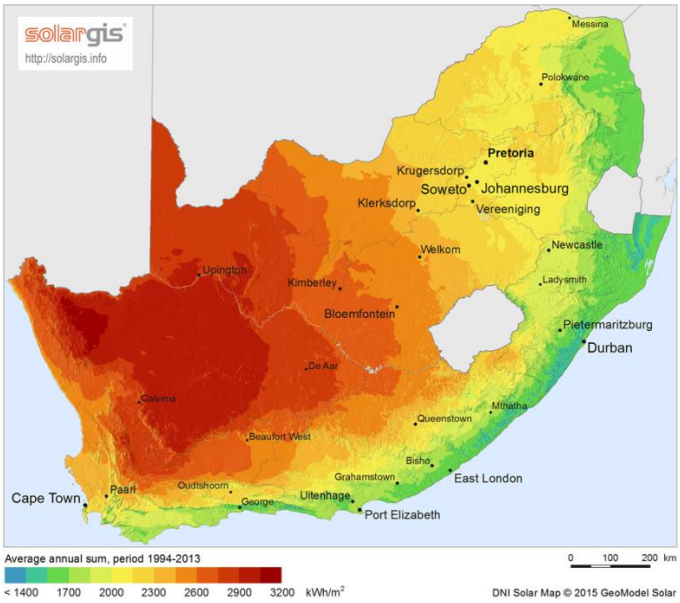

Figure 2: Annual DNI map of South Africa (GeoModel Solar, 2014)

In a recent study by Meyer and Van Niekerk (2011), a short term potential CSP capacity of 262 GW was identified in South Africa, with 51 % of the feasible sites based in the Northern Cape. The study included factors such as DNI, land use, land slope, water availability and dispatchability. CSP projects currently under development in the Northern Cape alone, total 890 MW (Meyer and Van Niekerk, 2011), suggesting positive future growth for CSP in South Africa.

2.2.1 Different CSP technologies

There are different technologies available that utilise CSP. The major CSP technologies currently in operation can be categorised under the following: Linear Fresnel, Dish Stirling, Parabolic Trough and Central Tower Receiver. These technologies are based on different concepts and are briefly discussed below, following an explanation of the importance and relevance of tracking.

2.2.1.1 Tracking Systems

The position of a specific location on earth, relative to the sun, changes throughout the day. Therefore single-axis and twin-axis tracking systems, that orientate the reflectors towards the sun, are required to maximise the solar receiver irradiation input throughout the day.

As the name states, single-axis tracking allows for one degree of freedom, whereas twin-axis tracking systems have two degrees of freedom. Trackers and tracking software have therefore become integral parts of CSP technologies.

2.2.1.2 Parabolic Trough

This is one of the oldest and most common CSP systems in use today (CSP Today, 2013). It consists of an array of parabolically shaped mirrors which track the sun's position and focuses the incoming irradiation onto a receiver, ideally located at the mirrors' focal point. The mirrors are aligned linearly, also called a linear system, and makes use of single-axis tracking. The receiver is an absorber tube, which is encapsulated by an evacuated glass tube, to minimise heat loss to the environment. A HTF circulates through the absorber tube and transfers the heat to the power generation cycle of the system.

2.2.1.3 Linear Fresnel

The Linear Fresnel system consists of an array of flat mirrors which are lined up linearly, also a linear system. The sets of mirrors track the sun's position to focus the incoming irradiation onto a fixed receiver, also known as line focus, which is situated above the mirrors. Hence, the maximum temperature to the receiver is limited. A heat transfer fluid (HTF) passes through the receiver and the heat is used to generate electricity in a steam power cycle. The HTF is usually thermal oil, molten salt or direct steam - in which case, no heat exchanger to the power generation cycle is needed. The linear system allows for single-axis tracking only.

2.2.1.4 Parabolic Dish

The parabolic dish comprises of mirrors that form a dish to reflect the incoming irradiation onto the receiver, situated at the focal point of the dish. This type of system is a point focus system. The receiver absorbs the incoming solar energy and converts it to thermal energy, which is absorbed by a circulating HTF. The thermal energy is usually converted to electric energy by means of a Stirling engine, mounted at the focal point of the dish. Twin-axis tracking is needed for the parabolic dish to work effectively.

2.2.1.5 Central Receiver Tower

The central tower receiver is a system consisting of a large field of heliostat mirrors, all reflecting the incoming irradiation onto a common target. The heliostats also use a twin-axis tracking system to keep the reflected light on the target. The common target, usually at the top of a tower, is a solar receiver which absorbs the heat and transfers it to a HTF that drives the system's power cycle. Due to the concentrated irradiation, higher temperatures are reached at the receiver, which translates into a more efficient plant (Chu, 2011).

2.2.2 Solar Thermal Power

The technologies described in the previous section all convert solar energy into thermal energy. The thermal energy is then used to generate electricity through a steam power cycle, as shown in Figure 3, with the exception of the parabolic dish that usually utilises a Stirling engine.

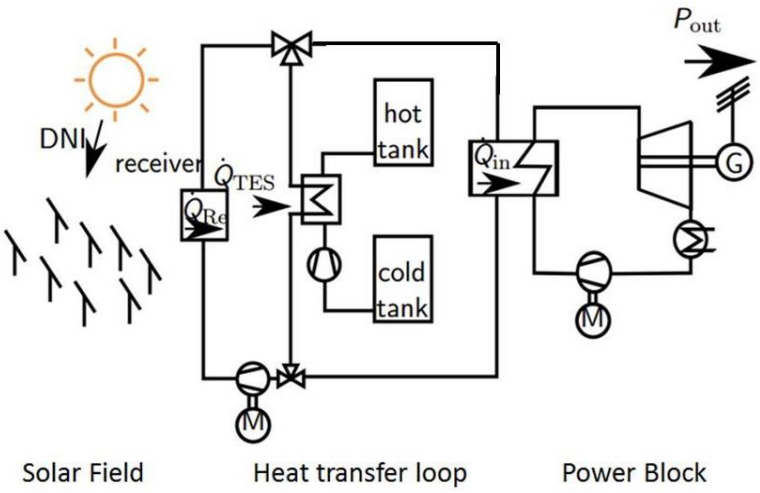

Figure 3: Solar thermal energy system (Heller, 2014)

From the receiver, the heated HTF charges a thermal energy storage (TES) system. The storage system is a critical subsystem in the heat transfer loop, as it provides the ability to store and dispatch energy when required. It also acts as a buffer against fluctuations in the transient thermal input from the solar field, enabling stable steam generation. Higher storage temperatures result in a higher thermal efficiency of the system.

Oil, rock beds and molten salt thermal storage systems have all been implemented. The thermal efficiency is limited when using silicon oil, because it degrades at temperatures higher than 400 °C (Mills, 2001). Temperatures up to 565 °C can be achieved when using nitrate salt, but with freezing points near 200 °C, not all of the thermal energy can be extracted. Allen (2010) investigated the use of rock bed storage, with air as HTF, in the SUNSPOT cycle. He concluded that rock beds should be able to store enough thermal energy, from the exhaust gas of a 100 MW_e gas turbine, to provide sufficient heat for 10 hours to a 25 – 30 MW_e steam turbine.

2.3 Gas Turbines

The use of gas turbines in solar thermal power plants presents a unique way to generate electricity while addressing current solar thermal power plant issues. This section explores the fundamental operation cycle and methods used to improve the performance of a gas turbine.

2.3.1 Gas Turbine Operation

Gas turbines can be traced back to 1791, when the first patent for a gas turbine was awarded to John Barber. The world's first gas turbine for power generation was only developed much later in 1939. Improvements in aerodynamics, metallurgical composition and manufacturing methods have resulted in the efficient gas turbines we know today. A simple gas turbine cycle is shown in Figure 4.

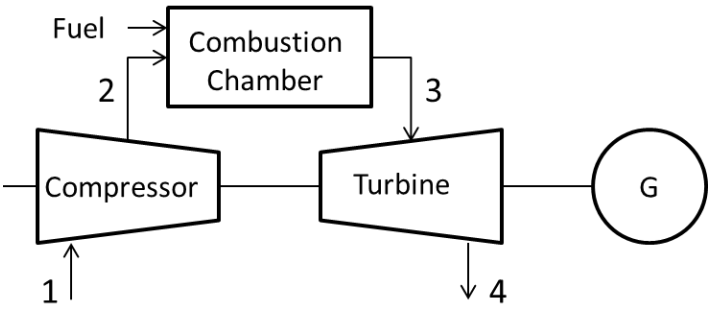

Figure 4: Simple gas turbine cycle

Gas (usually ambient air) is drawn through the intake to the compressor. The gas passes through the compressor (step 1-2), increasing in pressure. The compressed gas is then mixed with fuel and combusted in the combustion chamber (step 2-3), resulting in high temperature gases at the turbine inlet. Finally, the high temperature gases are expanded through the turbine and released back into the atmosphere (step 3-4). The compression process requires significantly less power than provided by the expansion process and thus a positive amount of net power is available to drive the generator shaft.

The ideal cycle for a simple gas turbine is also referred to as the open air standard Brayton cycle. By analysing the ideal cycle, the parameters that affect the power output and thermal efficiency can be clearly understood. The ideal Brayton cycle assumes that the compression and expansion processes are isentropic (i.e. reversible and adiabatic). No pressure losses occur in the ducting or combustion chamber and the working fluid has the same composition throughout the cycle. A constant mass flow throughout the cycle is also presumed. Figure 5 shows the Brayton cycle on a temperature-entropy chart and the numbers coincide with the zones labelled in Figure 4.

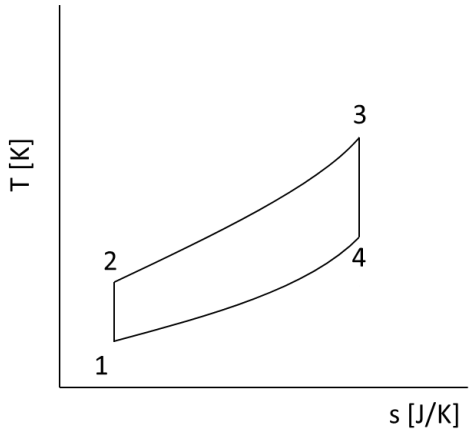

Figure 5: Brayton cycle T-s diagram

During step 1-2 the compressor requires power to compress the air. Heat is added to the air during step 2-3, through thermal energy released from the combustion process. Step 3-4 denotes the turbine work output. The waste heat is discarded to the atmosphere during step 4-1. These steps are evaluated mathematically in Section 3.3.

An important parameter is the pressure ratio of the cycle. Assuming steps 1-2 and 3-4 to be isentropic, the pressure ratio can be determined by:

$$\varepsilon = \frac{P_{02}}{P_{01}} = \frac{P_{03}}{P_{04}} = \left(\frac{T_{02}}{T_{01}}\right)^{\frac{\gamma}{\gamma-1}} = \left(\frac{T_{03}}{T_{04}}\right)^{\frac{\gamma}{\gamma-1}} \qquad 2.1$$

where P_0 denotes the total pressure and T_0 the total temperature and γ denotes the ratio of the specific heats of the gas. A value of γ = 1.4 is used for air. The thermodynamic efficiency of the cycle can then be computed by:

$$\eta_{th} = \frac{E_{useful}}{E_{in}} = \frac{\dot{W}_{3-4} - \dot{W}_{1-2}}{\dot{Q}_{2-3}} = 1 - \frac{T_{01}}{T_{02}} = 1 - \frac{1}{\varepsilon^{\frac{\gamma-1}{\gamma}}} \qquad 2.2$$

where $\dot{W}_{1-2}$ denotes the work required to drive the compressor, the work produced by the turbine is $\dot{W}_{3-4}$ and the heat input from the combustor is denoted by $\dot{Q}_{2-3}$.

Evidently the efficiency of the cycle depends on the compressor stage pressure ratio and a high pressure ratio will result in a more efficient cycle. A higher pressure ratio for an existing gas turbine would typically require redesign of the compressor impeller and diffuser, but there are various other methods that can be used to improve the gas turbine cycle efficiency or power output. These include recuperation, intercooling and reheating, discussed below.

2.3.2 Improving Brayton Cycle Efficiency or Work Output

The Brayton cycle can be altered during each of the four steps shown in Figure 5. The three improvement methods discussed below have all been well-proven in industry.

2.3.2.1 Recuperation

The first possible improvement is the addition of a heat exchanger, also referred to as a recuperator in some texts, between the compressor and combustion chamber. Instead of releasing the exhaust gases to the atmosphere, it is redirected through the recuperator. The air at the outlet of the compressor is also redirected through the recuperator, where it is heated by the exhaust gases. Since the gas is now heated before the combustor, less heat input is required by the combustor to achieve the same output. As seen in Equation 2.2, when the heat input is reduced, the efficiency of the system is increased. However, the disadvantage of including a recuperator is that the fluid friction through the heat exchanger results in additional pressure losses through the system.

2.3.2.2 Intercooling

Another way to increase the work output of the turbine is by ensuring the compressor requires less power to achieve the same pressure ratio. An intercooler, installed in the compressor, can be used for this purpose. The modified Brayton cycle for intercooling is shown in Figure 6.

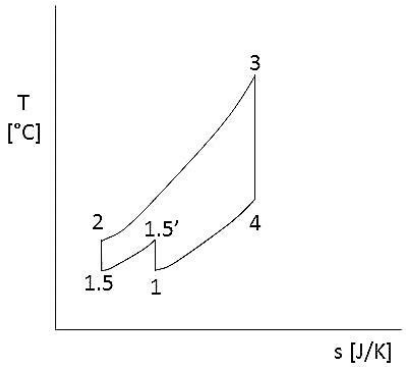

Figure 6: T-s diagram for intercooling

Air enters the compressor and is compressed to point 1.5'. The intercooler then cools the gas, usually so that $T_{1.5} = T_1$, where after it is compressed again to point 2. The rest of the cycle is completed like before. The disadvantage of intercooling is that it requires the combustor to do more work. The temperature of point 2 is reduced and therefore more heat is required to produce the same power output. Even though the work required by the compressor has been reduced, the heat required from the combustor has increased, resulting in a lower efficiency. This agrees with the findings of Chen et al. (2004), that the maximum power output and maximum efficiency cannot coexist.

2.3.2.3 Reheating

This concept is similar to that of intercooling, but it is implemented in the turbine to increase the work done by the turbine. A common application of reheating is the use of afterburners in aircraft engines. Figure 7 shows the modified Brayton cycle for reheating.

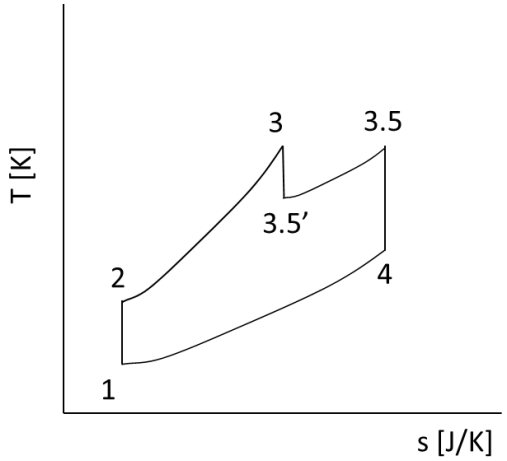

Figure 7: T-s diagram for reheating

The standard Brayton cycle is followed until point 3. There the gases are expanded to point 3.5'. The gases are reheated to point 3.5 and are expanded further until point 4 is reached. The net work output of the gas turbine is increased similar to the intercooler concept. Unfortunately, it also has the same downside as the intercooler. More heat input is required, resulting in a lower cycle efficiency.

2.4 Integration of Gas Turbines into CSP

Implementing high efficiency power cycles into CSP would lead to a reduction in the levelized cost of electricity (LCOE), i.e. the cost of the electricity produced, of a CSP plant, provided that the capital cost is reasonable. The thermal-to-electric efficiency in current operating solar tower power plants, range between 30 % and 40 %, with working temperatures of less than 600 °C (Ho and Iverson, 2014).

Several factors affect the overall plant efficiency and consequently the LCOE of the plant. Combining gas turbines within CSP systems may improve overall plant efficiency and deliver several other benefits in different sections of a solar power plant. These benefits depend on the configuration of the gas turbine within the system. The present study focuses solely on the SUNSPOT cycle, illustrated in Figure 8.

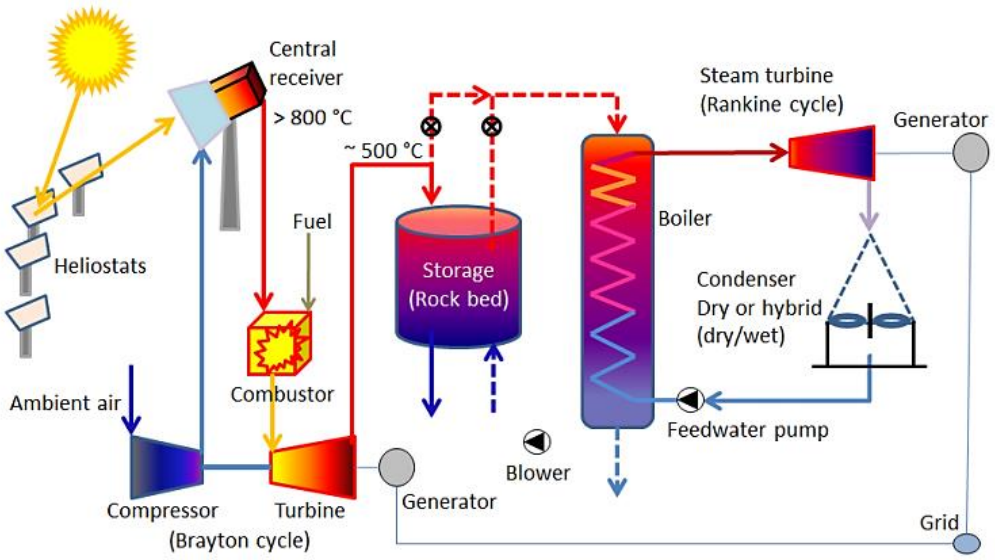

Figure 8: The SUNSPOT cycle (Kröger, 2012)

Concentrated solar irradiation is used to heat up compressed air in the receiver to more than 800 °C. The heated air is supplemented with fuel in the combustor to achieve the maximum permissible turbine inlet temperature. The gases expand through the turbine, generating electricity, completing the Brayton cycle. The exhaust gas of the turbine is at a temperature of 500 °C and the gas is used to heat the rock bed storage facility shown in Figure 8. After sunset, air is blown across the rock bed and ducted to a finned tube boiler. To supply electricity, the steam generated in the finned tube boiler flows through a steam turbine coupled to a generator. Finally, a condenser condenses the steam leaving the turbine, completing the Rankine cycle.

The SUNSPOT cycle is a combined cycle consisting of the primary Brayton cycle and a secondary Rankine cycle, with heat and work in-and-outputs, as shown in Figure 9.

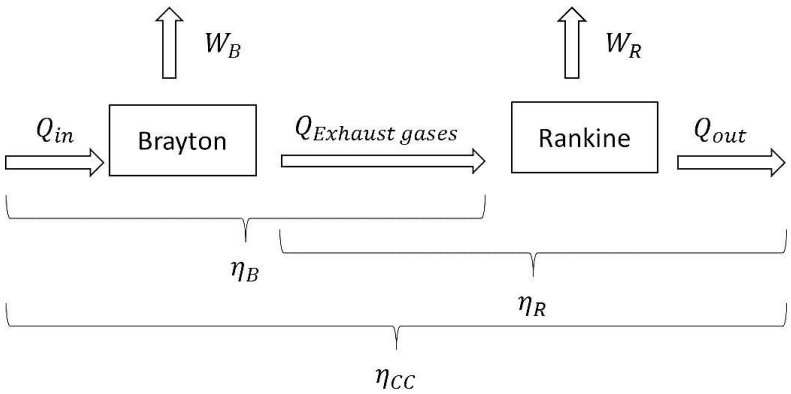

Figure 9: Combined cycle efficiency

From Figure 9, the efficiency of the combined cycle is:

$$\eta_{CC} = \frac{W_B + W_R}{Q_{in}} \tag{2.3}$$

where W_B and W_R is the work output of the Brayton and Rankine cycles respectively and Q_{in} is the total heat input into the system. Deriving Equation 2.3 in terms of the Brayton and Rankine cycle efficiencies, the following relation is found:

$$\eta_{CC} = \eta_B + (1 - \eta_B)\eta_R \tag{2.4}$$

where η_B and η_R are the Brayton and Rankine cycle efficiencies, respectively. Modern gas turbines have open cycle efficiencies between 35 % and 40 %, while subcritical steam driven power plants have efficiencies of up to 40 % (Beér, 2007). When the two are combined however, an efficiency of up to 64 % is possible according to Equation 2.4.

Using a gas turbine in this configuration also eliminates some general issues of CSP plants. A suitable gas, such as biofuel or natural gas, can be used in the combustion chamber to eliminate changes in electrical output due to fluctuations in the incoming irradiation during overcast weather conditions. Peak power demands are also met because the turbine output can be increased by burning additional fuel. The combination of the gas turbine and thermal storage gives the required flexibility and control to deliver sustainable power that matches the power demand.

The SHGT's cycle works on much the same principal as the recuperator, described in Section 2.3.2. Instead of using the exhaust gases as the heating fluid in a heat exchanger, the compressed gas is heated by the solar receiver. As with the recuperator, less heat input from the fuel is required, increasing the gas turbine efficiency.

2.5 Previous Modelling Approaches

Various models of solar hybrid gas turbines exist throughout literature, each unique in its approach. The majority of models focus on the solar part of the plant, although a few thermal performance models for hybrid configurations do exist.

Barigozzi *et al.* (2012) modelled a hybrid configuration that consisted of a heliostat field, solar central receiver and a commercial gas turbine, as shown in Figure 10. The solar field was modelled in TRNSYS®, while Thermoflex was used to simulate the gas turbine. They compared the performance of a solarized and conventional gas turbine, taking into account the electric power, shaft speed and efficiency of the gas turbine.

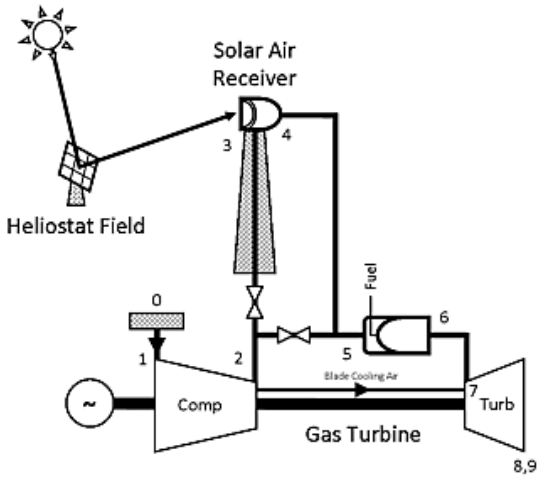

Figure 10: Layout of a simple hybrid gas turbine system (Spelling, 2013)

It was found that a reduction in electric power and efficiency was caused by the combination of air flow regulation and pressure drop associated with the solar energy input. The model also indicated substantial fossil fuel savings.

Another simulation tool for SHGTs, including an integrated TES system, was developed by Grange *et al.* (2014). The effect of the TES operating conditions on the combustion chamber performance, and thus the power plant performance, was the focus of the study. A schematic of the simulation is shown in Figure 11.

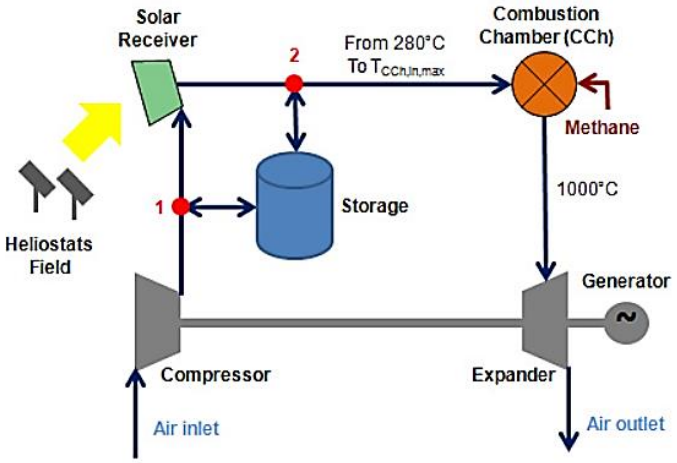

Figure 11: Schematic of the solar hybrid gas turbine with integrated storage (Grange *et al.*, 2014)

The simulation showed an increase of solar contribution, from 37.5 % to 44.7 %, due to the addition of thermal storage. The fuel consumption decreased by 6.7 % when compared to the same plant without storage.

It was noted that the configuration led to a decrease in pressure at the turbine inlet during the storage charging mode, leading to a minor decrease in electricity generation.

Schwarzbözl *et al.* (2006) assessed several prototype CSP tower plants and reported on their design and performance. The HFLCAL code, developed by Becker and Böhmer in 1989, was adapted and used to design the optics of the tower system, while TRNSYS® was also used to simulate the gas turbine. Three industrial gas turbines ranging in size (1.4 MW, 4.2 MW and 16.1 MW) were used with thermal efficiencies of 42.9 %, 40.3 % and 44.6 %, respectively. Using two different locations and hourly solar data as input, the simulations yielded solar to electric efficiency values of 14-19 %. These simulated conversion efficiencies were among the best for solar electric technologies (Schwarzbözl *et al.*, 2006).

A thermo-economic analysis on hybrid solar gas turbine power plants was done by Spelling (2013). A DYESOPT simulation tool (DYnamic Energy System OPTimiser) capable of performing plant design, equipment costing and performance evaluation was used, while TRNSYS® was again preferred to simulate transient conditions. Two turbines were simulated using a simple hybrid solar gas turbine cycle, as investigated by Barigozzi *et al.* (2012). The SGT-750 had too-high firing temperatures, while the SGT-500 was inefficient. The latter resulted because of fuels burning at a high heat rate, also causing high CO_2 emissions.

Spelling (2013) extended the model to include an optimised gas turbine, integrated storage and Rankine bottoming cycle. The integration of thermal storage increased the maximum annual solar share to over 50 %, with the SGT-750, with integrated storage, attaining a solar share of 49 % and the SGT-500 reaching nearly 100 % annual solar share (Spelling, 2013). The addition of a bottoming-cycle to the plant reduced the electricity costs by up to 15 %, when compared to the simple-cycle hybrid plant. It was concluded that in order to keep the cost of electricity low and reduce CO_2 emissions simultaneously, the hybrid solar gas turbine plant needs to integrate both thermal storage and a bottoming-cycle.

From the work published, it is evident that a reduced power output and fuel savings can be expected from a gas turbine when integrating it in to a SHGT configuration. The system layout, especially when including storage and a Rankine bottoming cycle, vary significantly, but these additions to the SHGT system seem crucial with regards to higher system efficiency and reduced LCOE. This study will simulate a SHGT within the SUNSPOT cycle configuration, as a developmental tool for SUNSPOT and also to further understand the benefits and shortcomings of hybridising a gas turbine.

3 Rover 1S/60 Gas Turbine

This chapter provides a brief overview of the history and operation of the Rover 1S/60 gas turbine. The motivation for specifically investigating the Rover gas turbine, for solar hybridization, is given and previous research work is listed. A performance analysis of the gas turbine is completed and compared to results obtained by previous studies.

3.1 History and Operation

Rover, a British car manufacturing company, was founded in 1878. Besides gas turbine automobiles, which they were famous for, Rover also manufactured gas turbines for industrial applications. They produced 1052 gas turbines between 1954 and 1973, 777 of these being the 60 hp rated unit (Hunt, 2011), a unit similar to the one currently under investigation for solar hybridization. Rover gas turbines were used in water pumping and supplementary power generation applications, with a few units also used at universities for educational purposes. The basic operation of the Rover gas turbine can be explained with the gas flow diagram, shown below in Figure 12:

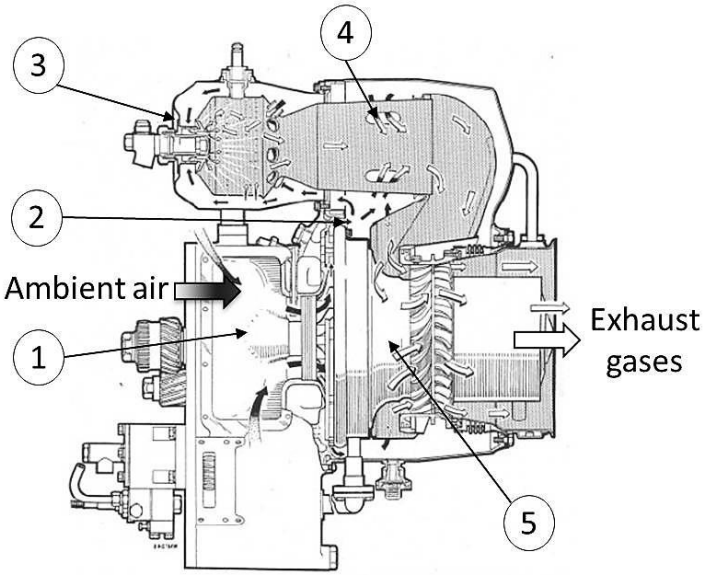

Figure 12: Rover gas flow diagram (Adapted from Rover, 1966)

Ambient air is drawn through two inlet ducts (1) to the centrifugal compressor's impeller. The air is forced outwards (compressed) and directed to the diffuser vanes where the air pressure is further increased by reducing its velocity. From the diffuser outlet, air enters the main air casing (2) where it is directed to the can-type combustion chamber. Fuel is injected via the spray atomiser at the rear end of the can-type combustor (3) and mixes with pressurised air.

During start-up, a spark plug ignites the mixture continuously until the engine operating speed is reached, at which point the combustion is self-sustaining. The expanding combustion gases are directed through the centre of the can-type combustor towards the turbine where gases continue to expand through the single stage axial turbine (5). Swirl holes along the flame tube (4) draws in cool pre-combusted air to ensure that the air temperature does not exceed the maximum turbine inlet temperature. The Rover engine's technical data, as per manual (Rover, 1966), is shown below in Table 1.

Table 1: Rover 1S/60 technical data (Rover, 1966)

Parameter	Specification
Altitude	Sea level
Barometric Pressure [kPa]	101.325
Fuel Type	Diesel/Kerosene
Main shaft speed [rpm]	46 000
Compressor	Single stage, Centrifugal
Combustor	Reverse flow, Can type
Turbine	Single stage, Axial
Turbine Inlet Temperature [°C]	750
Net Power Output [kW]	45
Fuel Consumption [kg/kWh]	0.476

While numerous gas turbines exist, the use of the Rover gas turbine as first iteration for solar hybridization was an obvious choice, due to the following practical considerations:

- The Rover 1S/60 is a robust gas turbine, with a relatively simple layout and has potential for solar hybridization and testing.
- The Mechanical Engineering Department at Stellenbosch University has access to a Rover 1S/60 gas turbine.
- The gas turbine has an external reverse flow can-type combustor, simplifying the modification process. The modification is expected to redirect the air through a solar receiver for pre-heating before combustion. This is much simpler compared to modifying a gas turbine with an internal combustion chamber for the same purpose.

Gas turbines are expensive, and with the prospect of future experimental work, the existing robust Rover gas turbine is an ideal candidate to investigate.

3.2 Previous Work

Several students have performed investigations on the Rover gas turbine currently at Stellenbosch University:

Prinsloo (2008) overhauled a similar Rover gas turbine. He measured various properties through operational testing. He also designed and installed an intake system, which measures the air mass flow rate and ensures proper air filtration prior to the compressor inlet.

Phakathi (2009) investigated the fuel delivery system and tested the fuel sprayer. Both were found to be adequate for sustainable combustion.

Quarta (2012) modelled a solar hybrid Rover gas turbine in Flownex (2014b). A simplified solar receiver and integrated thermal storage was modelled, together with a Rover 1S/60 gas turbine. He verified that the flow parameters throughout the gas turbine cycle could be modelled accurately in Flownex, validating the standard gas turbine model to testing results previously obtained by Prinsloo (2008). The solar hybrid gas turbine was modelled with an 18 kW solar input, supposedly supplied by the 25 m2 heliostat at the CSIR facility in Johannesburg. An increased thermal efficiency, coupled to a reduced fuel consumption rate, was realised at design point conditions.

Luiten (2015) evaluated the performance of the Rover gas turbine compressor and designed a new compressor stage. The new design increases the pressure ratio over the compressor, while requiring the same amount of work to drive the compressor. The new compressor was modelled with a Computational Fluid Dynamics (CFD) software package and is yet to be manufactured.

3.3 Thermodynamic Performance Analysis

Figure 13 shows a schematic layout of the solar hybrid gas turbine model. Before attempting solar hybridization, the performance of the existing Rover gas turbine was evaluated, analysing all sub-models.

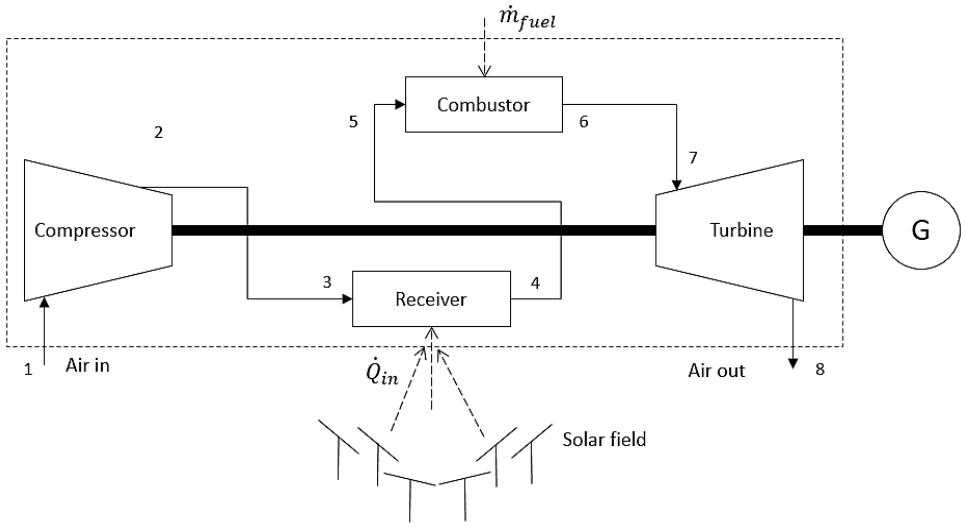

Figure 13: Schematic layout of the solar hybrid gas turbine

The numbers in Figure 13 denote the zones where different parameters from the model were evaluated, coinciding with the possible physical measurement zones on the Rover gas turbine test rig. This will simplify comparison between the model and experimental test results.

3.3.1 Compressor

For simplicity, it was assumed that zone 2 and 5, and zone 6 and 7 were identical, omitting the solar receiver. Note that all subscripts coincide with the zones in Figure 13. Assuming isentropic conditions at the compressor, the isentropic total temperature after compression is:

$$T_{02s} = T_{01}\left(\frac{P_{02}}{P_{01}}\right)^{\frac{\gamma-1}{\gamma}} \tag{3.1}$$

where P_{02} is calculated by assuming a pressure ratio of 2.8 as prescribed by the Rover engine manual (Rover, 1966). The isentropic work required to drive the compressor is then:

$$W_{c,s} = c_p(T_{02s} - T_{01}) \tag{3.2}$$

where c_p is the specific heat. To determine the real work required to drive the compressor, W_c, the slip factor, σ, and blade tip speed, U, is evaluated first by Equation 3-3 and 3-4 respectively (Cohen et al., 2001):

$$\sigma = 1 - \frac{0.63\pi}{Z} \tag{3.3}$$

$$U = \omega\pi r \tag{3.4}$$

where Z denotes the number of vanes, ω the rotational speed and r the radius of the impeller. The real work required to drive the compressor is calculated by:

$$W_c = \sigma\psi U^2 \tag{3.5}$$

Cohen *et al.* (2001) suggests a power factor (ψ) input of 1.04 for compressors. To determine the real outlet temperature of the compressor, the initial temperature is combined with the theoretical work to give:

$$T_{02} = T_{01} + \frac{W_c}{c_p} \tag{3.6}$$

The isentropic efficiency of the compressor is then simply:

$$\eta_{compressor} = \frac{T_{02s} - T_{01}}{T_{02} - T_{01}} \quad 3.7$$

The real work required to drive the compressor, W_c, can also be found by dividing the calculated isentropic work by the isentropic efficiency. The combustor inlet temperature is adjusted, thus altering the compressor efficiency, until the real work required is equivalent to that calculated in Equation 3.5. Finally, the power required by the compressor is then:

$$\dot{W}_c = \dot{m} W_c \quad 3.8$$

where $\dot{m}$ denotes the mass flow rate of the air.

3.3.2 Combustor

The energy input into the combustor is limited by the maximum temperature that the turbine blade can withstand, which is 1032 K according to the Rover engine manual (Rover, 1966). The energy input to the combustion chamber is determined by:

$$q_{combustor} = c_p(T_{07} - T_{02}) \quad 3.9$$

Thereafter, the isentropic temperature is calculated as:

$$T_{07s} = \frac{q_{combustor}}{c_p} + T_{02s} \quad 3.10$$

The combustor efficiency is then simply:

$$\eta_{combustor} = \frac{\Delta h_{actual}}{\Delta h_{theoretical}} = \frac{T_{07} - T_{02}}{T_{07s} - T_{02}} \quad 3.11$$

The pressure drop over a combustor, according to Cohen *et al.* (2001), is between 2 % and 8 %, therefore a mean value of 5 % was assumed. A sensitivity analysis between the extremes determined less than a 2 % difference in the net power output and combustor thermal efficiency of the gas turbine.

3.3.3 Turbine

The turbine efficiency was determined by using a method stipulated in *Cohen et al.* (2001). The method uses the turbine geometry, along with a set of empirical equations to determine the turbine axial and relative velocities, the rotor and stator inlet and exit gas angles, as well as their respective losses.A systematic explanation of the method is provided in Appendix G of Quarta (2012) or Appendix C of Luiten (2015).

To determine the work output of the turbine, the isentropic temperature at turbine outlet is determined first, assuming the outlet pressure (P_{08}) to be ambient.

$$T_{08s} = T_{07}\left(\frac{P_{08}}{P_{07}}\right)^{\frac{\gamma-1}{\gamma}} \tag{3.12}$$

As with the compressor, the isentropic work output is determined:

$$W_{ts} = c_p(T_{07} - T_{08s}) \tag{3.13}$$

where after the power output from the turbine is calculated by:

$$\dot{W}_t = \dot{m}W_{ts}\eta_{turbine} \tag{3.14}$$

The real temperature at turbine exit can be calculated by:

$$T_{08} = T_{07} - \eta_{turbine}T_{07}\left(1 - \left(\frac{1}{\left(\frac{P_{07}}{P_{08}}\right)^{\frac{\gamma-1}{\gamma}}}\right)\right) \tag{3.15}$$

3.3.4 Complete Brayton Cycle

Finally, the net power produced by the gas turbine is calculated by subtracting the work required by the compressor from the work produced by the turbine:

$$\dot{W}_{net} = \dot{W}_t - \dot{W}_c \tag{3.16}$$

The thermal combustion efficiency of the turbine is determined by evaluating the ratio of the energy output to energy input:

$$\eta_{th} = \frac{\dot{W}_{net}}{q_{combustor}\dot{m}} \tag{3.17}$$

3.3.5 Performance Prediction Results

Ambient air conditions of 30 °C and 101.325 kPa were used as input values to simulate the gas turbine at its design point. A comparison of the performance prediction's results to similar analyses by Quarta (2012) and Luiten (2015) is given in Table 2. The results indicate that the thermodynamic analysis of the existing Rover 1S/60 gas turbine compares well to the previous performance analyses.

Table 2: Results and comparison of thermodynamic performance analysis

		Current Study	Luiten (2015)	Quarta (2012)
$\dot{W}_{net}$	[kW]	43.32	44.18	44.70
η_{th}		0.104	0.105	0.107
T_{01}	[K]	303.15	303.15	288.15
T_{02}	[K]	446.84	445.37	429.16
T_{07}	[K]	1032.00	1032.00	1030.00
T_{08}	[K]	836.64	846.60	845.58
P_{01}	[kPa]	101.33	101.33	101.33
P_{02}	[kPa]	283.71	275.91	283.71
P_{07}	[kPa]	269.52	262.11	266.40
P_{08}	[kPa]	101.33	101.33	103.55

As seen in Table 2, the temperature predictions of Quarta (2012) are different when compared to both the current study's results and that of Luiten (2015). This is as a result of differences at the inlet temperature boundary condition and the chosen maximum turbine inlet temperature. The resulting pressure predictions, however, compare well to that of Quarta (2012).

There is less than a 4 % difference between the predicted power out and the thermal efficiency, when compared to the results of the previous performance predictions respectively. The thermodynamic analysis was therefore deemed acceptable to verify the gas turbine model created in Flownex (2014b), discussed hereafter.

4 System Simulation Methodology

In order to predict the performance of the solar hybrid gas turbine, an accurate model of the plant is required. A model of the solar field situated at Stellenbosch University's test facility, Helio100, predicts the maximum available solar resource, after which the gas turbine and solar receiver is modelled independently to investigate the effects of solar hybridization. The storage and Rankine steam cycle was omitted from the simulation scenario.

The gas turbine model development is described in the present chapter. Thereafter the solar resource and solar components are examined, before implementing the component models into the gas turbine model to evaluate their effects on the performance of the gas turbine.

4.1 Simulation Software and Model Development

Flownex (2014b) was used to simulate the gas turbine and solar receiver integration. The software allows the user to solve for various properties through thermal-fluid network analyses. Some of these properties include the flow rates, pressures, temperatures and heat transfer rates. Capable of both steady-state and transient analyses, the software is versatile and useful to evaluate the effects of changes to a system in real time.

Flownex has a drag-and-drop graphical user interface (GUI) in which the desired flow networks are created. The basic building blocks of a network are nodes, elements and boundary conditions, and are joined to form a network as shown in Figure 14.

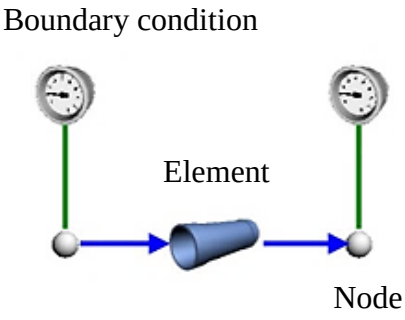

Figure 14: Basic network (Flownex, 2014a)

An element can be adjusted to the user's requirement by specifying properties such as the fluid through the element, the element geometry and primary and secondary losses. Different elements, from pipe bends to compressor and turbine elements, enable an accurate specification of the network required for analysis. Nodes generally connect different elements and the system's boundary conditions are specified by using the boundary condition component.

After a network is created, the conservation equations are solved in order to see the resultant properties (such as temperatures and pressures) over each element. The convergence criteria for the conservation equations can be customised for the steady-state and transient solutions, but a typical convergence criterion of $1x10^{-6}$ is used within the Flownex simulation environment and was deemed acceptable.

4.2 Gas Turbine Model Methodology

The Rover gas turbine model created by Quarta (2012) was adopted for the present study, as it was successfully simulated in his thesis. The details of the intake system, compressor- and turbine- performance maps were obtained, evaluated and found suitable for the intended use. The different components of the Rover gas turbine model are discussed below.

4.2.1 Intake System

The intake system considered by Quarta in his Flownex model, is identical to the one installed at Stellenbosch University and was originally designed and built by Prinsloo (2008). The air is drawn in through a conical inlet, split into two ducts and filtered before flowing to the compressor inlet. The differential pressure is measured at the conical inlet in order to determine the mass flow rate into the system. The intake system is shown in Figure 15 below:

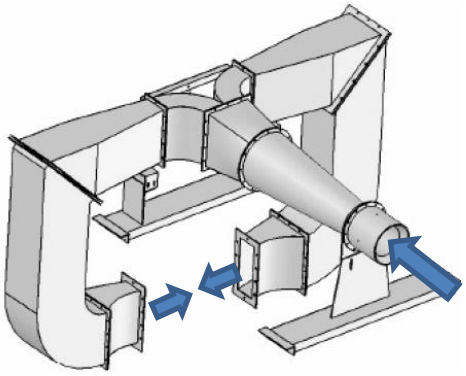

Figure 15: Air intake system (Adapted from Prinsloo, 2008)

The duct dimensions were specified where after air flow through the ducts was simulated. The aim of the simulation was to achieve the correct pressure drop, as determined through experimental testing by Prinsloo, at a particular mass flow rate through the intake system. To obtain the correct loss coefficient for the air filters, the system was first simulated without any air filters, where after the results were compared to the experimental results. The resulting pressure difference was used along with the air density, ρ, and the air velocity, V, to determine the air filter loss coefficient shown in Equation 4.1.

$$K_L = \frac{2\,\Delta P}{\rho\, V_{avg}^2} \tag{4.1}$$

Since the air density and velocity were known, the loss coefficient could be calculated. A loss coefficient of 19.83 was calculated and incorporated into the original, no filter, Flownex intake model. The results of the simulation were again compared to the experimental results obtained by Prinsloo (2008), as shown in Appendix A. At the designed air mass flow rate of the Rover gas, the difference was found to be less than 1 %. Because gas turbine performance is affected by atmospheric conditions and these tests were performed in Pretoria, South Africa, a design mass flow rate of 0.5 kg/s was established. It was thus concluded that the intake system, modelled by Quarta, is acceptable for this study.

4.2.2 Gas Turbine Performance Maps

A gas turbine's performance at various input conditions can be evaluated by utilising characteristic maps for the compressor and turbine respectively. These maps relate the gas turbine's pressure ratio, efficiency and corrected mass flow rate at various corrected speed lines in order to provide an accurate gas turbine performance output.

Neither the turbine map, nor the compressor map of the original Rover 1S/60 were available and thus both these were created by Quarta (2012). A brief description of the processes to create the performance maps is given. A new compressor stage, designed by Luiten (2015), was implemented to evaluate its effects on the system's performance. The process involved to generate the newly designed compressor map is also discussed.

4.2.2.1 Turbine Map

The same Rover gas turbine investigated by Quarta is under investigation at Stellenbosch University. By comparing the turbine geometry, it was confirmed that the turbine map was created for the same turbine. The process followed to obtain the turbine map is outlined in Figure 16 and explained thereafter.

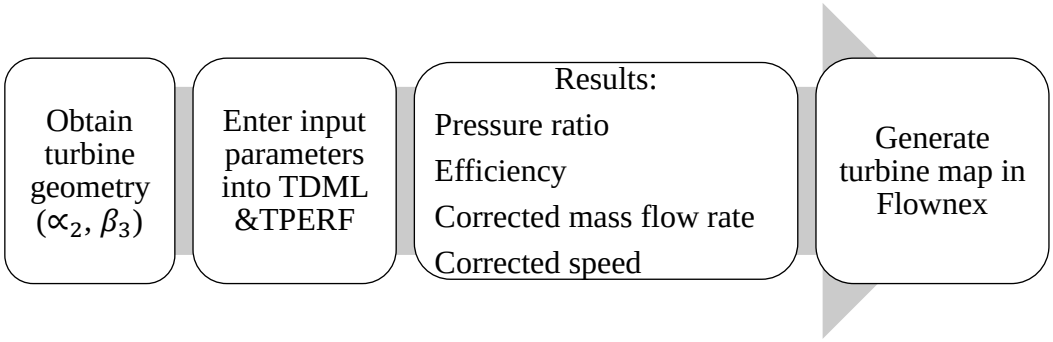

Figure 16: Process to generate the turbine map

The stator and rotor outlet gas angles were determined when calculating the turbine's efficiency (discussed in Section 3.3.3).The angles are input requirements for a one-dimensional solver, which generates the turbine performance lines. The Northern Research Engineering Corporation (NREC) developed the solver, which consists of two separate programs, namely Turbine Design Mean Line (TDML) and the Turbine Performance (TPERF) programs.

The TDML program was used iteratively until the stator and rotor angles were similar to the calculated values. The program yields the rotor inlet angle, an input required to run the TPERF code, which generates speed lines at various engine speeds. The results were extracted to Flownex map creator, from where the relevant map for the turbine was created.

4.2.2.2 Compressor Map

To generate the compressor map, Quarta obtained a set of spreadsheets from M-Tech Industrial, containing data based on an ALSTOM compressor. Using the design point efficiency, pressure ratio, corrected mass flow and corrected speed of the Rover 1S/60 gas turbine as input values, a scaled map, which is based on the original maps of the ALSTOM compressor, were created. It was found that, although the method was not ideal, the resulting compressor map represented the Rover gas turbine's compressor with reasonable accuracy in the simulations.

4.2.2.3 New Compressor Map

A new compressor was designed by Luiten (2015) as a part of his master's thesis. The newly designed compressor was not manufactured, but simulations were performed at the Rover gas turbine's design speed of 46 krpm, in order to obtain a performance line for the associated mass flow, pressure ratio and efficiency. The new compressor design point data is compared to the original compressor's design point data in Table 3.

Table 3: Compressor performance comparison at 46 krpm

	Original compressor	New compressor
Mass flow [kg/s]	0.603	0.6
Pressure ratio	2.8	3.44
Efficiency [%]	70.6	85.55

The new design improves the pressure ratio and therefore the efficiency of the compressor, as seen when Equation 3.1 is substituted into Equation 3.7. Implementing the new design could improve the performance of both the standard and solar hybrid Rover gas turbine. Flownex requires at least three performance lines in order to interpolate and iterate until the solution has converged, thus the single performance line was insufficient.

Multiple performance lines, hereafter referred to as the performance map, were generated using CompAero. This software package is used to design, refine and evaluate the performance of compressors and turbines. Various programs exist within CompAero, each unique in their capability to assist in the aerodynamic design and analysis processes of compressors and turbines. From these programs, only SIZE, VDDESIGN and CENCOM were used to generate the new compressor performance map.

To accurately predict the performance of the new compressor, the geometry of the impeller, vaneless passage and diffuser were sourced from the thesis and Computer Aided Drawing (CAD) files of Luiten (2015) as input parameters into SIZE. The design point data, seen in Table 3, were also required as input parameters. SIZE computes the initial compressor geometry, whereafter it is used as input data for CENCOM, the performance analysis program. After an initial performance analysis, the diffusor geometry data was exported to VDDESIGN, which allows refinement of the diffuser geometry. From VDDESIGN, the refined diffuser was exported back into CENCOM, where the performance of the compressor was re-evaluated. The results of the impeller performance at design point are compared to results obtained by Luiten (2015) in Table 4.

Table 4: Design point parameters comparison - Impeller

	Required value (Luiten, 2015)	**Achieved value (CENCOM)**
Mass flow rate [kg/s]	0.6	0.6
Tip total temperature [°C]	443.94	445.36
Tip total pressure [kPa]	369.34	368.56
Tip flow coefficient	0.28	0.282
Work input factor	0.98	0.943

The performance of the compressor correlates well to the values reported by Luiten (2015). A maximum difference of approximately 4 % was found between parameters of the required and achieved impeller performance. A similar comparison between the required and achieved values of the vaned diffuser can be found in Appendix B, which reveals a maximum parameter difference of 7 %. For the purpose of this investigation, the compressor is adequately represented by the values calculated in CENCOM and VDDESIGN.

To generate the required performance map, the compressor performance was re-evaluated, while varying the speed from 41 krpm to 47 krpm. To import the maps in to Flownex, the corrected speed and corrected mass flow rates are required. These corrected values are often termed non-dimensional rotational speed and mass flow respectively, and can be determined by (Cohen et al., 2001) :

$$N_{corrected} = N/\sqrt{T_{01}} \tag{4.2}$$

$$\dot{m}_{corrected} = \dot{m}\sqrt{T_{01}}/P_{01} \quad 4.3$$

Note that pressure should be specified in bar. The corrected mass flow rate, pressure and efficiency at various corrected speeds were exported to Flownex, where the performance map was created. The performance map illustrating the pressure ratio against the corrected mass flow rate, at various corrected speeds, is shown in Figure 17.

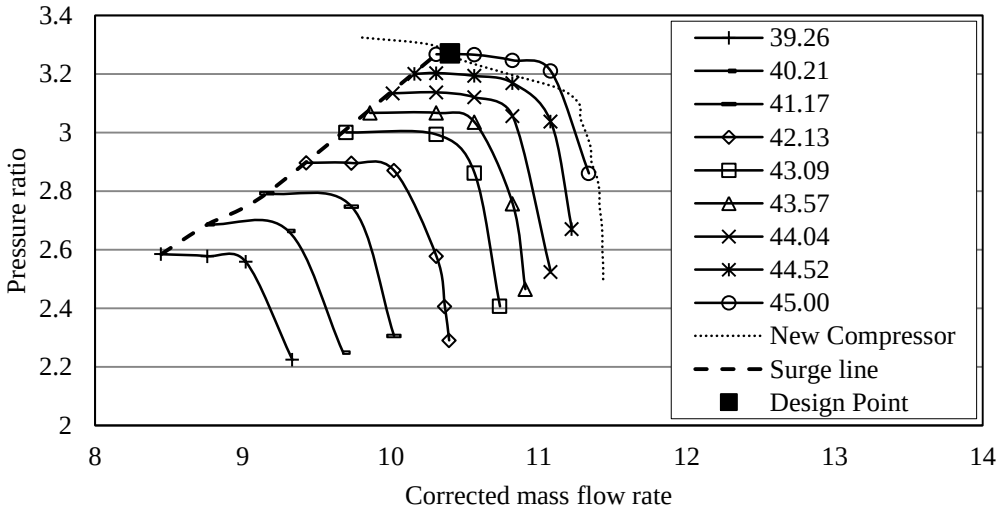

Figure 17: Performance map of the newly designed impeller

Each performance curve represents the change in compressor performance over various mass flow rates, at a specific compressor speed. A line connecting the peaks of the characteristic curves, referred to as a surge line, indicates the region of stable operation (Grong, 2009). The compressor operating point is within the stable region as long as it is located on the right-hand side of the surge line.

The performance line generated by Luiten (2015), at 46 krpm or a corrected speed of 44.04, is represented by the dashed line in Figure 17. The pressure ratio and efficiency of the new compressor is under predicted by 4.94 % and 3.28 % respectively at design point, due to CompAero performing a 1-D analysis as opposed to the preferred 3-D analysis. The performance map depicting the efficiency against the corrected mass flow rate can be found in Appendix B. The conservative results were deemed acceptable for further simulation purposes.

4.2.3 Combustion Chamber

The Rover gas turbine makes use of a tubular can-type combustion chamber. In order to model it in Flownex, two elements are required, namely the adiabatic flame element and a pipe element. The adiabatic flame element uses a secondary program, namely the NASA Glenn Chemical Equilibrium Program CEA2 (the Gordon-McBride program), to calculate off-gas compositions and the maximum temperature of a chemical reaction (Flownex, 2014a).

However, the adiabatic flame element does not account for the pressure drop in the combustor. Instead, Flownex (2014a) suggests modelling the flame element in parallel with a pipe element as seen in Figure 18, in order to specify the geometry, which will result in the required pressure drop.

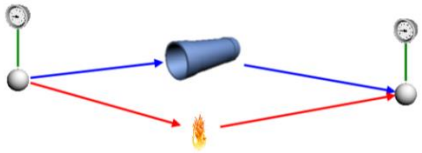

Figure 18: Adiabatic flame element

For consistency the pressure drop over the combustor was estimated at 5.00 %, as done in the thermodynamic performance analysis described in Section 3.3. A pressure drop of 14.19 kPa was found during the thermodynamic performance analysis and used as an estimate to determine the loss coefficient of the pipe element. Using Equation 4.1, with the density and velocity known, the loss coefficient of the combustion chamber was calculated as 7.78 and specified accordingly in the combustor pipe element properties.

4.3 Flownex Gas Turbine Model

The aforementioned elements were combined with nodes to create a network diagram. The intake system was omitted from this network diagram to make the model comparable to the thermodynamic analysis, as the latter does not account for losses in the intake system. Inlet and outlet boundary conditions were added to the compressor intake and turbine outlet respectively. A network diagram of the standard Rover gas turbine model is shown in Figure 19.

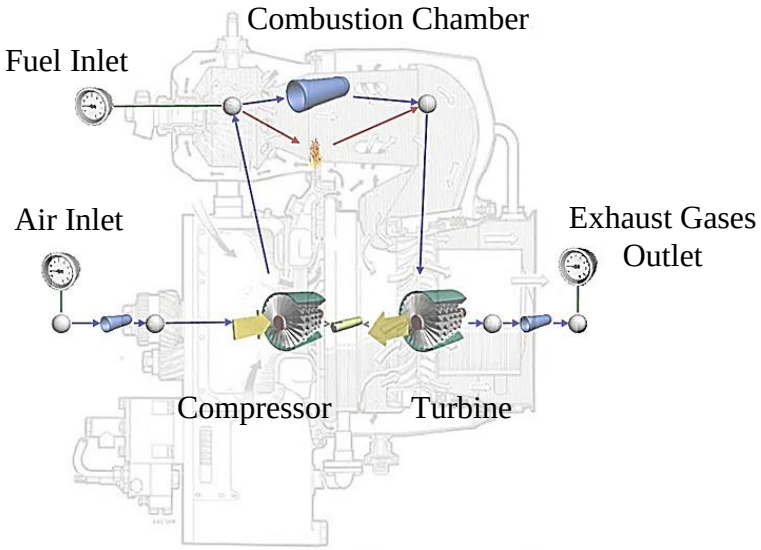

Figure 19: Standard Rover gas turbine network diagram

Figure 19 superimposes the network diagram onto Figure 12, in order to visualise what the various elements represent. The compressor and turbine is connected via a single shaft. The boundary conditions are denoted by a gauge-icon, as shown in Figure 19. The fuel delivery system was modelled by specifying the fuel type and mass flow rate as a boundary condition.

4.4 Solar Hybrid Gas Turbine Model Methodology

The effects of solar hybridization, on the performance of the Rover gas turbine, were investigated by expanding the standard model discussed in Section 4.3. As a first iteration, a solar receiver and relevant piping up and down the solar tower was implemented into the model, after investigating the resource availability at Stellenbosch University's Helio40 and Helio100 solar field testing facilities.

4.4.1 Solar Resource Availability

To predict the maximum thermal energy available from solar irradiation, at Stellenbosch University's solar field testing facilities, annual meteorological data for the period 2013/2014 was obtained. Specifications of both solar field testing facilities were used to estimate the potential thermal energy that could be supplied to a solar receiver. The methodology and results are discussed hereafter.

4.4.1.1 Solar Data

Annual solar data was obtained from the Sonbesie weather station at Stellenbosch University, as it is located closest to the solar field testing facilities. The station measures DNI directly with a SOLSYS sun tracker from Kipp & Zonen. The hourly averaged data was used, as opposed to 1000 W/m^2, commonly used in solar prediction calculations (Lovegrove and Stein, 2012). The tracker was last calibrated on 18 July 2012, which was deemed satisfactory since it is required that recalibration is done every two to three years (Kipp & Zonen, 2008).

4.4.1.2 Heliostat Field Specifications

Two different heliostat field sizes were considered, namely Helio40 and Helio100. These were chosen because experimental testing at the solar fields could be a possibility in the near future. The field specifications are given in Table 5.

Table 5: Solar field specifications

	Helio40	**Helio100**
Heliostat aperture area [m^2]	2.2	2.2
Number of heliostats	18	120
Field aperture area [m^2]	39.6	267.6
Location	Stellenbosch University	Mariendahl
Tower height [m]	18	14

With an optimal measured DNI value of 1050 W/m^2, disregarding all other possible losses, a maximum value of 41.58 kW_{th} is available at Helio40. Using the design point mass flow rate along with Equation 3.9, the gas turbine engine requires approximately 417 kW_{th} to run at its intended design point, based on heat released from the reaction of combustion. This means that less than 10 % of the heat input required by the Rover gas turbine could be supplied, given the best, albeit unrealistic, circumstances at Helio40. Under the same conditions Helio100 could supply more than 50 % of the heat input required, because of its much larger aperture area. Therefore, in order to see the effect that solar irradiation will have on the solar hybrid gas turbine, Helio100 was chosen for all further simulations.

To determine a more realistic value for solar irradiation concentrated on the solar receiver, the optical efficiency of the heliostat field was approximated by a sixth order polynomial, which accounts for the shading, blocking and cosine effects (Gauché *et al.*, 2011):

$$\eta_{optical} = 0.4254\theta_z^6 - 1.148\theta_z^5 + 0.3507\theta_z^4 + 0.755\theta_z^3 - 0.5918\theta_z^2 + 0.0816\theta_z + 0.832 \quad 4.4$$

where $\theta_z$is the zenith angle. This is the angle between the vertical and the line to the sun and can be determined through the evaluation of the following solar angles: The declination angle, the hour angle and the solar altitude angle. These angles are explained further in Appendix C, where after a sample calculation is given. Other factors influencing the amount of irradiation reaching the solar receiver is the heliostat reflectivity availability, fouling and tracking accuracy. The combined efficiency of these factors was taken to be 81 % (Stine and Geyer, 2001) and the amount of solar irradiation on the solar receiver is determined as:

$$\dot{Q}_{solar} = DNI\ A_{perture}\eta_{optical}\ \eta_{reflect,availability,soiling,accuracy} \quad 4.5$$

In order to determine the maximum amount of solar irradiation converted to thermal energy within the solar receiver, as well as the pressure drop through the receiver, a concise review on published experimental data of solar receivers is discussed in the next section.

4.4.2 Central Receiver Review

Heat input from incoming solar irradiation serves as a preheating stage before combustion, similar to a recuperated gas turbine. Preheating the compressed air before combustion will lower fuel consumption and it is envisaged that all the fuel could be replaced with heat from concentrated solar irradiation. A solar receiver converts solar irradiation into heat, whereafter the heat is transferred to a working fluid circulating through the receiver.

Solar receivers reach high temperatures during the day, which leads to high system thermal efficiencies, according to Carnot's theorem which states:

$$\eta_{max} = 1 - T_C/T_H \quad 4.6$$

where T_H and T_C is the temperature of the hot and cold reservoirs respectively. The efficiency of a system cannot be larger than that given by Carnot's theorem. To achieve a higher system thermal efficiency, the temperature of the working fluid can be increased, increasing the input temperature (T_H).

With an increase in temperature, several challenges arise in the development of solar receivers. These include the geometric design of the receiver to maximize solar irradiance absorption and heat transfer to the working fluid, while minimizing heat and pressure losses. The design of a solar receiver is not the objective of this thesis, but it plays a crucial part in the outcomes of the simulated results.

To model the receiver within the system, literature available on current receivers was explored. The review was limited to pressurised gas central receivers because of the configuration of the SUNSPOT cycle, which positions the solar receiver at the top of a tower, directly after the compressor stage of a gas turbine. Gas receivers can be classified under the following: Volumetric air receivers, small particle air receivers and tubular gas receivers. Published experimental data available of various gas receivers, using air as a working fluid, is tabulated below:

Table 6: Experimental data of different solar receivers

(Adapted from Le Roux *et al.*, 2014)

Receiver type	Model	η_{rec}	T_{out} [K]	T_{in} [K]	P [kPa]	$\dot{m}$ [kg/s]	ΔP [kPa]
Pressurised Volumetric	PLVCR 5	71 %	1323	-	420	-	-
	PLVCR 500	57 %	1233	300	415	-	-
	DIAPR	79 %	1477	308	1800	0.022	25
	REFOS	67 %	1073	573	1500	-	1.8
Tubular	SOLUGAS	-	873	598	850	5.6	-

The pressurised volumetric receiver efficiencies fall within a 21 % range while the output temperatures are more than 1000 K, with the highest temperature output values linked to the highest efficiency. Notably the solar receivers summarised in Table 6 operate at much higher pressures, in contrast to the low pressure ratio of the Rover gas turbine engine.

Le Roux *et al.* (2014) modelled a stainless steel open-cavity tubular solar receiver, specifically designed for a small-scale solar thermal Brayton cycle. The model used a micro turbine with a small compression ratio. It was found that high receiver surface temperatures and low mass flow rates reduced the receiver's efficiency due to high radiation heat losses. He also determined that the pressure drop through the receiver becomes significant when using small tube diameters. Thus larger tube diameters are preferred in solar thermal Brayton cycle applications. The experiments from Le Roux *et al.* (2014) were performed at a maximum mass flow rate of 0.08 kg/s, well below the expected 0.6 kg/s of the Rover gas turbine.

Lubkoll *et al.* (2014) reviewed the progress on existing pressurised air receiver concepts and highlighted important problems that developers encountered. One of the major issues is that there is limited information available on the proposed receivers, even though research of some receivers date back to the 1990's. The investigated receiver technologies and a qualitative comparison thereof are given in Table 18, Appendix D.

The review concluded that there exists a need for a central receiver that has a low pressure drop in the receiver, is robust, cost efficient and has effective thermal energy transfer capabilities. To meet these requirements, two receivers that are currently under development at Stellenbosch University are the SCRAP (Spikey Central Receiver Air Pre-heater) and Duel Pressure air receiver. The receivers are yet to be tested and due to their complex geometries, a simplified receiver was modelled for this research.

The solar receiver was modelled as a simple pipe element, specifying the heat transferred to the working fluid as an input condition in the pipe element properties. Therefore, the pipe geometry is only specified to obtain the required pressure drop. Typical solar receiver losses, such as convection and radiation losses to the environment are not applicable.

A pressure drop of 12 kPa over the SOLGATE receiver was found during testing (SOLGATE Report, 2005) and was used as an estimate within the simulation. A value of 12 kPa appeared reasonable since a pressure drop of 25 kPa and 1.8 kPa was observed during the testing of DIAPR and REFOS receivers, respectively (Le Roux *et al.*, 2014). The receiver is typically a collection of coiled pipes as shown in Figure 20.

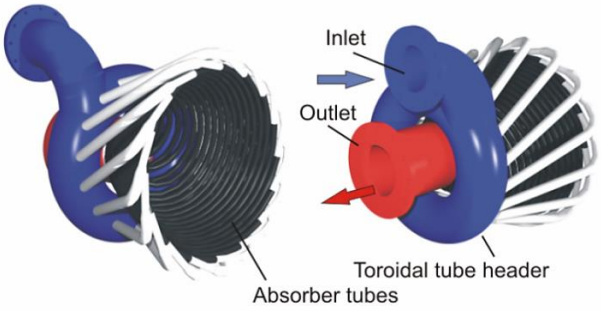

Figure 20: SOLGATE receiver (SOLGATE Report, 2005)

Assuming turbulent flow in the solar receiver pipe element, the total pressure drop in the receiver can be determined similar to the pressure loss over the combustor by evaluating:

$$\Delta P = (f\frac{L}{D} + \Sigma K_L)\frac{\rho\, V_{avg}^2}{2} \tag{4.7}$$

The receiver diameter and length was chosen as 70 mm and 1 m, respectively. To determine the friction factor, the velocity and properties from the standard gas turbine system simulation were used as first iteration, whereafter the solar hybrid gas turbine model was iteratively adjusted until the required pressure drop was achieved. The friction factor was determined from the Colebrook equation (Cengel and Cimbala, 2010), given as:

$$\frac{1}{\sqrt{f}} = -2.0\log\left(\frac{\frac{\varepsilon_r}{D}}{3.7} + \frac{2.51}{Re\sqrt{f}}\right) \tag{4.8}$$

where ε_r is the roughness of the pipe, chosen as stainless steel with a roughness value of 3µm (Flownex, 2014b). The Reynolds number is expressed as:

$$Re = \frac{\rho V_{avg} D}{\mu} \tag{4.9}$$

where μ is the viscosity of the fluid. The calculated Reynolds number is 4.3E+05 and it is assumed that turbulence exists in flow regions where Re > 4000 (Cengel and Cimbala, 2010). The Reynolds number therefore confirms turbulent flow within the solar receiver. The only unknown variable in Equation 4.7 is the loss coefficient, K_L, calculated as approximately 1.98. The pipe geometry and loss coefficient were specified in the solar receiver pipe element properties, in order to obtain the required pressure drop.

To model the efficiency of the SOLGATE receiver, an approach similar to Heller and Gauché (2014) was followed. They modelled the efficiency of the REFOS receiver by fitting a linear curve to the test data, in order to determine the thermal efficiency as:

$$\eta_{th,Receiver,REFOS} = 1.19 - 4 * 10^{-4}\, T_{Receiver,out} \qquad 4.10$$

where $T_{Receiver,out}$ denotes the working fluid temperature at the outlet of the solar receiver. A linear curve was fitted to the testing data of the SOLGATE receiver cluster (SOLGATE Report, 2005). The thermal efficiency of the cluster was given for outlet temperatures of up to 1233 K, which is well above the Rover gas turbine's maximum turbine inlet temperature of 1032 K. The linear correlation of the efficiency was determined as:

$$\eta_{th,Receiver,SOLGATE} = 1.1279 - 0.00034\, T_{Receiver,out} \qquad 4.11$$

The solar receiver efficiencies for different working fluid temperatures, at the solar receiver outlet, are shown in Figure 21.

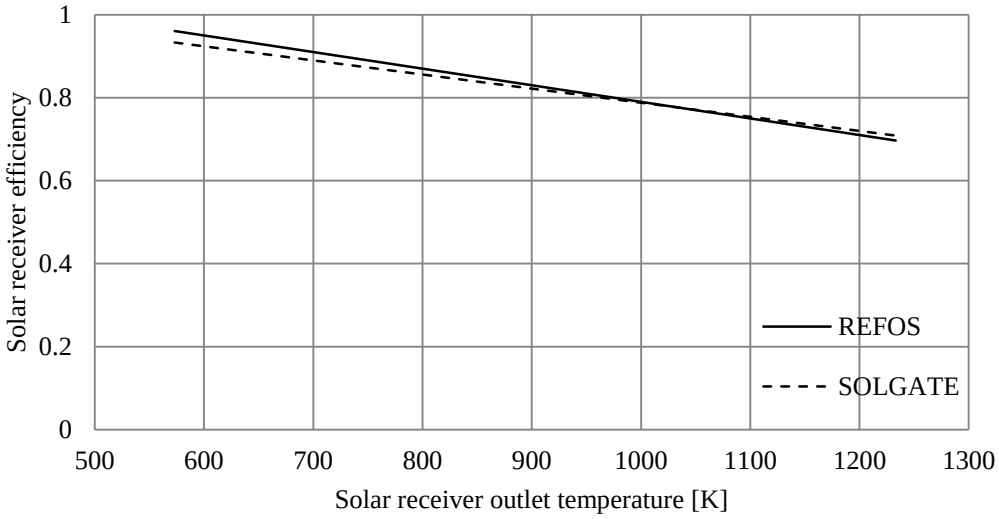

Figure 21: SOLGATE and REFOS receiver efficiency curves

Both solar receivers have very similar efficiencies across a wide range of working fluid temperatures at the solar receiver outlet. The REFOS receiver is slightly more conservative at higher solar receiver outlet temperatures, but the turbine inlet temperature of the Rover gas turbine prohibits temperatures of that magnitude. The SOLGATE receiver is slightly more conservative at the maximum allowed turbine inlet temperature, as well as the lower temperature range expected during operation. The SOLGATE receiver was thus chosen, due to its conservative efficiency values and to be consistent with the pressure drop calculations.

4.4.3 Balance of System Components

The balance of system components usually consist of valves and other piping. These components can have a significant effect on the results of the simulation, depending on the configuration and size of each component. For the conceptual design, pipes leading up and down the solar tower were added. If proven feasible, future work will include experimental testing which could require a detailed system simulation. Valves and pipe bends can only be added once more detail, regarding the actual experimental setup, is available.

For practical implementation of the Rover gas turbine into the Helio100 solar field, different plant configurations were considered. The Rover gas turbine, generator, tower and receiver were all assumed to be standard in the various configurations considered. The tower at Helio100, however, was not designed to support a gas turbine and it was decided to position the gas turbine on the ground. The pipe lengths and diameters for the initial SHGT simulation were specified as 14 m and 100 mm respectively, considering the tower height at Helio100 and the size of the Rover gas turbine's main air casing.

4.5 Flownex Solar Hybrid Model

The standard Rover gas turbine network diagram was modified to include the solar receiver and piping up and down the tower, as discussed in Section 4.4. Figure 22 shows the addition of the solar receiver and pipe elements to the standard gas turbine model.

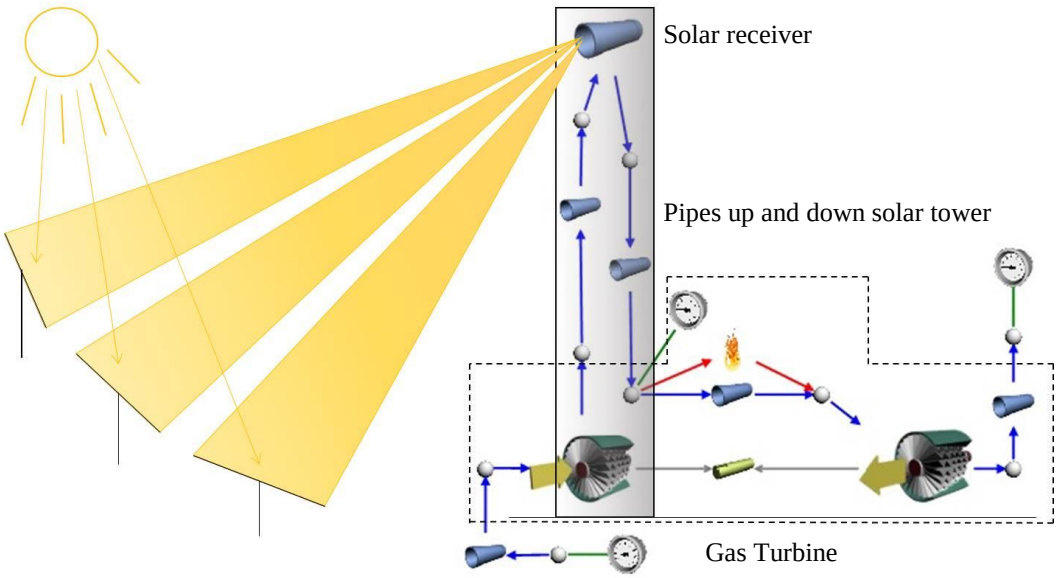

Figure 22: Solar hybrid Rover gas turbine network diagram

A sensible range of thermal energy values, specified under the receiver pipe element properties, was determined by evaluating the maximum possible solar irradiation obtainable at Helio100. An initial value for the receiver outlet temperature was required, in order to use Equation 4.11 to determine the receiver efficiency. Thereafter the solar receiver efficiency is simply multiplied by the incoming solar irradiation, $\dot{Q}_{solar}$, determined in Equation 4.5, to give the thermal energy into the working fluid. An alternative equation to determine the receiver efficiency is as follows:

$$n_{th,receiver} = \frac{\dot{Q}_{transferred}}{\dot{Q}_{solar}} = \frac{\dot{m}\, c_p\, (T_{out} - T_{in})}{\dot{Q}_{solar}} \qquad 4.12$$

Setting Equation 4.12 equal to Equation 4.11 and assuming the working fluid temperature at the receiver inlet (T_{in}) is approximately the same value as the temperature at the compressor outlet, leaves the equation with one unknown, T_{out}, to solve. Following this, the maximum thermal energy was determined.

The procedure described hereafter was repeated for every hourly measurement for the period 2013/2014 and the maximum thermal energy transferred to the working fluid was determined on January 21st. On 21 January 2014 at 12:00, hourly averaged DNI was measured as 1050 W/m^2. Using Equations C.1 to C.4 in Appendix C, the zenith angle and subsequently the optical efficiency of the heliostat field, was determined as 13.72° and 82.83 % respectively. Combining measured DNI and total solar field efficiency, as stated in Equation 4.5, the total solar irradiation of the receiver was determined to be 209.55 kW.

The outlet temperature was calculated as 722.99 K and the resulting receiver efficiency 88.21 %. The amount of solar irradiation transferred to the working fluid, being air in this case, was determined, using Equation 4.12, to be 184 kW$_{th}$. The solar irradiation transferred to the air at the solar receiver pipe element was therefore varied from 0 to 200 kW, while adjusting the fuel inlet mass flow rate to maintain a turbine inlet temperature of 1032 K. Note that the heat input, specified at the receiver pipe element, does not rely on any solar resource or heliostat data. It is merely a sequential increase in heat transferred to the working fluid, in order to evaluate the effects on the performance of the gas turbine, discussed hereafter.

5 System Simulation Validation and Results

The results obtained from the Flownex simulations are presented in this chapter. The gas turbine engine was simulated at a shaft speed of 46 krpm only, as the start-up and shutdown procedures were not considered. Firstly, the gas turbine model is validated by comparing the results against those of the one-dimensional thermodynamic model (detailed in Section 3.3.5). Thereafter, results obtained in the solar hybrid gas turbine model simulation will be presented.

5.1 Standard Gas Turbine Model Validation

In order to validate the standard Rover gas turbine model, inlet air conditions matching the inlet boundary conditions of the thermodynamic analysis were used. An ambient temperature of 30 °C and pressure of 101.325 kPa were thus specified. The system intake, as described in Section 4.2.1, was not modelled in the standard gas turbine model, in order to compare the model to the thermodynamic performance analysis, which does not account for a pressure drop before the compressor inlet. A comparison between the gas turbine model and the thermodynamic analysis results shows that the conditions at the design point are very similar, seen in Table 7.

Table 7: Gas turbine model validation

	Thermodynamic Analysis	Flownex Gas Turbine Model
Work output [kW]	43.32	42.41
Thermal efficiency [%]	10.39	10.59
Compressor efficiency [%]	69.91	70.00
Turbine efficiency [%]	85.14	84.97

Both work output values differ from the rated value of 45 kW, due to a variation in inlet conditions, which is location dependent. There is less than a 3 % difference between the standard gas turbine model and the thermodynamic analysis results for all the presented values, validating the accuracy of the gas turbine model created in Flownex.

5.2 Solar Hybrid Gas Turbine Model Results

Before considering a variation in solar resource, the effects of the additional components on the performance of the gas turbine are first evaluated. The additional components included a solar receiver and balance of system components, such as the piping up and down the tower as discussed in Section 4.4. The performance of the SHGT, with no solar irradiance, is compared to the standard Rover gas turbine performance in Table 8.

Table 8: Effect of solar components on the gas turbine performance

	Standard GT	Solar Hybrid GT
Net power output [kW]	42.41	32.50
Thermal efficiency [%]	10.59	8.71
Solar heat input [kW]	0	0
Fuel flow rate [kg/s]	0.0077	0.0072
Compressor efficiency [%]	70.00	69.66
Turbine efficiency [%]	84.97	84.79

The solar receiver and related tower piping result in an additional pressure loss of 19.34 kPa between the gas turbine's compressor and the combustion chamber. The additional pressure drop lowers the power produced by the turbine and therefore, the net power produced decreased by 23.36 %, as seen in Table 8. The decreased thermal efficiency of the solar hybrid gas turbine is attributed to the decreased net power output. Consequently the fuel flow rate decreased by 7.24 % in order to maintain the maximum turbine inlet temperature in the SHGT model.

There is clearly a decline in the performance of the solar hybridized gas turbine without solar irradiation heating the solar receiver. This scenario is analogous to night time conditions, when no solar resource is available. If the plant is required to generate electricity during the night or during days with dreary weather conditions, a by-pass valve would be required to circumvent the solar receiver and tower piping. This will prevent inefficient gas turbine power production due to additional pressure losses. When solar irradiation is available, the pressurised air is directed through- and heated by, the solar receiver. The effect of solar irradiation on the temperatures across the solar hybrid gas turbine is evident, as shown in Figure 23. The measurement zones correspond to the zones depicted in Figure 13, Section 3.3.

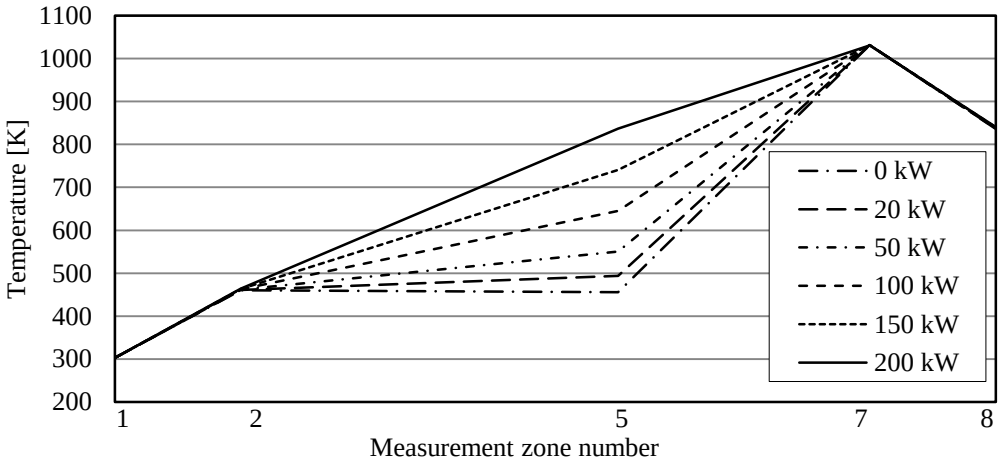

Figure 23: Temperature variation throughout the SHGT system with solar resource variance

From Figure 23 it is clear that the turbine inlet temperature is kept within the design conditions, regardless of solar irradiation magnitude (see zone 7). A steeper slope between two zones indicates that more heat is required to achieve an increase in temperature. An increase in solar irradiation results in a more gradual slope, seen between zone 5 and 7 in Figure 23. This results in a reduced heat requirement from the combustion process, leading to a reduced fuel flow rate, as seen in Figure 24. Note that thermal efficiency is defined as W_{net}/Q_{fuel}.

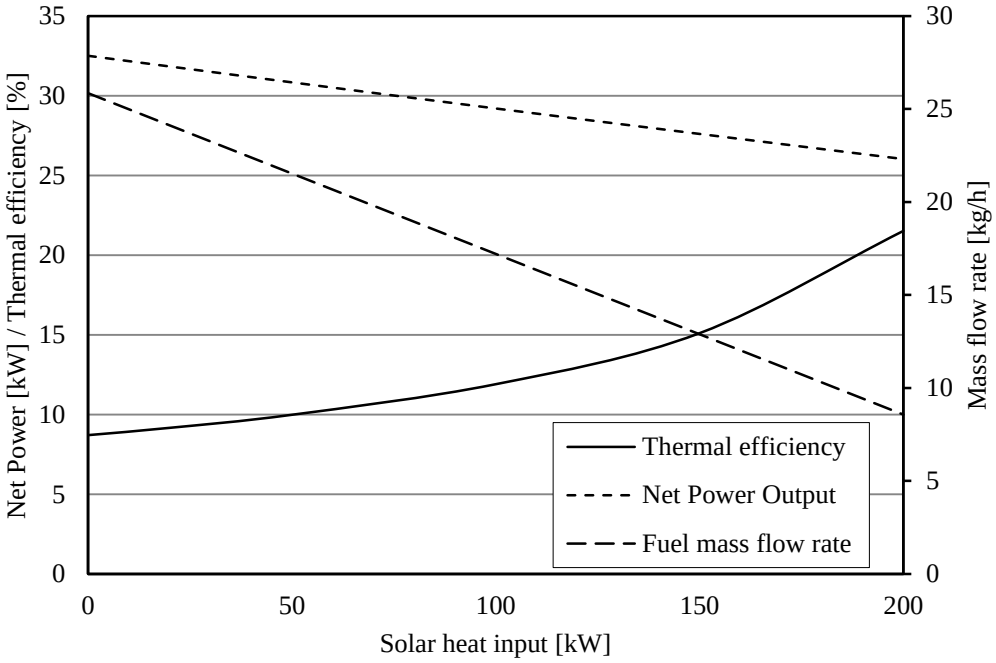

Figure 24: Effect of solar hybridization on net power output, fuel mass flow rate and thermal efficiency of the Rover gas turbine

Because the solar irradiation replaces a percentage of the fuel needed to achieve the required turbine inlet temperature, the thermal efficiency of the gas turbine increases. Even though there are fuel savings and an increase in thermal efficiency, the net power produced by the gas turbine decreases with an increase in solar irradiation.

The net power output of the gas turbine is dependent on the temperature, as well as the pressure of the air delivered to the turbine. Since the air temperature is at the designed turbine inlet temperature, shown in Figure 23, the pressure drop over the receiver and piping adversely affects the power output. The relationship between the pressure loss and power was examined at various solar irradiation magnitudes, shown in Figure 25.

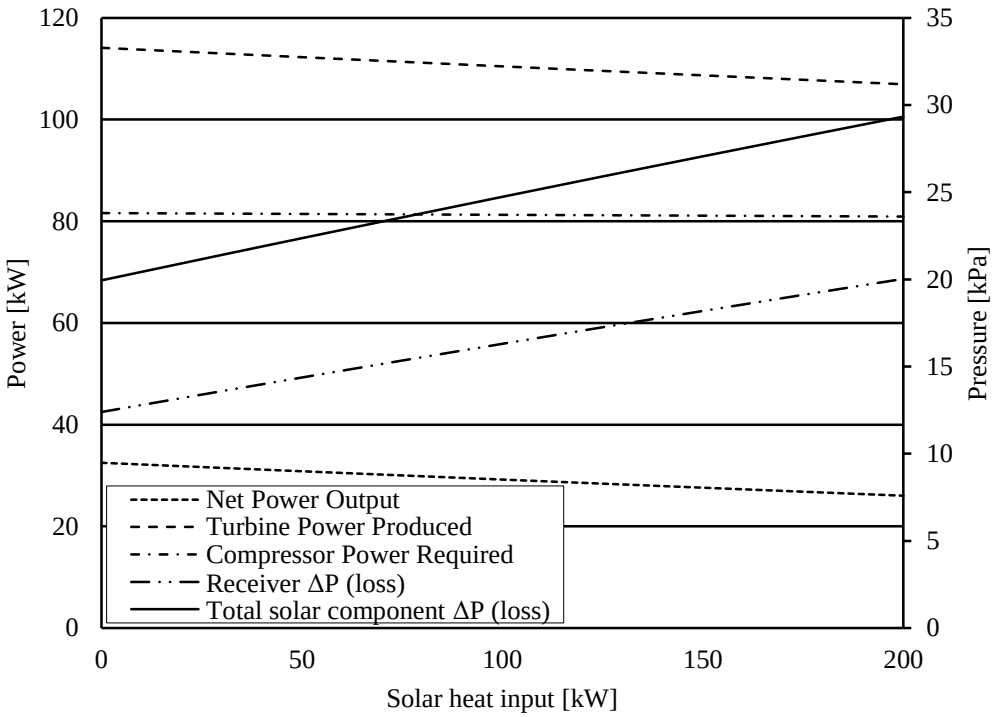

Figure 25: Variation in power and pressure losses with solar resource variance

At 0 kW, the addition of a solar receiver and piping results in a reduction of net power output, as discussed earlier. The power required to drive the compressor stays constant, regardless of the amount of solar irradiation. However, the power produced by the turbine decreases and therefore, taking the aforementioned into account, the net power produced by the gas turbine also decreases.

An increase in the pressure drop over the solar receiver and piping is evident and can be explained by considering the effect of heat addition to a gas, in this case air being the working fluid. With an increase in temperature, the density of the air will decrease. To obey the conservation of mass, assuming the flow area to be constant, the velocity of the air at the solar receiver outlet has to increase. Increased velocity has a greater effect on pressure drop than decreased density, due to the pressure drop being proportional to the dynamic pressure as indicated in Equation 4.1.

5.3 Effects of Implementing the New Compressor

Implementing the newly designed compressor of Luiten (2015), could compensate for the pressure drop created by the addition of the solarizing components. The effect that the new compressor will have on the gas turbine, as well as the solarized gas turbine with zero solar irradiation input, is summarised in Table 9.

Table 9: Effect of implementing the newly designed compressor

	Standard GT		SHGT	
	Original	New Compressor	Original	New Compressor
Work output [kW]	42.41	63.43	32.50	50.24
Thermal efficiency [%]	10.59	13.80	8.71	12.10
Compressor efficiency [%]	70.00	82.48	69.66	82.34
Turbine efficiency [%]	84.97	84.96	84.79	84.93

The newly designed compressor increases the work output and thermal efficiency of the standard gas turbine by 49.6 % and 30.3 % respectively. It has an even greater influence on the solar hybrid gas turbine by increasing the same parameters by 54.6 % and 38.9 % respectively (with no solar input). With the newly designed compressor, the solar hybrid gas turbine will produce 18.5 % more power and increase the thermal efficiency by 14.3 % with no solar irradiation, when compared to the standard Rover gas turbine. The solar heat input was again varied and its effects are shown in Figure 26.

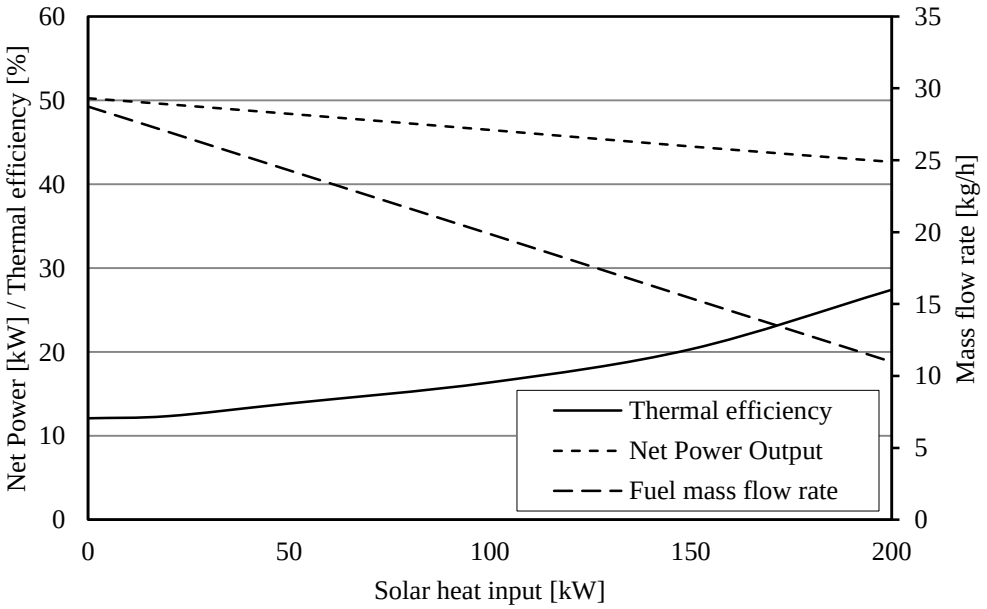

Figure 26: Effect of solar hybridization on net power output, fuel mass flow rate and thermal efficiency, implementing the new compressor

The trends in the results are a repeat of those obtained when implementing the original compressor. The major difference is the magnitude of the net power output, which is significantly higher due to the increased pressure ratio over the new compressor. The adverse pressure effects, due to the inclusion of solarizing components into the gas turbine cycle, can therefore be off-set by implementing the newly designed compressor.

6 Interconnection Component Design Methodology

The technical feasibility of a solar hybrid gas turbine was shown by means of the Flownex system simulation. The next step is to proceed with practical implementation and experiments. To assist future implementation of the SHGT, an interconnecting component, hereafter referred to as a GTR (Gas Turbine to Receiver) Link, was investigated to integrate the Rover gas turbine within a CSP system. The objective is to investigate the flow profile at the GTR-Link inlet, in order to facilitate the design process linked to the GTR-Link geometry. The GTR-Link will be connected to piping leading to and from the solar receiver and ideally a uniform flow profile should be supplied to the solar receiver. The geometry of the GTR-Link should therefore rectify any non-uniform flow profile coming out of the main air casing, if required.

Various GTR-Link implementation options exist, taking the layout of the main air casing into account. Two outlet options to extract air from the main air casing were investigated and are shown in Figure 27. Two different GTR-Link designs are required for the two outlet options and are referred to as Design Case A and Design Case B hereafter. Airflow from the compressor outlet into the main air casing (denoted Inlet in Figure 27) was kept unchanged, as this would require a redesign of the entire gas turbine engine layout.

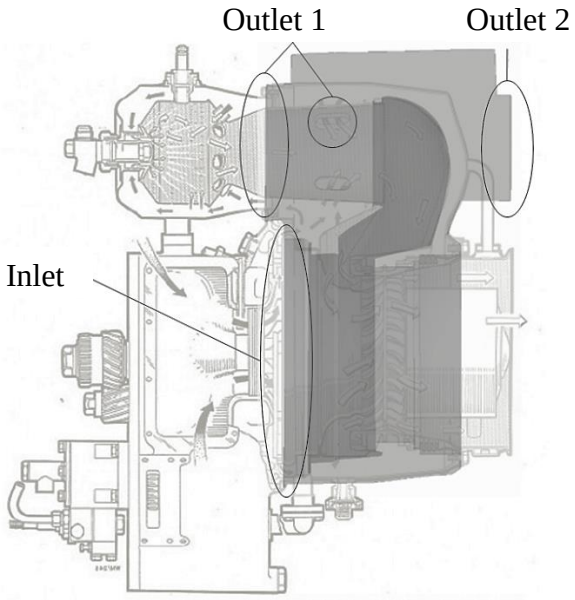

Figure 27: Outlet options from the main air casing (Adapted from Rover, 1966)

Design Case A utilizes the standard flow paths of the Rover gas turbine. The airflow exits the main air casing through the combustion chamber inlet and flame tube dilution holes (denoted outlet 1 in Figure 27).

For Design Case B, both the combustion chamber inlet and the flame tube's dilution holes are sealed and the airflow is re-directed to outlet 2. This is based on an existing modification to the original main air casing, manufactured to implement a recuperator into the Rover gas turbine engine. The modifications to implement the shell and tube heat exchanger also re-directed the airflow to outlet 2 by sealing outlet 1, as proposed in Design Case B. The air was reintroduced from the heat exchanger into the gas turbine by extending and modifying the original combustor liner and casing, similar to the modification shown in Figure 48, Section 10.1.

Data from the experimental testing done by Prinsloo (2008), revealed that the heat exchanger had an effectiveness of around 35 % and a fractional pressure drop of approximately 1.6 % over the cold side, at an engine speed of 40 krpm. He concluded that the pressure drop over the heat exchanger adversely affected the efficiency of the gas turbine, by lowering the net power output. This is similar to the findings presented in Section 5.2 and an efficient solution to extract and re-introduce the airflow into the Rover gas turbine is therefore essential.

Before attempting physical modifications to hybridize the existing gas turbine engine, the GTR-Link connection to the main air casing was evaluated by means of Computational Fluid Dynamics (CFD) simulations. Field testing is expensive due to fuel usage and changes in the test cell setup, which requires additional resources for both modifications and measurement equipment. A CFD simulation provides a quick and relatively inexpensive way to iterate design ideas by solving flow problems through algorithms and numerical analyses, showing the potential outcome of a particular design case.

The conditions at the main air casing's outlet were required to specify the GTR Link geometry, but no published data of the flow profiles inside the gas turbine casing could be found. A 3-D CAD model of the flow domain was therefore created and the flow phenomena inside the casing were validated by comparing the results of the standard case (Design Case A) to experimental data. Thereafter the flow profiles were investigated at the various outlets and the GTR-Link explored. The design process followed, as well as the report layout regarding the rest of the work, is depicted in Figure 28 below:

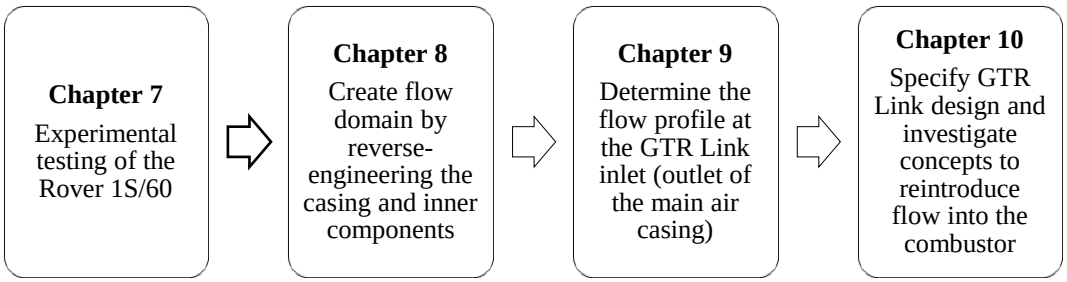

Figure 28: Schematic of the GTR Link design process

7 Rover 1S/60 Experiment Setup and Test Procedure

The experimental procedure pertaining to the performance analysis of the Rover 1S/60 gas turbine is presented in this chapter. The Rover 1S/60, currently at Stellenbosch, was overhauled during November 2014 to May 2015. The refurbishment was performed after finding cracks on the turbine blades during inspection. Upon completion of the overhaul, the gas turbine was "run-in" according to the Rover 1S/60 manual, before the tests for this study were conducted. Emphasis is placed on the analysis of the test results, comparing the results to test results obtained by Luiten (2015).

7.1 Overview of the Experimental Setup

The gas turbine is mounted on a rigid test bench and connected to a Schenck dynamometer in the test cell. All measurement instrumentation, as well as the gas turbine control system, is monitored from a computer situated in the operating room, seen in Figure 29.

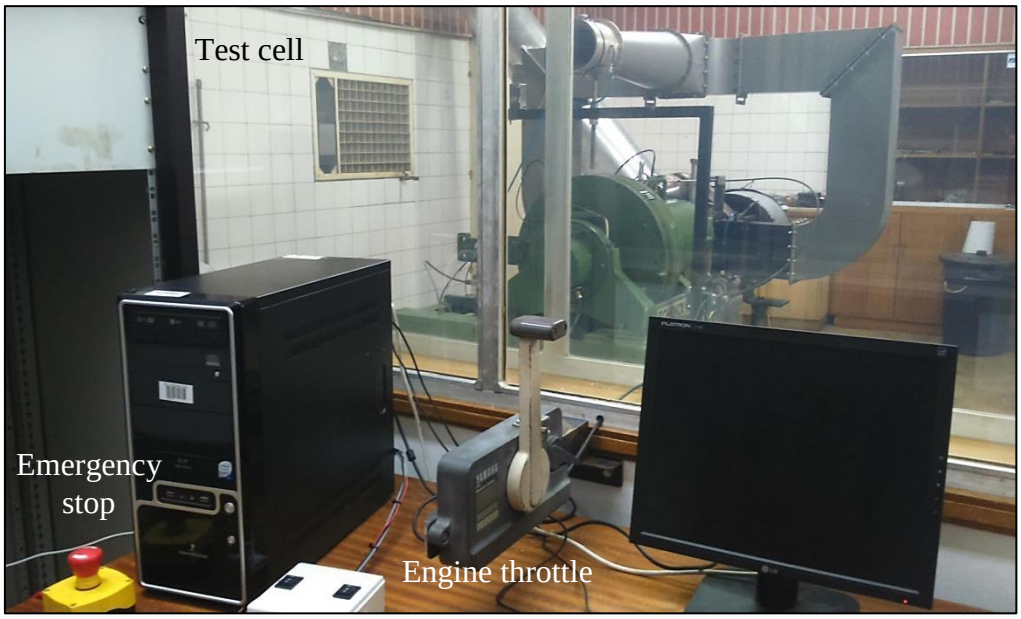

Figure 29: Test cell operating room

Safety is a priority when conducting any experiment and there are multiple safety measures taken in the test cell. Fuel is stored in a 120 L stainless steel container within the test cell and is gravity fed to the gas turbine fuel system. Two solenoid valves, both connected to the emergency shutoff valve shown in Figure 29, ensure that fuel supply to the gas turbine can be stopped in case of emergency. A large centralised fan blows fresh air into the test cell in order to replenish combusted air during gas turbine testing. Exhaust gases are removed from the test cell by an extraction vent, placed at the outlet of the gas turbine as seen in Figure 30.

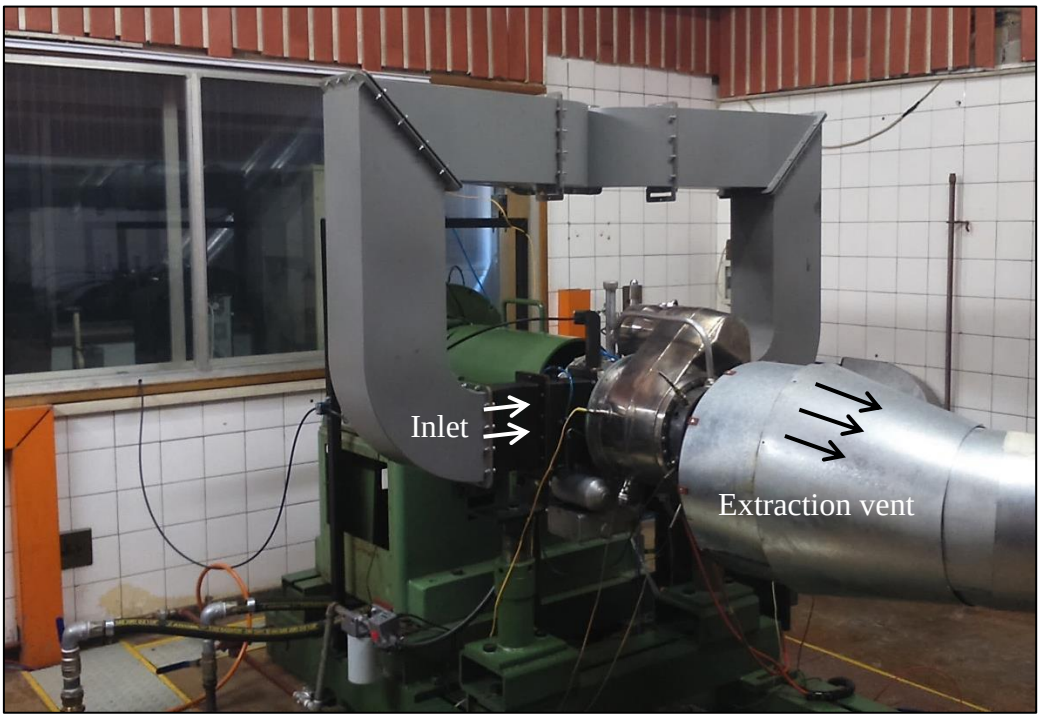

Figure 30: Rover gas turbine mounted on a test bench in the test cell

In addition to the air supply, extraction of exhaust gases and fuel supply limiting valves, various other safety measures are taken within the test cell. A smoke detector and fire detection system sounds an alarm when activated. The fire detection system then releases carbon dioxide into the test cell when activated and stops fire from spreading to adjacent test cells. Furthermore, the test bench rig was set up positioning the gas turbine axis perpendicular to the control room. If component failure occurs, debris is discharged sideways, away from the occupants in the control room. Finally, safety film similar to smash and grab window tint, is installed on the double pane window between the control room and test cell, preventing glass from shattering in the event of component failure.

7.2 Instrumentation and Data Acquisition

The instrumentation and data acquisition methodology are detailed hereafter. For this study, the temperatures and pressures coinciding with the actual measurement locations, depicted in Figure 31, are of interest. Combustor delivery pressure (P_{2b}) is situated behind the can-type combustor and is therefore not visible in Figure 31 (a). The exhaust gas temperature (T_{08}) measurement probes are visible on the right hand side of Figure 31 (a).

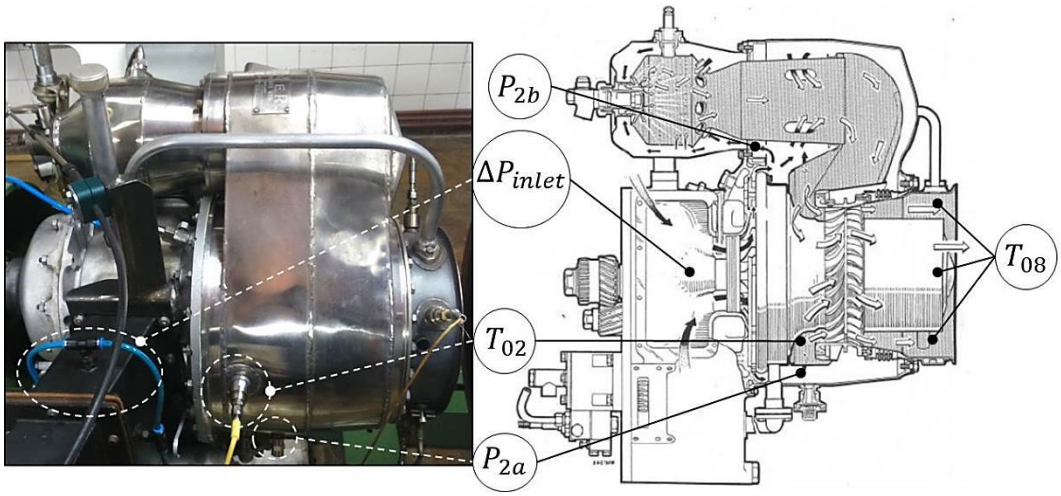

(a) (b)

Figure 31: Measurement locations on the actual (a) and a schematic (b) of the Rover gas turbine (Adapted from Rover, 1966)

All the instrumentation is connected to an Allen Bradley MicroLogix1200 programmable logic controller (PLC). The PLC serves as interpreter between the instrumentation and Engine Test Automation (ETA), a software package used in the control room. The software allows the user to calibrate the incoming input and output signals, data acquisition during testing and operational control of the gas turbine. Recalibration of the instrumentation is thus not required for every field test, since the correlation between the input signal and required value of each instrumentation channel is saved in ETA.

K-type thermocouples were used for temperature measurements. They are accurate within approximately 0.75 % and operate within a range of -270 °C to 1260 °C (REOTEMP Instruments, 2011). Although the thermocouples were calibrated by the supplier, additional calibration was done by comparing the measured value with that measured by a temperature probe. A linear regression between the output voltage and correct temperature reading was saved in ETA.

The pressure at the throat of the intake system (ΔP_{inlet}) was measured with a WIKA A2G-50 differential pressure transducer. The WIKA A2G-50 has an operating range upper limit of 7 kPa and a measuring uncertainty of 1.5 %. Due to the low operating range, a Betz manometer was used to calibrate the transducer. All other static pressures ($P_{2a,b}$) were measured using WIKI A-10 type pressure transducers, having an uncertainty of approximately 0.5 %. To calibrate the WIKI A-10 pressure transducers, a hand pump and certified analogue pressure gauge were used. A T-piece connected the analogue pressure gauge and pressure transducer. Pressure readings across the transducer's operating range were captured in ETA and compared to the measured values from the analogue pressure gauge. Again a linear regression, this time between the output voltage and correct pressure reading, was saved in ETA.

Pressure measurement locations are dependent on the physical arrangement of the internal components of the gas turbine and thus prefabricated measurement taps, refer to Figure 31, were used. All instrument calibration was performed by Luiten (2015) and Zhang (2015).

7.3 Test Procedure

After ensuring all the instrumentation is connected properly, a final safety check should be performed to ensure that the test cell is evacuated, supply and extraction fans are switched on and that the manual fuel supply valve is open. The test cell alarms are then activated and Rover gas turbine tests can commence. The start-up and shut-down procedures of the Rover gas turbine are as follow:

7.3.1 Start-up Procedure

- In ETA, switch on the master switch, followed by the starter motor and igniter.
- Monitor the fuel pressure and introduce fuel with the engine throttle, shown in Figure 29, when the fuel pressure reaches 2 bar.
- The gas turbine shaft speed should now increase and the igniter and starter motor can be switched off.
- The gas turbine will continue to increase and should stabilise at an operating speed of 46 krpm.

Data is logged within ETA by creating a new data entry and starting the data acquisition when required. Data for this study was recorded only when operating the gas turbine at its design speed of 46 krpm. However, start-up and shut-down procedures can be recorded and analysed if needed.

7.3.2 Shut-down Procedure

- Remove the dynamometer load (if any).
- Switch off the master switch, to close all fuel supply solenoids.
- Close the engine throttle by pushing the lever forward.
- Monitor all temperatures and enter the test cell when the gas turbine has cooled down.

In case of emergency, press the emergency stop button shown in Figure 29. Close the engine throttle and wait for the test cell and gas turbine to cool down before inspecting any possible failures.

7.4 Data Analysis

Two data sets were utilised in the present study. The first data set is from experimental tests performed on the Rover gas turbine before it was overhauled and the other set from tests after the overhaul, referred to as the old and new data set. The data sets consist of multiple experimental tests and each set contains the following measured values: the inlet differential pressure (ΔP_{inlet}), post-compressor pressure (P_{2a}) or combustor delivery pressure (P_{2b}), post-compressor temperature (T_{02}) and exhaust temperature (T_{08}). The static pressure measurement point was changed after the overhaul to measure combustor delivery pressure (P_{2b}), as opposed to measuring the pressure directly after the compressor stage (P_{2a}).

The two data sets were compared to assess the effects of the overhaul and the overlapping ranges were used to establish a final value range for each measured parameter. The statistical analysis was limited to experimental results obtained close to the design point speed, in the range of 45 – 47 krpm. The limitation ensures results obtained during the start-up and shut-off procedure is omitted, as these results will adversely influence the analysis and lead to incorrect conclusions about the data sets.

Various other sources could contribute to errors and uncertainties in data acquisition processes. These include, but are not limited to, the instrumentation, measurement process, operator skill, sampling issues and the environment. A valid interpretation of the data can only exist when the influence of uncertainties within the data set are acknowledged. According to Bell (2011), there are two approaches to estimate uncertainties within a data set. Type-A evaluations use statistics to estimate uncertainties from a data set. Type-B evaluates uncertainty from any other information available during the data acquisition process. The information could be from instrument calibration, from the manufacturer's specifications or from published information.

The calibration process described in Section 7.2, corrects for uncertainty contributions by the measurement instrumentation and the data acquisition unit, thereby eliminating Type-B uncertainties within the data sets. The remaining Type-A uncertainty of the recorded measurements can be evaluated by fitting a probability density function (PDF) to the data. The likelihood of a parameter occurring within a certain range of values can be evaluated by integrating the PDF.

In order to determine the PDF for each parameter, the logged measurements were sorted in ascending order and grouped into bins, sized in relation to the maximum and minimum values of the specific measurement group. A plot of the bins forms a histogram, as seen in the example given in Figure 32 (a), to which the PDF is fitted.

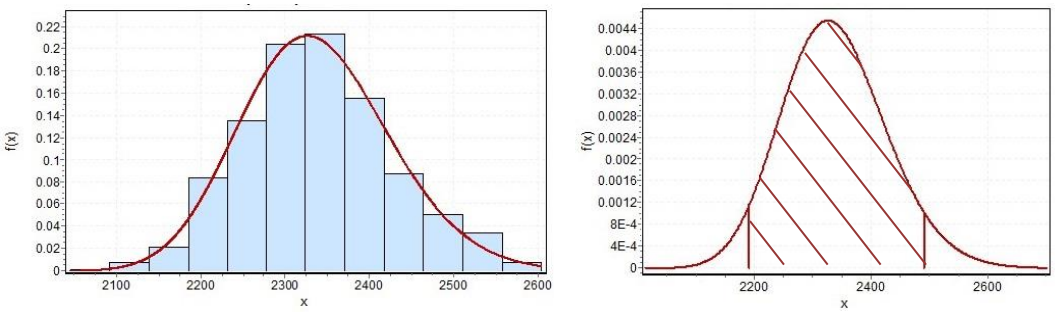

(a) (b)

Figure 32: Example of a frequency distribution (a) and fitted probability density function (b)

The area underneath the function represents the possibility of the data set to fall within a specified range of values, as seen in Figure 32 (b). To fit a probability function to the data set, EasyFitXL (MathWave Technologies, 2015) was used. The program, installed as an add-in within Microsoft Excel, iteratively fits more than 50 probability distribution functions to the data set and determines the best fit by means of the Chi-Squared goodness of fit test, given by DeCoursey (2003):

$$\chi^2_{calculated} = \sum \frac{(O_i - E_i)^2}{E_i} \tag{7.1}$$

where the O_i is the observed and E_i the expected frequency of bin i. The expected frequency is determined by:

$$E_i = F(x_h) - F(x_l) \tag{7.2}$$

where F denotes the distribution function at the higher limit (x_h) and the lower limit (x_l) of the bin. The value calculated in Equation 7.1 is compared to a critical value at a chosen level of significance. If it is larger than the critical value, the null hypothesis, stating that the data follows the specified distribution, is rejected. EasyFitXL calculates the critical value at significance levels of 0.2, 0.1, 0.05, 0.02 and 0.01, where a significance level of 0.05 relates to a 5 % chance of rejecting the null hypothesis. The calculated value is compared to each critical value, in order to establish whether or not to reject the null hypothesis.

It was found that in both the old and new data sets only the differential pressure measurement's null hypotheses were accepted, according to the Chi-Squared goodness of fit test. The other measured parameters did not follow a given distribution shape within the specified significance levels. This could be due to outliers affecting the data, the operating speed limitation being too wide or an indication that a larger data sample is required.

Outliers within the remaining data sets were removed and PDF's were again fitted to each measured parameter's data set. To inspect how accurately the data set of a measured parameter follows the proposed PDF, a P-P Plot was utilised, shown in Figure 33.

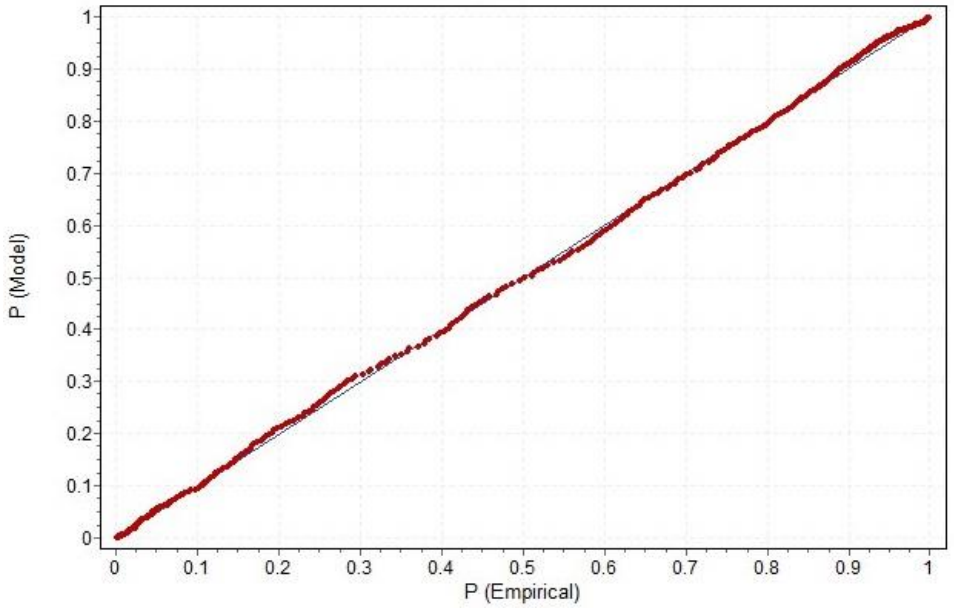

Figure 33: P-P Plot of the Pearson distribution fitted to measured pressure differential data

The PP-Plot is another measure to evaluate how well a selected distribution fits the measured data. A distribution is deemed correct if it is approximately linear along the diagonal line representing the reference of the PDF distribution. The PP-Plots of all the measured parameters, excluding the differential pressure, can be viewed in Appendix E.

7.5 Test Results

After establishing an appropriate PDF for each measured parameter, a range adhering to a 90 % confidence band was estimated for each data set. The experimental test results of the old data set are shown below in Table 10.

Table 10: Experimental testing results summary: Before Overhaul

Measured Parameter	Probability Distribution	Value Range	Probability of Occurrence
ΔP_{inlet} [kPa]	Pearson 5	2.05-2.32	90.14 %
P_{2a} [kPa]	Cauchy	130-166	90.65 %
T_{02} [°C]	Beta	183-215	90.77 %
T_{08} [°C]	Johnson SB	420-478	90.45 %

Each measurement parameters' range in the old and the new data set were compared and the overlapping range taken as the final range. The post-compressor pressure in each of the two data sets was not comparable due to a change in the measurement location. Results of the new data set are summarised in Table 19, Appendix E.

Luiten (2015) performed experimental tests on the Rover gas turbine before its overhaul. The resultant parameter ranges, of the old data set, found in this study are compared to his findings in Table 11.

Table 11: Experimental testing results comparison

Measured Parameter	Value Range	Test Results by Luiten (2015)
ΔP_{inlet} [kPa]	2.05-2.32	1.83
$P_{2,a}$ [kPa]	130-166	163.89
T_{02} [°C]	183-215	206.85
T_{08} [°C]	420-478	468.1

The test results compare well to the results obtained by Luiten (2015). The post-compressor pressure and temperature, as well as the exhaust gas temperature, fell within the 90 % confidence band determined in this study. The differential pressure of Luiten, however, was 10.73 % lower than the minimum value determined for the range. The larger data sample set used in the present study could have an effect on the value range shown in Table 11.

The resultant final parameter ranges, within a 90 % confidence band, is discussed further in Section 9.1. There the model predicting air flow through the gas turbine casing, presented next, is validated with the experimental results.

8 Reverse-engineering the Main Air Casing

The inlet boundary conditions of the GTR Link were determined by evaluating the conditions through the main air casing of the gas turbine. The main air casing, inner volute, flame tube, turbine nozzle and shroud ring, as well as parts of the compressor housing, heat shield, bearing housing support plate and exhaust bellows were reverse-engineered in order to obtain the correct flow domain for analysis. In this chapter the process to obtain the flow domain for CFD analysis and the CFD setup is explained.

8.1 Flow Domain Creation

The existing Rover 1S/60 gas turbine casing was measured with a GOM camera 2. This is an optical measurement process which work as follows: The camera is calibrated to achieve a measurement deviation of less than 0.1 mm. The object intended for measurement, in this case the main air casing and inner volute, is sprayed with a white powder to reflect as much light as possible back to the camera. Black dotted stickers are placed on the casing, which the camera recognises and uses as a referencing system. Using the dots as references, images from the camera are converted to point cloud data and a model is built in real time.

Surfaces are then fitted over the point cloud data, using various sectioning techniques to extract the casing and volute profiles. The process of obtaining the inner volute, from point cloud data to complete surface model, is shown in Figure 34. PowerSHAPE (Delcam, 2014) was used to fit the surfaces over the point cloud data.

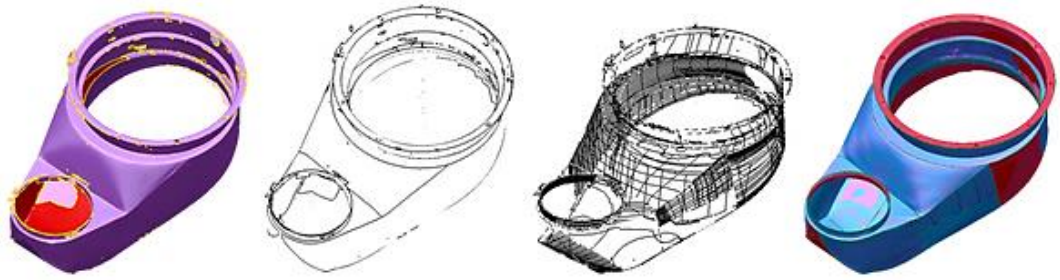

Figure 34: Inner Volute: Point Cloud Data to Surface Model

The surface models were converted to solid models, from which the flow domains were extracted. Figure 35 shows the solid model and fluid domain of the main air casing.

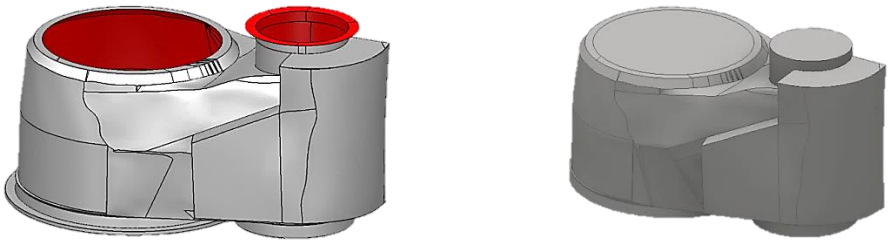

(a) (b)

Figure 35: Main air casing solid model (a) and flow domain (b)

Simplified geometries of the remaining component's flow domains were created with Inventor Professional (AUTODESK, 2016). All the components, except for the main air casing, were assembled to create the inner flow domain. After that the inner flow domain was subtracted from the main air casing's flow domain, generating the flow domain required for simulation purposes. The final flow domain is shown in Figure 36.

(a) (b)

Figure 36: Main air casing flow domain (a) and a section view of the flow domain (b)

The sectional view is identical to the extraction shown in Figure 27, illustrating where the main air casing is located within the Rover gas turbine assembly. For further clarification, regarding the components that form the inner flow domain, refer to Appendix F.

8.2 Numerical analysis

The objective of the numerical analysis is to determine the velocity and pressure flow patterns at the main air casing's outlet, while also investigating the effect of implementing the new compressor. Workbench 14.5.7 (ANSYS Inc, 2013b) was used as a CFD project management platform, from where the meshing application and Fluent, the fluid flow solver, were launched. The mesh generation and quality control process, as well as the solution setup in Fluent, are detailed below.

8.2.1 Mesh Generation and Quality Control

A mesh divides the flow domain into discrete cells, enabling the solver to solve equations at each cell. Adjacent elements influence each other and if the model is meshed incorrectly the solution will be erroneous. It is therefore important, not only to generate the correct type of mesh, but to employ quality control methods which ensure the best possible chance for an accurate solution.

Various meshing processes can be followed, depending on the shape of the flow domain. For the main air casing's flow domain, a tetrahedron mesh using an advancing front patch conforming algorithm was chosen, where after several refinements were made. Initially, small faces fitted to the point cloud data, in order to capture the correct shape of the domain, caused many mesh elements to generate around the edges of the small faces. This was an unnecessary refinement of the mesh and the problem was solved by creating a virtual topology to merge small faces and edges.

The flow inside the casing was expected to be turbulent and due to the chosen turbulence model, discussed in Section 8.2.2, inflation control was applied to capture flow in the boundary layer. The inflation was specified based on the first layer boundary height, which was determined by assuming a y^+ value of 100. In turbulent flow problems, when a wall function approach is sufficient, the y^+ value typically lies between 30 and 500 (Versteeg and Malalasekera, 2007). The first boundary layer height was determined to be 0.635 mm and a sample calculation can be viewed in Appendix G. The generated mesh and a detailed view, that showcases the boundary layer, are depicted in Figure 37.

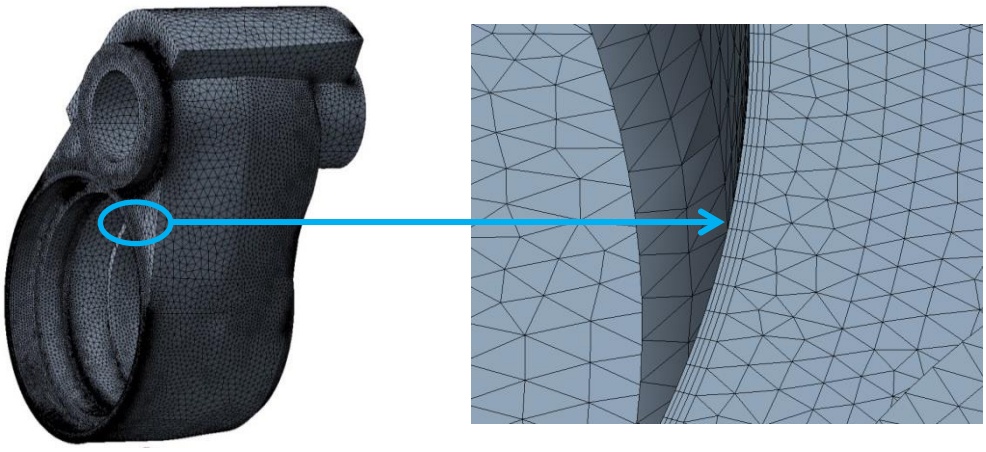

(a) (b)

Figure 37: Mesh of flow domain (a) and the inflation layer on the inlet boundary (b)

For the two design cases specified in Chapter 6, different meshes were created, based on the different outlet boundary conditions depicted in Figure 27. When boundary conditions have to be specified on a certain face, a named selection is created for the relevant face. The meshing application detects and grows inflation layers from all the named selections. The difference after changing the named selection is evident at outlet 2, as seen in Figure 38. The inflation layer can clearly be seen around the edge of the outlet, after performing the refinement.

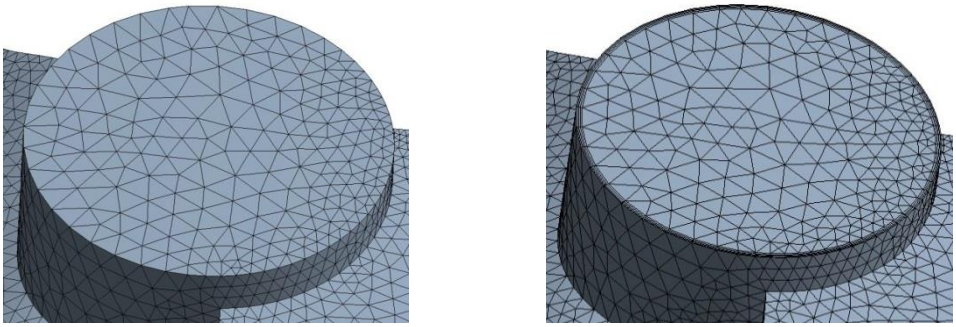

(a) (b)

Figure 38: Outlet 2 in Design Case A (a) compared to Design Case B where it is specified as a boundary condition (b)

Various quality parameters exist within the meshing application. Two of the most common quality parameters are orthogonality and skewness, with the values of these parameters ranging between 0 and 1. The minimum orthogonality of the mesh should be higher than 0.01, while the average should be as close to 1 as possible (ANSYS Inc, 2015). The skewness, however, should be as close to 0 as possible. The mesh quality of the two design cases are shown in Table 12.

Table 12: Mesh quality control parameters

	Design Case A	Design Case B
Orthogonality Minimum	0.0462	0.0543
Orthogonality Average	0.8462	0.8470
Skewness	0.2750	0.2689

The minimum orthogonality in both cases is well above the suggested minimum and the averages are close to 1. The skewness is also reasonably close to zero and the quality of the generated meshes is therefore acceptable. Another mesh quality parameter is mesh independence, which is achieved when a refinement in the mesh no longer improves the accuracy of the results. Mesh independence of the solutions of Design Case A and Design Case B are evaluated in Chapter 9.

8.2.2 Solution Setup

After a suitable mesh was applied to the flow domain, the solution setup within Fluent was specified. The solver was set to pressure-based solving and air was selected as the working fluid from the materials database. Next, the turbulence model was selected.

While various turbulence models exist within Fluent, each is different in its boundary flow solving approaches. Da Soghe *et al.* (2010) investigated various turbulence models to study rotor-stator cavity flows, the secondary air system in gas turbines. They found that the SST k-ω turbulence model agreed well with experimental results and that it provided a good trade-off between computational cost and numerical accuracy. Compressible flow in the diffuser duct of an afterburner unit of a jet engine was simulated by Bheemaraddi and Kumarappa (2014). The SST k-ω turbulence model was considered satisfactory as it provided good flow predictions for flow characteristics within the diffuser.

Turbulence models used to predict flow performance inside centrifugal pumps were also investigated. Although the working fluid differs, the complex internal flows within the pump volute also require appropriate turbulence models to predict the performance of the pump accurately. A centrifugal pump volute was investigated by Shah *et al.* (2010) and it was found that the SST k-ω turbulence model provided better results than other models. Shojaeefard *et al.* (2012) performed a parametric study on the effects of different impeller geometrical characteristics on the performance of a centrifugal pump. The pump volute was included in the CFD simulations and again it was found that the SST k-ω turbulence model provided better results than other models.

The SST model uses the k-ε model in regions away from the wall, while using the k-ω model in near wall regions, thus requiring inflation control on the boundary layer, as discussed in the previous section. The SST k-ω turbulence model was therefore selected for the current flow problem. A schematic of the boundary locations are shown in Figure 39 and are described below.

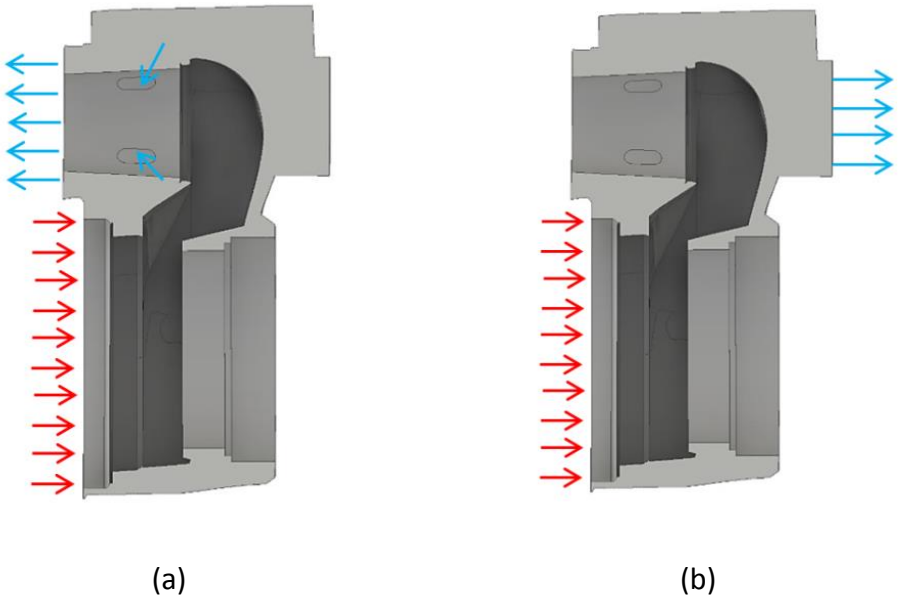

Figure 39: Boundary conditions of Design Case A (a) and Design Case B (b)

The inlet boundary is the region where the working fluid exits the compressor's diffuser and enters the main air casing. The boundary condition was specified as a Pressure-Inlet orientated normal to the boundary. The total pressure and temperature at the inlet was specified as 283.71 kPa and 445.17 K respectively, from simulation results obtained by Luiten (2015). Neither the inlet or outlet mass flow rates were specified as it was predicted by the simulations.

An unknown parameter at the inlet boundary was the turbulence intensity. It is defined as the average root-mean-square velocity as a ratio of the mean velocity of a fluid. A low turbulent intensity is considered in the region of 1 % while high intensities fall in the region of 10 %, according to ANSYS (2013a). An average turbulent intensity of 5 % and turbulent viscosity of 10 % was selected, in agreement with the values found by Shaw et al. (1966) and Camp and Shin (1994).

The main air casing outlet velocity and pressure profiles are the desired solutions from the numerical analysis. Fluent however, requires the user to specify outlet boundary conditions. The outlet was initially specified as an Outflow boundary, a condition that requires only the fraction of mass flow rate through the boundary to be specified, but the simulations were found to be unstable.

Consequently a Pressure-Outlet boundary condition was specified, with an initial static pressure estimate of 161 kPa. The combustor delivery pressure measurement obtained from the test data, discussed in Section 7.5, was used as an estimate. Note that the pressure outlet value was just an initial estimate and that the solver determines the final pressure and pressure profile at the outlet.

The last boundary condition specified was the flame tube surface temperature, assumed to be constant after sufficient running time. Since investigating the cooling effects of the dilution holes are beyond the scope of the current study, the tube surface temperature was taken as a mean value between the flame temperature in the combustion chamber and the maximum turbine inlet temperature. The flame temperature of kerosene is approximately 2093 °C (Chu, 2006), while the maximum inlet temperature is 1032 K (Rover, 1966). This results in an average flame tube surface temperature of about 1700 K. In Design Case A, the dilution holes were also specified as pressure outlets, with exactly the same parameters as the boundary conditions at the main air casing outlet.

Installing the newly designed compressor, theoretically improved the gas turbine's performance. The inlet and outlet boundary conditions were adjusted accordingly to solve the relevant flow through the casing. The inlet pressure was set to 348.56 kPa, at a temperature of 428.82 K, obtained from the results of Luiten (2015). No test data of the new compressor was available to estimate the static pressure at the main air casing's outlet. The percentage pressure drop through the casing, implementing the standard compressor, was thus used as an initial estimate. The outlet static pressure was determined as 195.2 kPa. The flame tube's boundary conditions remained unchanged, as it is not directly affected by the performance of the new compressor.

9 Simulation Results

The results obtained from the CFD simulations are presented in this chapter. Before investigating the velocity and pressure profiles, the validity of the predicted flow solutions was examined by inspecting three independent monitors.

9.1 Solution Validation

The following validation process illustrates how the solution obtained from Design Case A, incorporating the original compressor, was validated. All other solutions obtained were validated in a similar manner. The experimental results however, are only applicable to the first simulated case and were thus omitted when validating the other cases. The solution's convergence, mesh independence and comparison to experimental results are detailed below.

9.1.1 Residual Convergence

Convergence is achieved when the residuals stop changing at an acceptable value, which varies depending on the flow problem. Design Case A's residuals, calculated throughout the solving process, are shown in Figure 40. The results shown were obtained for Mesh 3, containing 1.69 x 10^6 elements, as discussed in Section 9.1.2.

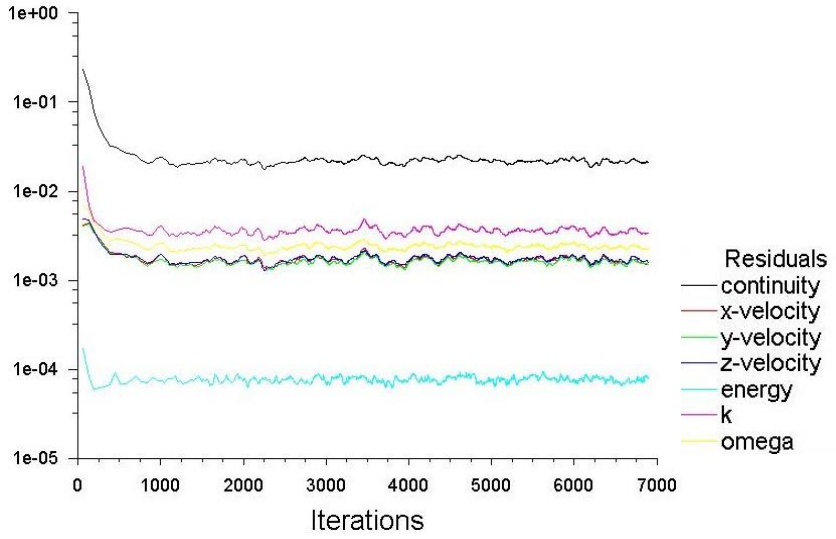

Figure 40: Solution scaled residuals

The trends of the residuals, depicted in Figure 40, suggest that the solution has converged. The minor fluctuations in the residuals are attributed to the extremely disordered fluid motion, a characteristic of turbulent flow. All further results were examined after the convergence of the residuals.

9.1.2 Mesh Independence and Conservation of Mass

The solution predicting flow phenomena in the main air casing should also be independent of the mesh size. This was established by comparing the mass flow rate through the casing at different mesh element sizes. The mass flow rate was monitored because it was not specified as a boundary condition and the Rover manual indicated that an approximate value of 0.6 kg/s could be expected. The mass flow rate at the outlet, versus the number of mesh elements from Design Case A are shown in Figure 41. Similar results for Design Case B can be found in Appendix H.1.

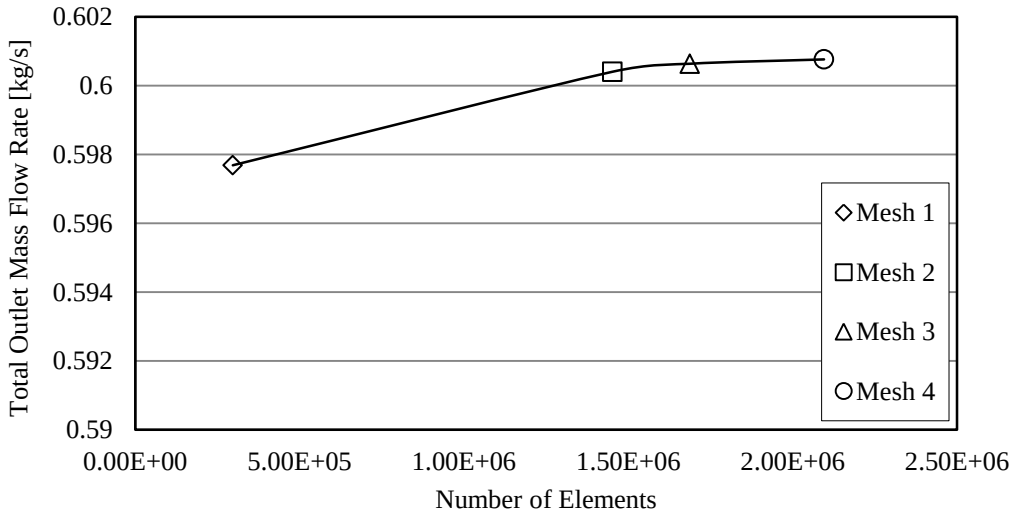

Figure 41: Total outlet mass flow rate vs. the number of elements in the mesh

An increased mass flow rate value was predicted by refining the mesh from a coarse Mesh 1 to Mesh 2. The refinement increased the number of elements by approximately five times, also increasing the computational requirements significantly. Further refinements in the mesh, referred to as Mesh 3 and Mesh 4 in Figure 41, led to less significant variations in the results. The mass flow rate changed by 0.02 % from Mesh 3 to Mesh 4, indicating that mesh independence has been achieved. All simulation results discussed hereafter were obtained from Mesh 3.

A flux report, providing the difference between the inlet and outlet mass flow rates, reported a net mass flow rate of -0.0046 % and -0.012 % for Design Case A and Design Case B respectively. This confirmed that both solutions adhered to the conservation of mass. The mass flow rate passing through the dilution holes were investigated for Design Case A. It was found that 29.76 % of the total air flows through the dilution holes. This is in agreement with findings by Lefebvre (1998), who stated that the amount of air used for dilution in gas turbine combustion varies between 20 % and 40 % of the total airflow.

9.1.3 Experimental Validation

The final validation, applicable only to Design Case A, representing the original compressor, compares the values predicted by the solution to the experimental results found during testing. The predicted results for temperature and pressure were examined in the regions of the main air casing, where the measurements were taken during experimental testing.

In order to compare the measured differential pressure (ΔP_{inlet}) to the mass flow rate obtained in the simulated solution, the following equation, specified in the British Standard (BS 848, 1997), was used:

$$\dot{m}_{air} = \alpha\varepsilon \frac{\pi D^2}{4} \sqrt{2 \rho \Delta P_{inlet}} \tag{9.1}$$

where $\alpha\varepsilon$ is a coefficient dependent on the Reynolds number, at the inlet of the intake system and D is the duct diameter at the measurement position, specified as 0.11 m by Prinsloo (2008). The density of the air was taken as 1.18 kg/m^3, at an average inlet air temperature of 27 °C. The coefficient $\alpha\varepsilon$ was taken as 0.96, since the experimental results were obtained from the gas turbine design point speed of 46 krpm. A comparison of the predicted values, to the range of values within a 90 % confidence band from experimental testing, is shown in Table 13.

Table 13: Predicted solution compared to experimental results

Measured Parameter	Experimental value	Predicted Value
$\dot{m}_{air}$ [kg/s]	0.65 – 0.67	0.60
$P_{2,a}$[kPa]	130 – 166	182.93
$P_{2,b}$ [kPa]	150 – 161	180.92
T_{02} [K]	463 – 488	440.83
T_{08} [K]	695 – 718	N/A

The solution predicts the values reasonably well when compared to the experimental values. The mass flow rate and post compressor temperature are under predicted by 7.69 % and 11.74 % respectively. The post compressor- and combustor delivery pressure, however, are over predicted by 10.20 % and 12.37 %, respectively. The experimental values could be influenced by an inconsistent inlet air temperature. It is specified as a constant inlet boundary condition within the simulations, but is actually dependent on the ambient air temperature in the test cell. When performing the experiment, the air temperature within the test cell fluctuated between 16.9 °C and 32.2 °C. The fluctuation in temperature is attributed to heat radiation from the gas turbine, off-set by cooler air supplied to the test cell by air vents. The inlet air temperature affects the density of the air, consequently affecting the air temperature and pressure after compression.

In order to determine the pressure and velocity profiles, the predicted solution is within an acceptable range of the experimental values, given the fluctuating inlet air temperature observed in the experimental setup.

9.2 Standard Compressor Results

Following confirmation of the convergence of the residuals, mesh independence of the solution and the conservation of mass flow through the casing, the velocity and pressure profiles were examined. Figure 42 depicts the velocity stream lines and velocity contour predicted at outlet 1, if the original standard compressor is installed.

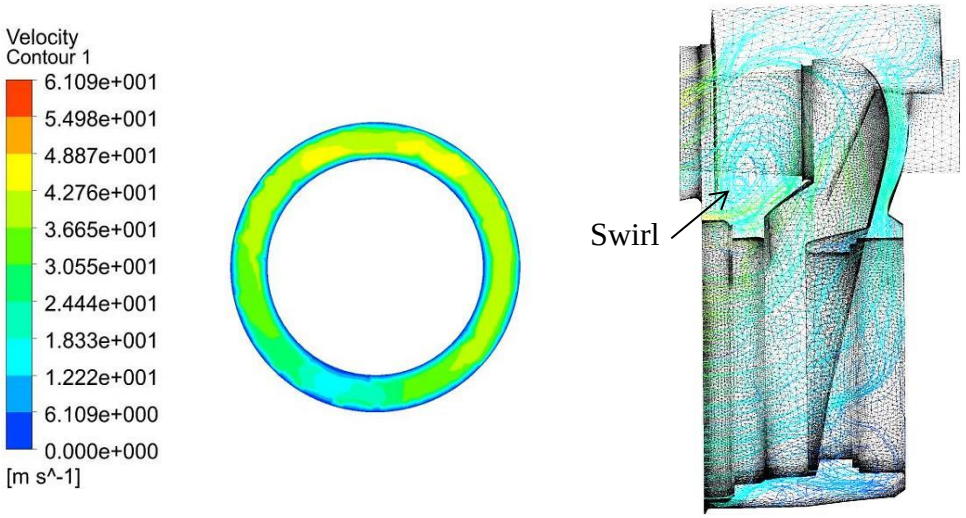

(a) (b)

Figure 42: Velocity contour at outlet 1 (a) and streamlines through casing (b)

Figure 42 (a) indicates a relatively dispersed velocity profile, with higher velocity regions at the top of the profile. Deceleration in the flow, due to recirculation, is predicted at the bottom of the casing as seen in Figure 42 (b). Swirl is apparent just before the outlet, as seen at the bottom of the flame tube, which might contribute to a lower velocity region forming at the bottom of the outlet. The flow prediction of Design Case B is shown in Figure 43.

The predicted velocity contour, Figure 43 (a), shows that the flow is circumferentially fairly, evenly distributed, with most of the high velocity flow located at the centre of the outlet. The flow does not swirl before the outlet, contributing to more circumferentially distributed flow in contrast to results of Design Case A, Figure 42 (a). Recirculation in the casing is still visible, as shown at the bottom of Figure 43 (b). An increase in the velocity magnitude between the inner volute and the main air casing was found, encircled in Figure 43 (b).

This is as a result of directing all the air flow through outlet 2, at an increased mass flow rate, by sealing outlet 1 and the dilution holes.

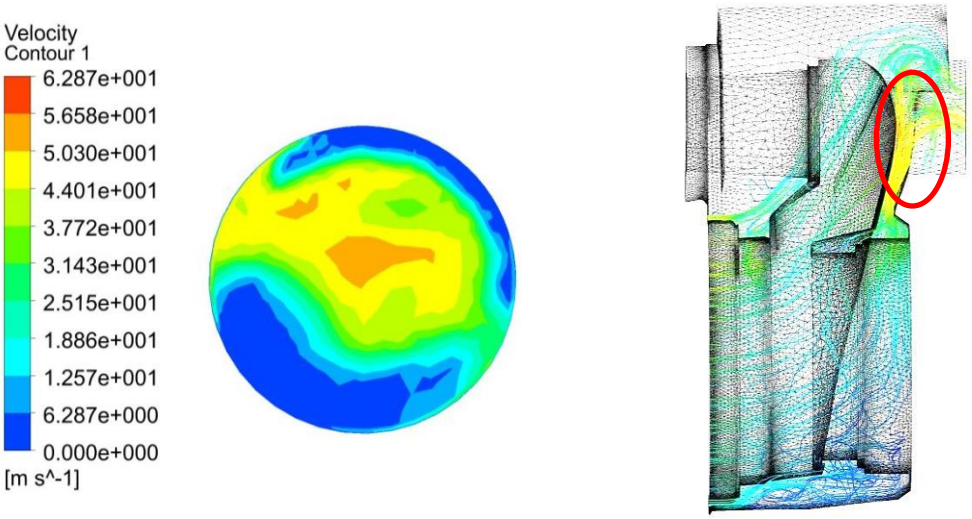

Figure 43: Velocity contour at outlet 2 (a) and streamlines through casing (b)

A comparison of the pressure distributions predicted at the two outlets, is shown in Figure 44. The pressure contours were scaled locally, due to the minor variation in pressure across the outlets.

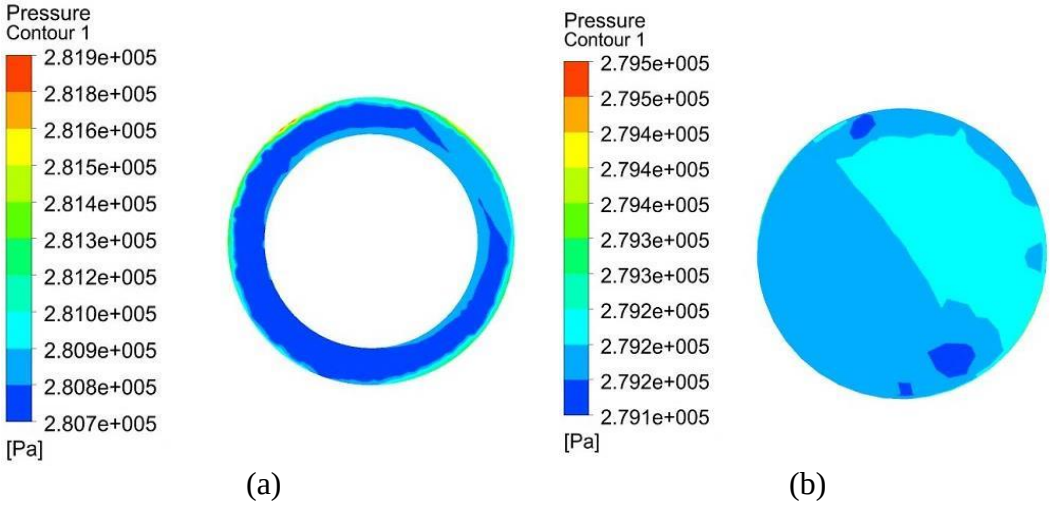

Figure 44: Comparison of the pressure contours at outlet 1 (a) and outlet 2 (b)

There is a much smaller variation in pressure magnitude, compared to the velocity distributions. A variation of 1.2 kPa and 0.4 kPa is apparent in both Figure 44 (a) and (b), respectively. This is less than 1 % of the average total pressure in both design cases and the profiles are thus viewed as uniform.

Continuing with the solar hybrid application in mind, Design Case B was investigated further. The velocity and pressure profiles indicate that a more uniform distribution is predicted at outlet 2. Closing the dilution holes result in increased mass flow rate through the outlet, although solar receivers are generally sized according to the design point mass flow rate and thus this does not have an influence on the decision to discard Design Case A. It is envisioned, however, that utilising outlet 2 will make possible future modifications easier to implement.

Implementing the newly designed compressor stage was shown to increase the overall system performance in Section 5.3. The effects of implementing the new compressor, on the velocity and pressure profiles at outlet 2, are presented next. The effect of the new compressor on the flow profiles at outlet 1, as per Design Case A, is shown in Appendix H.2.

9.3 New Compressor Solutions

The effects of implementing the new compressor on the resultant flow at outlet 2, is compared to the original compressor's flow predictions. The new compressor stage changed the inlet boundary conditions of the simulation, as discussed in Section 8.2.2. A comparison of the velocity streamlines is shown in Figure 45.

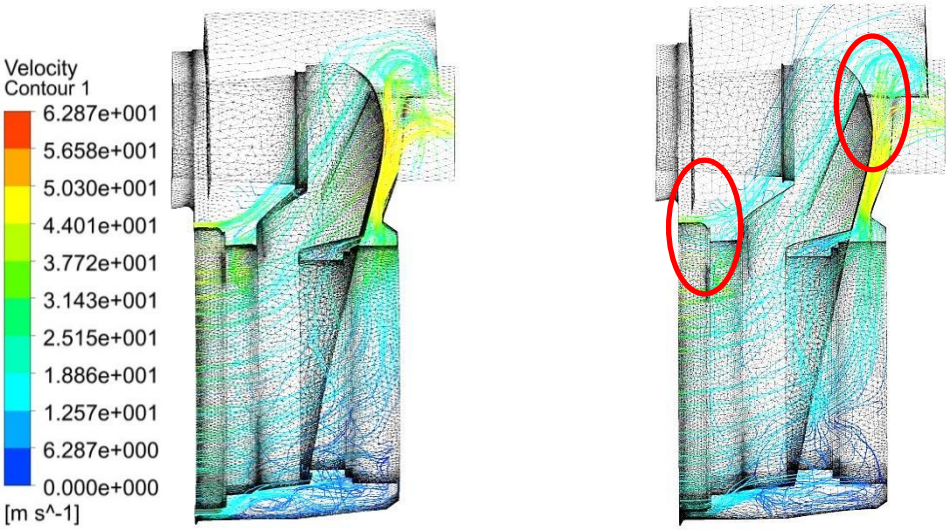

Figure 45: Original compressor (a) and new compressor (b) velocity streamline comparison

The solution in Figure 45 (a) is identical to that displayed in Figure 43 (a) and is repeated to emphasize the effects when implementing the new compressor. The new compressor improved the pressure ratio over the compressor. An increased inlet pressure slightly decreases the flow velocity, as shown in Figure 45 (b). This is mainly due to the new diffuser, which is designed for pressure recovery, by decreasing flow velocity and is confirmed by the velocity contours in Figure 46.

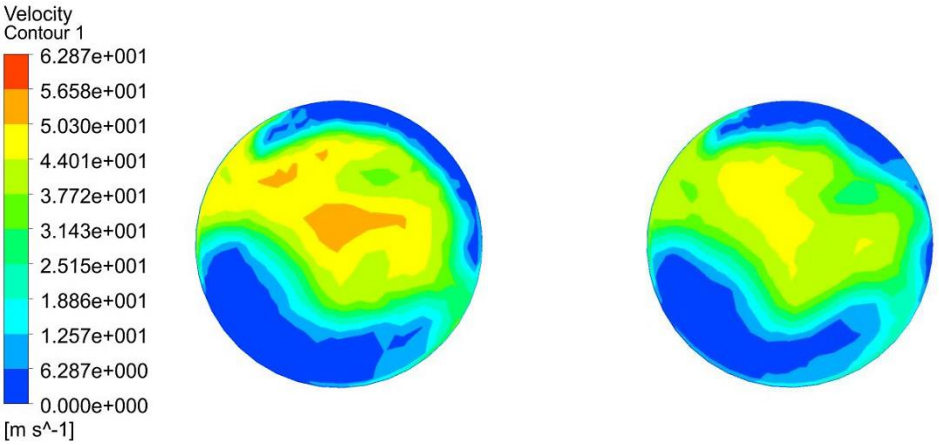

Figure 46: Original compressor (a) and new compressor (b) velocity contour comparison

The velocity contour, as a result of implementing the new compressor, clearly shows a decrease in the flow velocity magnitude. However, the outlet velocity profile (or shape) in Figure 46 (b), is very similar to the case when the original compressor is used, shown in Figure 46 (a). The pressure profiles also seem similar, as shown in Figure 47.

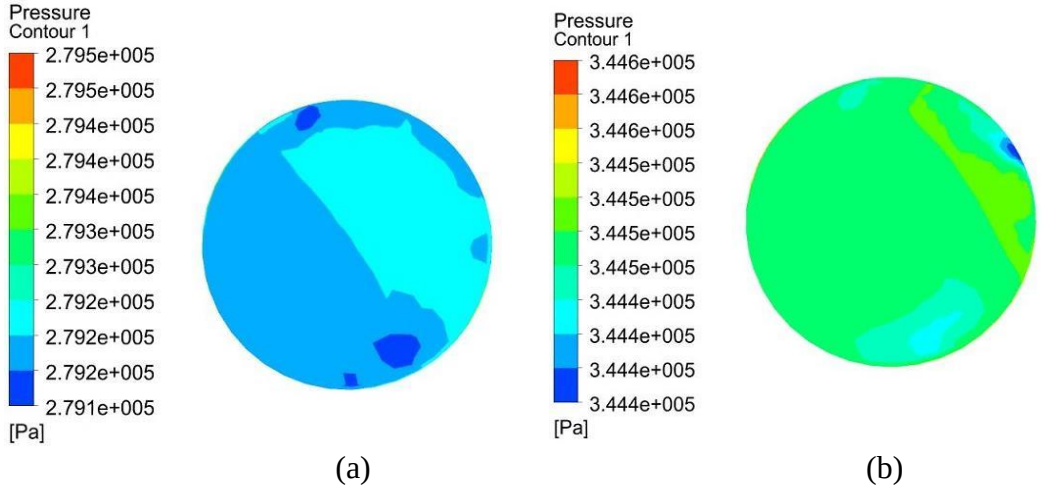

Figure 47: Comparison of the pressure contours between the old compressor (a) and the new compressor (b)

The pressure profiles do, however, differ vastly in magnitude. The legend's scale of both pressure contours were again set to local scale, as a matching scale for Figure 47 (a) and (b) would lead to a single coloured contour. This is erroneous, even though the pressure values do not vary much on the outlet face. A 23.22 % increase in pressure on the outlet face was predicted and it is expected to compensate for the additional pressure loss incurred in the solar components.

10 Solar Hybridization Modification Concepts

It was established that Design Case B would provide uniform pressure flow profiles, with larger flow velocity magnitudes predicted at the centre of the outlet. This significantly simplifies the GTR-Link design as it does not have to rectify the flow profile. A simple pipe elbow connected to outlet 2 will suffice. However, reintroducing the air into the combustor upon return from the solar receiver, poses some challenges.

The combustor is an important component in gas turbines, as it ensures that the maximum turbine inlet temperature is not exceeded, while supplying a uniform temperature flow profile to the turbine. The maximum turbine inlet temperature is dependent on the turbine material properties and cannot be exceeded, as this will cause degradation in the turbine blades. Furthermore, a uniform temperature pattern at the combustor outlet is required, to reduce the turbine's exposure to concentrated thermal stress, which could also lead to degradation.

To effectively reintroduce the air into the combustion chamber, two concepts were explored. The first concept entails the extension of the flame tube and adaption of the combustion chamber, similar to that of the recuperated Rover gas turbine. A second concept was investigated, replacing the combustion chamber with an inline firing duct. The two concepts are detailed below.

10.1 Combustor Extension

The first concept proposes an extension of the flame tube. A pipe elbow, combined with the extended flame tube through it, is shown in Figure 48.

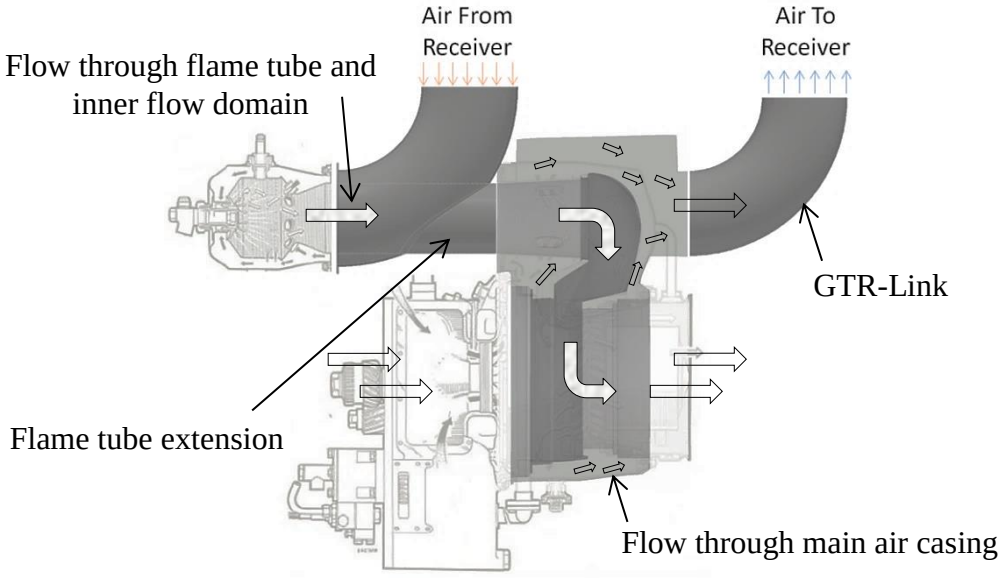

Figure 48: Combustor extension

Fisher *et al.* (2004) recognised that a major issue of solar hybridization of gas turbine engines was the adaptation of the combustion chamber, to accommodate a large range of fuel-air-ratios (FAR). The flame tube in the Rover gas turbine regulates the turbine inlet temperature and the temperature pattern, but was designed for design point conditions only, as opposed to a wide range of operating conditions.

Sjoblom (1980) investigated the effects of various design parameters, including the flame tube length, on the cooling air requirements in a gas turbine combustion chamber. Although his emphasis was on the cooling air requirement, the amount of cooling air in the flame tube directly impacts the turbine inlet temperature and temperature pattern. The result of the effect of flame tube length on the percentage of cooling air required, at a constant flame tube diameter, is shown in Figure 49.

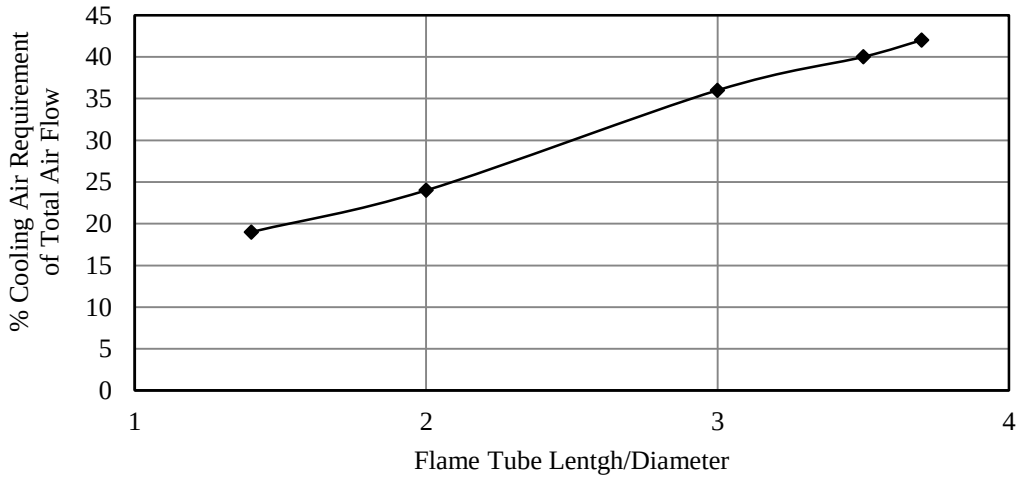

Figure 49: Effect of flame tube length on the % cooling air required (Sjoblom, 1980)

Sjoblom (1980) found that an increased flame tube length increases the percentage of cooling air required, but with adverse pressure effects. It was also established that a reduced length, impaired combustion efficiency and dilution zone performance. Even though his study focussed primarily on combustors with film cooling, he concluded that his findings were also valid for other types of combustors.

To provide sufficient combustion, flame stabilization and mixing with cooler dilution air, typical combustor length-to-diameter ratios range from three to six (Boyce, 2012). To stay within the recommended range, the flame tube length can be increased by a maximum of 474 mm. The original flame tube diameter and length is 117 mm and 228 mm respectively.

Gupta (2000) examined the flame characteristics of high temperature air combustion and described some of the challenges encountered with high temperature air combustion technologies. He found that, due to the decreased density of air, there were less diffusion of fuel into the air and this resulted in an increased flame length. Applying Gupta's findings, the high temperature air from the solar receiver would result in an increased flame length, which is then potentially compensated for by the extension of the flame tube in the proposed modification.

The concept is similar to modifications made to the experimental setup that incorporated the recuperator into the Rover gas turbine. The dilution holes were also sealed when installing the recuperator, possibly to prevent air from flowing predominantly through the dilution holes. If the pressure drop through the recuperator is too large during the start-up procedure, more air will flow through the dilution holes than the recuperator. Consequently, less air will be present in the combustion chamber and a rich fuel-to-air ratio will exist. Due to the large amount of air entering the flame tube, however, it is possible that the flame is extinguished, otherwise known as a flameout.

Sealing the dilution holes also prevents the cooling of combusted air before the turbine inlet. Since no other cooling air was introduced in the recuperated Rover gas turbine setup, it is possible that the cracks found on the turbine blades were caused by continuously exceeding the maximum turbine inlet temperature.

Although theoretically examined, no definitive conclusion can be made regarding the effects of extending the flame tube and it is suggested that the flame tube (including extension) is experimentally tested to verify flame stability and shape. The effect of sealing the dilution holes should also be investigated further.

10.2 In-line Combustor

The second concept simplifies the proposed experiment by completely removing the combustion chamber. Additional heat is added, after the solar receiver, inside the pipe leading to the gas turbine, by means of an In-line Firing Burner (IFB), depicted in Figure 50.

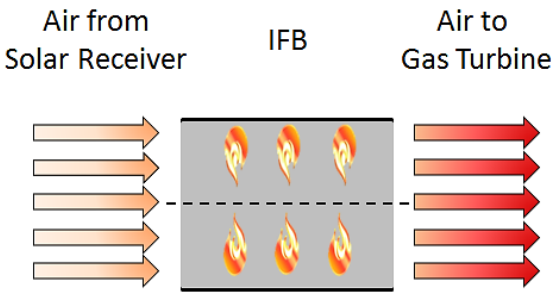

Figure 50: In-line combustor concept

IFB's have the advantage that ambient air is used for the combustion process, thus the amount of heat added through the solar receiver does not affect combustion. A control algorithm determines the burner intensity required to achieve maximum turbine inlet temperature, by monitoring the temperature at the inlet and outlet of the IFB and adjusting the intensity accordingly. The intensity can be varied by installing rows of burners with a variable firing capacity range, or rows of different fixed-capacity burners in a geometric sequence. The sequence will size the capacity of the fixed-capacity burners by:

$$f_n = f_{n-1}\, r_b \tag{10.1}$$

where r_b is the ratio of the sequence and n is the burner number. Selecting a sequence ratio of two, the burner capacities will be 1, 2, 4, 8, 16 etc., in relation to the first burner's capacity. For example, if the first burner capacity is 5 kW, the second burner will have a capacity of 10 kW, the third a capacity of 20 kW, etc. This enables the control algorithm to fire the burners in any sequence necessary to achieve the required turbine inlet temperature.

There are numerous firing burners installed and proven in industry and several companies specialise in the design and installation of In-line Firing Burners. Two prospective burners from Eclipse (2014) are shown in Figure 51.

(a) (b)

Figure 51: Tube Firing Burner (a) and ThermAir Burner (b) products from Eclipse (2014)

The Tube Firing Burner can be installed with a recuperator to maximize its efficiency, as shown in Figure 51 (a). The nozzle is designed for an adjustable flame length and the flame tube ensures an even heat distribution up to a maximum process temperature of 1040 °C. The Tube Firing Burner works similar to an electric element, heating air flowing over the tube by means of convection. The ThermAir Burner, shown in Figure 51 (b), is a direct fired burner capable of a maximum process temperature of 1038 °C. Specifying the capacity and number of burners needed to obtain the correct turbine inlet air temperature, requires an in-depth investigation of the air flow profiles and properties, primarily dependent on the solar receiver, which is beyond the scope of the current work.

10.3 Concept Evaluation and Proposed Modification

An evaluation of the two concepts, by means of a decision matrix, is given in Table 14 below. The concepts were rated on a scale of 1 to 5 (1 = Poor and 5 = Very Good) at various criteria, with an emphasis on experimental practicality. Weightings were applied to each criterion, as seen fit.

Table 14: Numerical evaluation of experimental concepts

Criteria	Criteria Weighting	Effect of Flame Tube Length	In-line Combustor
Low Design time	0.05	4	3
Ease of implementation	0.25	2	4
Low Maintenance	0.15	2	4
Testability	0.5	4	5
Applicability to other gas turbines	0.05	1	4
Total		3.05	4.55

The decision matrix results indicate that the In-Line Combustor concept should be implemented and tested within an experimental environment. Although it might require more design time to source and specify the correct burners, the concept has many advantages over the concept requiring an extended flame tube. The largest advantage lies in the simplification of the combustion process. The proposed modification is shown in Figure 52 and discussed thereafter.

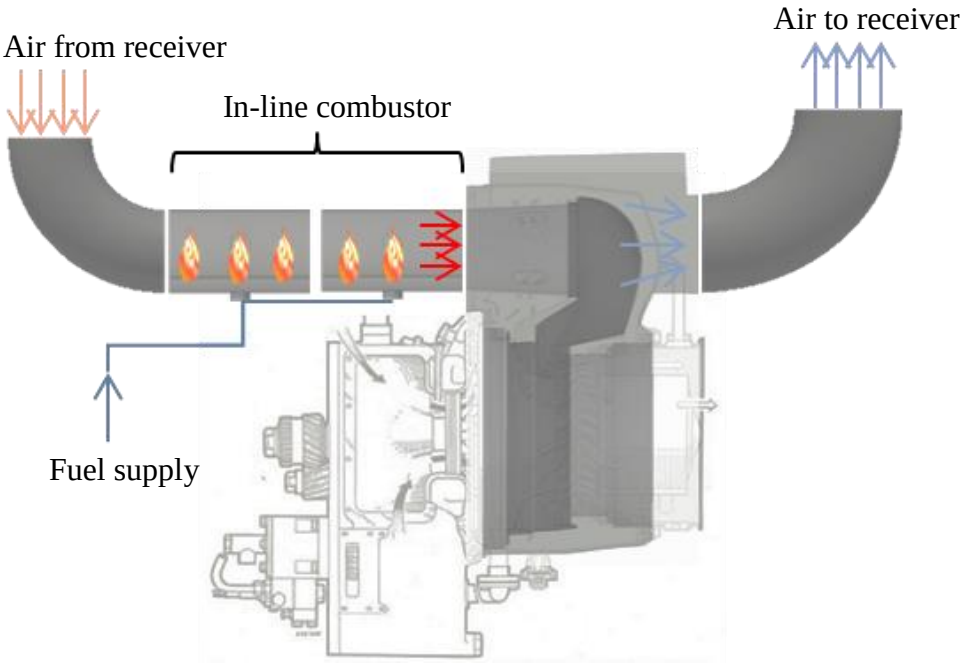

Figure 52: Proposed solar hybridization modification (Adapted from Rover, 1966)

The current combustor is removed completely and replaced by a fitting made to close outlet 1. The concept replaces the original flame tube with a standard pipe, negating the requirement to seal the dilution holes. An elbow redirects air from the solar receiver into the in-line firing section, where the air is heated to the maximum turbine inlet temperature.

The main purpose of a combustor is to rapidly heat the air before it expands in the turbine. This is achieved by mixing air and fuel, and igniting the mixture in the combustion chamber to release thermal energy. When enough heat is added by the burners, the gas turbine should be able to operate at its design point.

If the concept is found feasible within an experimental setup, gas turbines designed with external combustion chambers could be modified for solar hybridization with minimal effort. Gas turbines with a larger power production capacity requires more heat input from combustion, and to determine whether this is feasible on a commercial scale, a scalability analysis was conducted.

11 Scalability Analysis

This chapter presents the findings on the feasibility of solar hybrid gas turbines implemented at a commercial level. The approach approximated the thermal energy input required by industrial sized gas turbines and determined the size of the solar field that will be able to supply all of the thermal energy, given the meteorological and solar field data of Helio100. The aperture area of the solar fields, along with the predicted power output of the plant, is then compared to commercial CSP plants. The aperture area was chosen as the comparative measure because it contributes to a significant share, estimated at 33 % for the heliostat support structures and mirrors only, of the total investment cost (IRENA, 2013).

The Rover gas turbine requires approximately 417 kW_{th} (from Equation 3.9) in order to achieve the maximum turbine inlet temperature and deliver 45 kW net power. Given the solar resource at Helio100, on a day when maximum solar field efficiency and solar receiver efficiency is obtained, about 45 % of the required thermal energy input can be supplied. Solar field and receiver efficiencies resulting in 74.55 % and 88.21 % were determined respectively, at a measured DNI value of 1050.42 kW/m^2, as explained in Section 4.5.

Four other commercial gas turbines were investigated. They were chosen within the power range limitations of current commercial single tower CSP plants, which range between 1 MW and 110 MW. Details of the gas turbines selected for the analysis are given in Table 15.

Table 15: Commercial gas turbines' specifications

	Mercury 50	**Mars 100**	**Siemens SGT - 700**	**Siemens SGT6 – 2000E**
P_e [MW]	4.6	11.35	31.21	112
Heat Rate [kJ/kW_e-hr]	9350	10935	9882	10619
Heat Input Required [MW]	11.95	34.48	85.67	330.37
Recuperated?	Yes	No	No	No
Exhaust Gas Temperature	374	484	541	540

Data sheets of all the above mentioned gas turbines can be viewed in Appendix I. The thermal energy input required, $\dot{Q}_{th}$, was approximated as:

$$\dot{Q}_{th} = P_e \, \dot{Q}_{combustor} \tag{11.1}$$

where P_e denotes the output power and $\dot{Q}_{combustor}$ is the heat rate supplied by the combustion chamber. To determine the aperture area required to operate the gas turbines at 100 % solar share, Equation 4.5 was rewritten as follows:

$$A_{Aperture} = \frac{\dot{Q}_{th}}{DNI\ \eta_{solar-field}\ \eta_{receiver}} \quad 11.2$$

where the solar thermal power is now replaced by the thermal energy supplied by the combustor. The size of the solar field, relative to the solar field size required to reach the rated power output at design point, is called the solar multiple. The solar multiple is typically chosen between 1.3 and 1.4 to ensure that the power block is used effectively (IRENA, 2012). All areas calculated by Equation 11.2 were thus multiplied by a solar multiple range average value of 1.35.

Next, the aperture area and power output from commercial central receiver tower CSP plants were investigated. For a reasonable comparison, single tower CSP plants were limited to the USA, more specifically to the western states such as Nevada and California. The specifications of the CSP plants relevant to the current study are shown in Table 16.

Table 16: CSP Plant specifications

	Sierra SunTower (NREL, 2014b)	**Coalinga (CSP World Map, 2015)**	**Crescent Dunes Solar Energy Project (NREL, 2014a)**
P [MW]	5	29	110
Aperture Area [m^2]	27670	194000	1071361
Average annual DNI [kwh/m^2]	2629	2550	2685

The specifications listed in Table 16 indicate that an increase in the power output of a plant demands an increase in aperture area. It is assumed that a solar multiple was already allocated during plant design and optimization. Figure 53 compares power outputs against aperture areas of gas turbines and CSP tower plants. Both axes in Figure 53 were scaled logarithmically, due to the large range of plant sizes evaluated.

To supply 100 % of the thermal energy required by the Rover gas turbine an aperture area of 815 m^2 is required, approximately three times the current available aperture area at Helio100. Figure 53 indicates an approximate linear relationship between the logarithmic rated power and logarithmic aperture area of both commercial CSP tower and suggested SHGT power plants. The approximated gas turbine solar field sizes compare well to those currently used in industry when 100 % of the heat from combustion is replaced by solar irradiation. However, at large power outputs, Figure 53 shows that SHGTs might require smaller aperture areas, when compared to large CSP tower plants.

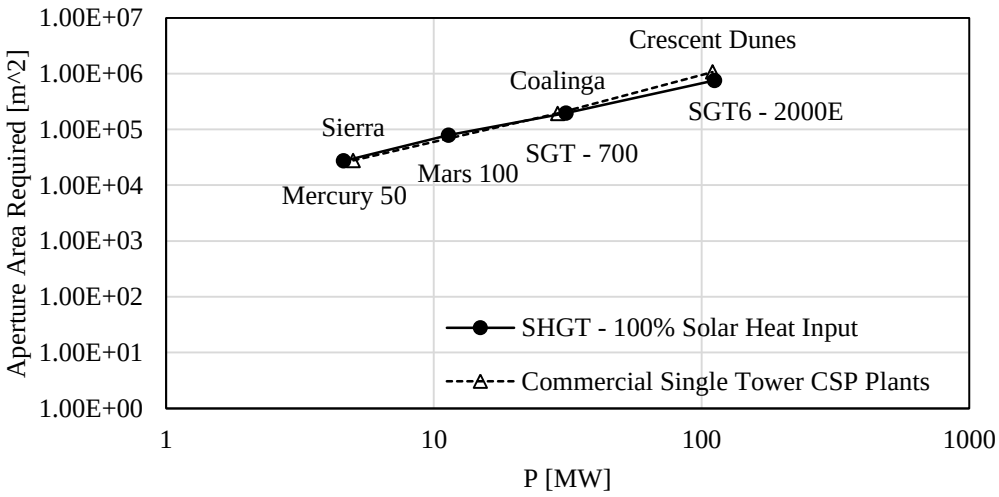

Figure 53: Comparison of potential SHGTs and CSP plant aperture areas

As discussed in Section 4.4, the availability of solar resource varies depending on the location of a plant. The size of the solar field therefore, inherently depends on the resource availability as well. Although the solar annual average DNI of each location varies, as seen in Table 16, CSP plants are typically designed for DNI values of 800 W/m^2 to 1000 W/m^2. An average DNI design value of 900 W/m^2 was used to estimate the aperture area of the SHGT power plants.

The aperture-area-to-power comparison of the SHGT power plants omits the possibility of utilising combined cycles. The net power produced by the plant will increase when implementing a secondary Rankine cycle, as proposed by SUNSPOT. Consequently, the new aperture-area-to-power ratio will favour the SGHT plants when compared to commercial CSP tower power plants.

However, the Achilles heel of the SHGT concept remains the pressurised air solar receiver. Air, being less dense than water and molten salt used in commercial CSP plants, has to be pressurised for sufficient heat transfer to occur. Currently, most of the pressurised air receivers make use of a quartz glass window because it is the only glass with properties that permits sufficiently high transmittance and temperatures, with a low thermal expansion (Hofmann *et al.*, 2009). A review on pressurised air receivers by Lubkoll *et al.* (2014) also reported that receiver dimensions have been limited by the use of quartz glass windows. A breakthrough in pressurised air receiver technologies, like the SCRAP receiver, if proven feasible, is required for SHGT's to become commercially feasible.

12 Conclusions and Future Work

The effect of solar-hybridization of a gas turbine, on its performance and its integration into a solar power plant, was investigated. The integration of the Rover gas turbine within Stellenbosch University's testing facility, Helio100, was considered. The main findings and suggested future work are presented in this chapter.

12.1 Conclusions

The effects of solar hybridization on the performance of a gas turbine, were investigated by creating a system simulation in Flownex (2014a). Firstly, the existing Rover 1S/60 gas turbine was modelled and validated by a one dimensional thermodynamic model. The model determined a net power output of 42.41 kW and thermal efficiency of 10.59 %.

The model was adapted to a solar hybrid Rover gas turbine, based on the SUNSPOT configuration. A solar receiver and piping up and down the solar tower were incorporated to create a SHGT model. It was established that the pressurised air solar receiver plays an integral role in the performance prediction of a SHGT and a solar receiver was modelled based on published data of the SOLGATE receiver. At zero input solar irradiation, adverse pressure effects were realised due to the inclusion of solar components in the SHGT model. An additional pressure loss of 19.34 kPa reduced the net power output of the solar hybrid Rover gas turbine by 23.6 %. It was concluded that a by-pass valve should be included to circumvent the solar components at night times or during days with overcast weather conditions.

The additional pressure drop could also be eradicated by implementing a newly designed compressor. The compressor performance maps, for a newly designed compressor by Luiten (2015), were created in CENCOM and implemented into Flownex. Both the existing Rover gas turbine and solar hybrid Rover gas turbine models were re-evaluated, implementing the newly designed compressor. Significant performance improvements were predicted in both models, increasing the net power output by 49.6 % and 54.6 % respectively.

The performance of the solarized Rover gas turbine integrated within the Helio100 solar field was predicted. Using the solar field meteorological data and heliostat specifications, the maximum thermal energy transferred to the air via the solar receiver was determined as 184 kW_{th}. The solar heat input into the receiver pipe element in Flownex was thus varied from 0 to 200 kW and the effects on the performance of the gas turbine evaluated.

Heat addition due to solar irradiation resulted in a decreased fuel consumption rate and an increased thermal efficiency for the gas turbine. The influence of the additional pressure drop over the solar receiver is evident as it leads to decreased net power output.

Similar results were found when the new compressor was implemented, but due to the higher pressure ratio, the performance of the gas turbine is improved. At 200 kW solar thermal heat input, the SHGT model predicted 42.65 kW power output and a thermal efficiency of 27.41 %, which is a significant improvement when compared to the original Rover gas turbine's performance.

After proving the feasibility of the SHGT concept within a system setup, the integration of the Rover gas turbine into a CSP system was explored in more detail. Concepts to extract and re-introduce the air from and to the Rover gas turbine were investigated.

The main air casing was reverse-engineered and the inner flow domain was created, in order to generate a model that could predict the interconnection component's inlet conditions. Experimental test results of the Rover 1S/60 gas turbine were used to validate the computational flow model. The mass flow rate and post-compressor temperature were under predicted by 7.69 % and 11.74 % while the post compressor- and combustor delivery pressure were over predicted by 10.20 % and 12.37 % respectively.

Two possible outlets were investigated and it was determined that outlet 2 was the superior option for extracting the flow from the casing. The air flow predicted at this outlet indicated that a uniform pressure profile could be expected and high air velocities, that are relatively concentric around the centre of the outlet, were deemed acceptable for the intended application.

The model was revised by implementing the newly designed compressor's performance at the inlet boundary conditions. Due to the increased pressure ratio, the velocity of the air in the casing was decreased. This was attributed to the newly designed diffuser which was designed for pressure recovery after compression. Implementing the new compressor resulted in an average pressure increase of 23.22 % on the outlet face, considered sufficient to overcome the additional pressure drop over the solar components.

Reintroducing the air into the current combustion chamber has many unknowns and therefore requires extensive analysis. A simplified concept was suggested for experimental application. The concept utilizes in-line firing burners in the ducting that returns the air to the gas turbine from the solar receiver.

Finally, the feasibility of implementing a solar hybrid gas turbine on a commercial level was investigated. The aperture areas required to replace thermal heat input from combustion of several gas turbines, ranging from 4.6 MW to 112 MW, were determined. The resultant aperture areas were found to compare well to current commercial CSP tower plants, omitting the additional power that a secondary Rankine cycle would provide to the SHGT plant. The scalability analysis showed that there is potential in commercializing solar hybrid gas turbines, but that advances in the technology of pressurised air receivers are crucial to their success.

12.2 Future Work

The SHGT concept has shown great potential and the following work packages are suggested in order to advance the research to an experimental stage.

The technical feasibility with regard to accurate fuel flow control, as solar irradiation varies, is recommended for further investigation. Experimental tests should also be performed to determine the lean and rich FAR's of the Rover gas turbine, as the lean limit is necessary to establish the minimum required solar heat input to operate the gas turbine on solar irradiation only.

The proposed combustion replacement system should be proved theoretically, before proving it in an independent experimental setup. It should also be tested at conditions that simulate the new compressor. Once the feasibility of the combustor is proven on an experimental level, it should be integrated with the Rover gas turbine and the performance re-evaluated.

Great potential performance improvements were realised when implementing the new compressor in the system simulation. The new compressor should be manufactured and implemented into the current Rover gas turbine experimental setup. After critically evaluating the effects of the newly designed compressor on the performance of the gas turbine, it can be determined whether to proceed with further modifications that solarize the gas turbine.

It is envisioned that the SCRAP receiver, currently under development at Stellenbosch University, provides the means necessary to integrate the Rover gas turbine into a CSP system while incurring minimal additional pressure losses. To demonstrate the feasibility of SHGT's, the solar hybrid Rover gas turbine is to be implemented into the Helio100 testing facility, in order to experimentally evaluate the effects of solar hybridization on the performance of the Rover gas turbine.

13 Bibliography

Allen, K. G. (2010) 'Performance characteristics of packed bed thermal energy storage for solar thermal power plants', University of Stellenbosch.

ANSYS Inc (2015) 'Introduction to ANSYS Fluent', Stellenbosch, ANSYS Intoductory workshop presented by Qfinsoft.

ANSYS Inc (2013a) 'User Manual: ANSYS Fluent - Turbulence',.

ANSYS Inc (2013b) 'Workbench V14.5.7', [online] Available from: http://www.ansys.com/Products/Workflow+Technology/ANSYS+Workbench+Platform.

AUTODESK (2016) 'Inventor Professional', [online] Available from: http://www.autodesk.com/products/inventor/features/all/gallery-view.

Barigozzi, G., Bonetti, G., Franchini, G., Perdichizzi, A. and Ravelli, S. (2012) 'Thermal performance prediction of a solar hybrid gas turbine', *Solar Energy*, 86(7), pp. 2116–2127.

Beér, J. M. (2007) 'High efficiency electric power generation: The environmental role', *Progress in Energy and Combustion Science*, 33(2), pp. 107–134.

Bell, S. (2011) *Measurement Good Practice Guide*, Teddington, Middlesex, United Kingdom, National Physics Laboratory.

Bheemaraddi, S. B. and Kumarappa, D. S. (2014) 'Assessment of Turbulent Boundary Layer Modeling Methods by Using Computational Fluid Dynamics for Gas Turbine Engine Afterburner Diffuser', *International Journal of Innovative Research in Science, Engineering and Technology*, 3(1), pp. 8765–8772.

Boyce, M. P. (2012) *Gas Turbine Engineering Handbook*, 4th ed. Elsevier Inc.

BS 848 (1997) *Fans for general purposes - Part 1: Performance testing using standarized airways*, British Standards Institution.

Camp, T. R. and Shin, H.-W. (1994) 'Turbulence Intensity and Length Scale Measurements in Multistage Compressors', In *ASME 1994 International Gas Turbine and Aeroengine Congress and Exposition*, The Hague, Netherlands.

Cengel, Y. A. and Cimbala, J. M. (2010) *Fluid Mechanics Fundamentals and Applications*, 2nd ed. New York, McGraw-Hill.

Chen, L., Wang, W., Sun, F. and Wu, C. (2004) 'Closed intercooled regenerator Brayton-cycle with constant-temperature heat-reservoirs', *Applied Energy*, 77(4), pp. 429–446.

Chu, H. (2006) 'Flame Temperature', In National Cheng Kung University, [online] Available from: myweb.ncku.edu.tw/~chuhsin/ppt/.../04-Flame Temperature.ppt.

Chu, Y. (2011) 'Review and Comparison of Different Solar Energy Technologies', San Diego, California, Global Energy Network Institute.

Cohen, H., Rogers, G. and Saravanamuttoo, H. (2001) *Gas Turbine Theory*, 5th ed. Essex, England, Pearson Education Limited.

CSP Today (2013) *Concentrated Solar Power Markets Report 2012-2013*, London, FC Business Intelligence Ltd.

CSP World Map (2015) 'Coalinga', [online] Available from: http://www.cspworld.org/cspworldmap/coalinga (Accessed 12 August 2015).

DeCoursey, W. J. (2003) *Statistics and Probability for Engineering Applications*, 1st ed. Saskatoon, Canada, Elsevier Science.

Delcam (2014) 'PowerSHAPE', [online] Available from: http://www.delcam.com/software/powershape/.

Duffie, J. A. and Beckman, W. A. (1991) *Solar Engineering of Thermal Processes*, 2nd ed. New York, John Wiley and Sons.

Eclipse (2014) 'Eclipse Products', [online] Available from: http://www.eclipsenet.com/ (Accessed 11 August 2015).

EPIA and Greenpeace (2011) *Solar Generation: Solar Photovoltaic Electricity Empowering the World*, [online] Available from: http://www.greenpeace.org/international/Global/international/publications/climate/2011/Final SolarGeneration VI full report lr.pdf.

Fisher, U., Sugarmen, C., Ring, A. and Sinai, J. (2004) 'Gas Turbine "Solarization"-Modifications for Solar/Fuel Hybrid Operation', *Journal of Solar Energy Engineering*, 126(3), p. 872.

Flownex (2014a) *Flownex Library Manual*, [online] Available from: www.flownex.com/info@flownex.com.

Flownex (2014b) 'Flownex Simulation Environment', [online] Available from: http://www.flownex.com/.

Gauché, P., von Backström, T. W. and Brent, A. C. (2011) 'CSP Modeling Methodology For Macro Decision Making - Emphasis On The Central Receiver Type', In *SolarPACES*, Granada, Spain.

Gauché, P., Brent, A. C. and von Backström, T. W. (2014) 'Concentrating solar power: Improving electricity cost and security of supply, and other economic benefits', *Development Southern Africa*, (July), pp. 1–19.

GeoModel Solar (2014) 'SolarGIS iMaps online access to high resolution solar data', [online] Available from: http://solargis.info/doc/_pics/freemaps/1000px/dni/SolarGIS-Solar-map-DNI-South-Africa-en.png (Accessed 3 August 2015).

Grange, B., Dalet, C., Falcoz, Q., Siros, F. and Ferrière, A. (2014) 'Simulation of a Hybrid Solar Gas-turbine Cycle with Storage Integration', *Energy Procedia*, 49, pp. 1147–1156.

Grong, T. S. (2009) 'Modeling of Compressor Characterisics and Active Surge Control', Norwegian University of Science and Technology.

Gupta, A. (2000) 'Flame characteristics and challenges with high temperature air combustion', In *Proccedings of 2000 International Joint Power Generation Conference*, Miami Beach, Florida, ASME, pp. 1–18.

Heller, L. (2014) 'Solar Thermal Power Systems',.

Heller, L. and Gauché, P. (2014) 'Dual-pressure Air Receiver Cycle for Direct Storage Charging', *Energy Procedia*, 49, pp. 1400–1409.

Ho, C. K. and Iverson, B. D. (2014) 'Review of high-temperature central receiver designs for concentrating solar power', *Renewable and Sustainable Energy Reviews*, 29, pp. 835–846.

Hofmann, A., Schenk, C. and Uhlig, R. (2009) 'Optical Quartz Glass Windows for High Concentrated Thermal Power Plants', In *SolarPACES*, Berlin, Germany.

Hunt, R. J. (2011) *The History of the Industrial Gas Turbine (Part 1 The First Fifty Years 1940-1990)*, United Kingdom.

IRENA (2012) *Concentrating Solar Power, Renewable Energy Technologies: Cost Analysis Series: Concentrating Solar Power*, [online] Available from: http://www.irena.org/documentdownloads/publications/re_technologies_cost_analysis-csp.pdf.

IRENA (2013) *Concentrating Solar Power Technology Brief*, [online] Available from: https://www.irena.org/DocumentDownloads/Publications/IRENA-ETSAP Tech Brief E10 Concentrating Solar Power.pdf.

Jamel, M. S., Abd Rahman, A. and Shamsuddin, A. H. (2013) 'Advances in the integration of solar thermal energy with conventional and non-conventional power plants', *Renewable and Sustainable Energy Reviews*, 20, pp. 71–81.

Kipp & Zonen (2008) 'CHP1 Pyrheliometer: Instruction Manual', Delft, Netherlands.

Knies, G., Möller, U. and Straub, M. (2007) *Clean Power from Deserts EU-MENA Clean Power from Deserts*, 4th ed. Trans- Mediterranean Renewable Energy Cooperation, Hamburg.

Kolb, G. J., Ho, C. K., Mancini, T. R. and Gary, J. A. (2011) *Power Tower Technology Roadmap and Cost Reduction Plan*, Livermore, California.

Kröger, D. G. (2012) *SUNSPOT – The Stellenbosch University Solar Power Thermodynamic cycle*, Technical report, Department of Mechanical and Mechatronic Engineering, Stellenbosch University.

Le Roux, W. G., Bello-Ochende, T. and Meyer, J. P. (2014) 'The efficiency of an open-cavity tubular solar receiver for a small-scale solar thermal Brayton cycle', *Energy Conversion and Management*, 84, pp. 457–470.

Lefebvre, A. H. (1998) *Gas Turbine Combustion*, 2nd ed. Phiadelphia, United States of America, Edwards Brothers.

Lovegrove, K. and Stein, W. (2012) *Concentrating solar power technology*, 1st Editio. Cambridge, UK, Woodhead Publishing Limited.

Lubkoll, M., von Backström, T. W. and Kröger, D. G. (2014) 'Survey on Pressurized Air Receiver Development', In *Southern African Solar Energy Conference*, Port Elizabeth, South Africa.

Luiten, R. V. (2015) 'Performance Improvement of the Rover 1S/60 Gas Turbine Compressor', Stellenbosch University.

MathWave Technologies (2015) 'EasyFitXL', [online] Available from: http://www.mathwave.com/products/easyfit_desc.html.

Meyer, A. J. and Van Niekerk, J. L. (2011) 'Roadmap for the Deployment of Concentrating Solar Power in South Africa', In *SolarPACES*, Granada, Spain.

Mills, D. R. (2001) *Solar thermal electricity, The state of the Art ISES Position Papers*, 1st ed. J. Gordon (ed.), United Kingdom, Cromwell Press.

NREL (2014a) 'Concentrating Solar Power: Projects: Crescent Dunes Solar Energy Project', [online] Available from: http://www.nrel.gov/csp/solarpaces/project_detail.cfm/projectID=60 (Accessed 12 August 2015).

NREL (2014b) 'Concentrating Solar Power: Projects: Sierra SunTower', [online] Available from: http://www.nrel.gov/csp/solarpaces/project_detail.cfm/projectID=63?print (Accessed 12 August 2015).

Phakathi, S. A. (2009) 'Commisioning of a 1S/60 Rover gas turbine', University of Pretoria.

Prinsloo, L. (2008) 'The Commissioning of the Rover 1S / 60 Gas Turbine', University of Pretoria.

Quarta, N. J. (2012) 'Simulation of a Hybridised Solar Gas Turbine System', University of the Witwatersrand.

Rao, A. D. (2012) *Combined Cycle Systems for Near-Zero Emission Power Generation*, 1st ed. Sawston, Cambridge, Woodhead Publishing Limited.

REOTEMP Instruments (2011) 'Thermocouple Info', [online] Available from: http://www.thermocoupleinfo.com/ (Accessed 2 June 2015).

Rover (1966) *Rover Gas Turbines: Engine Type 1S/60 and 1S/90 Maintenance Manual*, Coventry, England.

Schwarzbözl, P., Buck, R., Sugarmen, C., Ring, A., Marcos Crespo, M. J., Altwegg, P. and Enrile, J. (2006) 'Solar gas turbine systems: Design, cost and perspectives', *Solar Energy*, 80(10), pp. 1231–1240.

Shah, S., Jain, S. and Lakhera, V. (2010) 'CFD based flow analysis of centrifugal pump', In *Proceedings of International Conferenceon Fluid Mechanics and Fluid Power*, Chennai, India.

Shaw, R., Lewkowicz, A. Z. and Gostelow, J. P. (1966) *Measurement of Turbulence in the Liverpool University Turbomachinery Wind Tunnels and Compressor*, London, England, Her Majesty's Stationery Office.

Shojaeefard, M. H., Tahani, M., Ehghaghi, M. B., Fallahian, M. a. and Beglari, M. (2012) 'Numerical study of the effects of some geometric characteristics of a centrifugal pump impeller that pumps a viscous fluid', *Computers and Fluids*, 60, pp. 61–70.

Siemens (2015) 'Siemens Gas Turbines: Gas turbines with a capacity from 4 to 400 MW', [online] Available from: http://www.energy.siemens.com/nl/en/fossil-power-generation/gas-turbines/ (Accessed 16 August 2015).

Sjoblom, B. G. A. (1980) 'Effects of Design Parameters on Cooling Air Requirement in a Gas Turbine Combustor', *Journal of Aircraft*, 17(5), pp. 292–293.

Da Soghe, R., Innocenti, L., Andreini, A. and Poncet, S. (2010) 'Numerical Benchmark Modelling in Gas Turbine Rotor-Stator System', In *ASME TURBO EXPO*, Glasgow, Scotland.

Solar Turbines Incorporated (2013) 'Gas Turbine Packages', [online] Available from: https://mysolar.cat.com/cda/layout?m=41100&x=7 (Accessed 16 August 2015).

SOLGATE Report (2005) *Solar hybrid gas turbine electric power system,*.

Spelling, J. D. (2013) 'Hybrid Solar Gas-Turbine Power Plants: A Thermoeconomic Analysis', KTH Royal Insitute of Technology.

Stine, W. and Geyer, M. (2001) 'Power From The Sun', [online] Available from: http://www.powerfromthesun.net/ (Accessed 18 July 2014).

Versteeg, H. K. and Malalasekera, W. (2007) *An Introduction to Computational Fluid Dynamics*, 2nd ed. Essex, Englad, Pearson Education Limited.

World DataBank (2013) 'World Development Indicatiors: Population Database', [online] Available from: http://databank.worldbank.org/data//reports.aspx?source=2&country=ZAF&series=&period= (Accessed 27 July 2015).

Appendix A: Intake System Results Comparison

Prinsloo (2008) designed, built and tested the intake system of the Rover gas turbine. Thereafter, Quarta created a Flownex model of the intake system, as discussed in Section 4.2.1. After determining the loss coefficient of the air filter in the intake system, the filter's loss coefficient within Flownex was corrected. The results obtained from the simulation correlates well to those of the experimental test results, as shown in Figure 54.

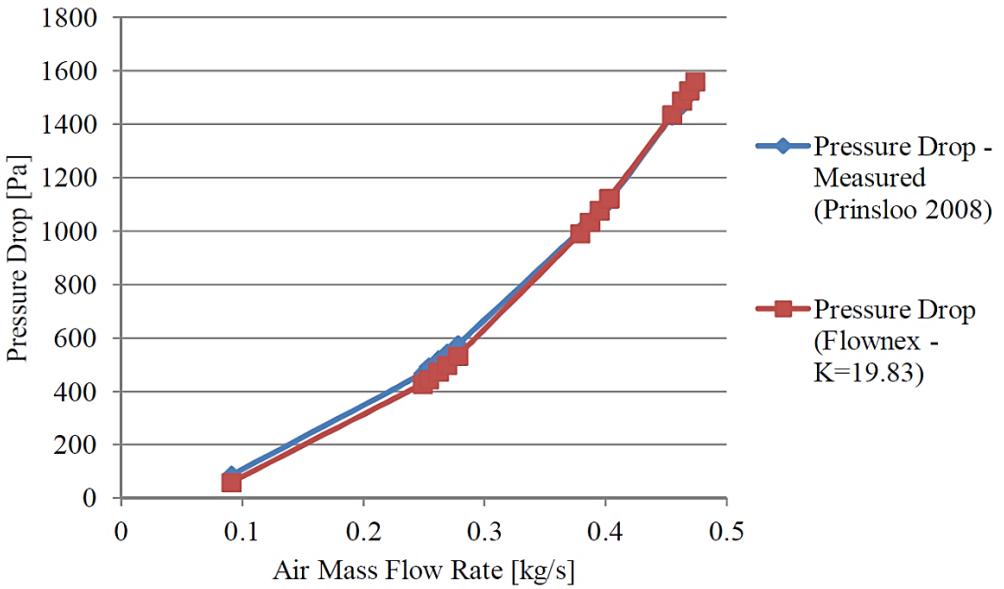

Figure 54: Comparison between the experimental and simulated results of the intake system (Quarta, 2012)

At the design mass flow rate, the difference between the simulated and experimental value was found to be less than 1 %. The intake system model was thus considered to be an accurate representation of the actual intake system and was used in subsequent models.

Appendix B: Diffuser Results Comparison

The new compressor stage, designed by Luiten (2015), was re-created in CompAero to obtain a compressor performance map as discussed in Section 4.2.2.3. Various programs within CompAero were used to create an accurate representation of the performance of newly designed compressor stage. The initial size estimation of the impeller and diffuser was done in SIZE, where after the diffuser geometry was exported to VDDESIGN for individual analysis. After further refinements in the geometry, more specifically the blade shape, of the diffuser, the following results were obtained in VDDESIGN and are compared to the results reported by Luiten (2015).

Table 17: Vaned diffuser design point parameters comparison

	Required value (Luiten, 2015)	Achieved value (VDDESIGN)
Flow inlet angle [°]	16.44	16.44
Blade inlet angle [°]	15.79	15.79
Incidence loss coefficient	0.023	0.025
Choke	0	0
Blockage loss coefficient	0.048	0.046
Static pressure coefficient	0.65	0.621
Total loss coefficient	0.23	0.247

As seen the results achieved compare well to those required. A maximum difference of approximately 7 % was found between parameters of the required and achieved diffuser performance. The diffuser was therefore considered to replicate the newly designed diffuser with reasonable accuracy after which the results from VDDESIGN were exported back into CENCOM. The performance map generated by CENCOM, at various corrected speeds, depicting the efficiency against the corrected mass flow, is shown in Figure 55.

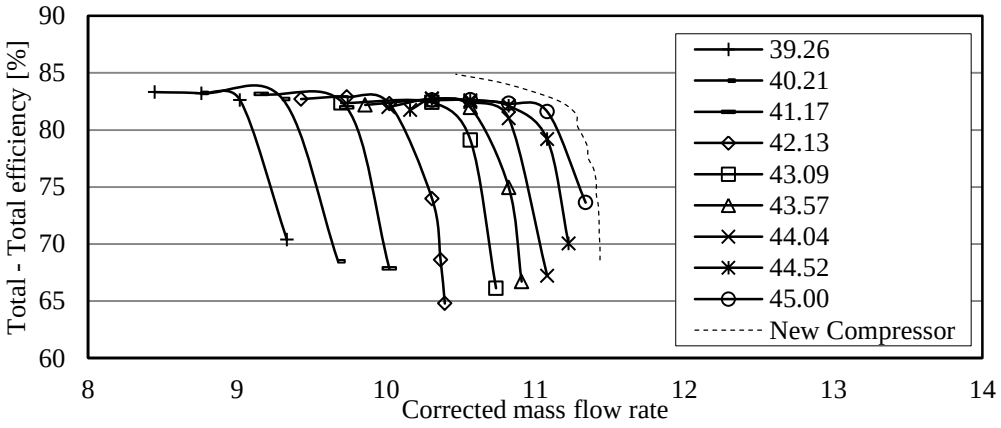

Figure 55: New compressor performance map

Appendix C: Zenith Angle Sample Calculation

To determine the zenith angle, used to calculate the optical efficiency of the heliostats (Equation 4.4), various solar angles were determined, including the declination angle, hour angle and solar altitude angle.

The declination angle is defined as the angle between lines drawn from the centre of the earth to the sun, and from the centre of the earth to its equatorial plane. The angle is calculated as follow:

$$\delta = 23.45 \sin\left(360 \frac{284 + n}{365}\right) \quad \text{C.1}$$

where n is the day number. The hour angle is used to describe the rotation of the earth about its polar axis, determined by:

$$\omega_{solar} = 15(t_{solar} - 12) \quad \text{C.2}$$

where t_{solar} is the solar time in hours. The solar and zenith angles are depicted in Figure 56, as seen from an observer, Q.

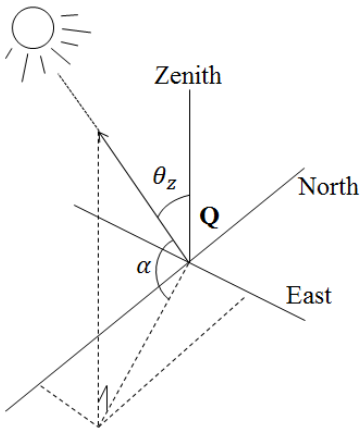

Figure 56: Coordinate system on Earth surface for an observer located at Q (Adapted from Stine and Geyer, 2001)

The solar altitude angle is calculated by:

$$\sin \propto = \sin\delta \sin\Phi + \cos\delta \cos\omega \cos\Phi \quad \text{C.3}$$

where Φ denotes the latitude. Finally the zenith angle can be found:

$$\theta_z = 90 - \propto \qquad \text{C.4}$$

Example calculation:

If the zenith angle is to be calculated at 14:00 on 8 May 2014, at the position of the heliostat field located at Mariendahl, the abovementioned equations would result in the following:

$\delta = 16.53°$; $\omega = 30°$; $\alpha = 32.08°$; $\theta_z = 57.92°$

Appendix D: Review of Pressurised Air Receivers

Literature on pressurised air receivers were reviewed to determine the specifications, more specifically, the pressure drop and efficiency of the receiver, of a simplified solar receiver model used in Flownex (Section 4.4.2). The development and progress of existing pressurised air receivers were reviewed by Lubkoll *et al.* (2014) and a qualitative comparison is shown in Table 18 below:

Table 18: Qualitative comparison of receiver technologies

(Adapted from Lubkoll *et al.*, 2014)

	DIAPR	REFOS	SOLGATE LT- receiver	SOLHYCO	SOLUGAS
Maximum temperature	+	+	-	0	0
Pressure drop	+	+	-	-	N/A
Thermal efficiency	+	+	0	-	0
Robustness, durability	N/A	-	-	-	N/A
Cost, simplicity	N/A	-	+	N/A	N/A
Flux density	+	0	-	-	-

As seen in Table 18, development regarding the robustness and durability of pressurised air receivers remain an obstacle. The pressurised air receiver is an important component contributing to the feasibility of solar hybrid gas turbines.

Appendix E: Probability Density Functions for Experimental Measurements

The P-P plots of the measured parameters in the recorded data set, indicating how well the proposed PDF's fit the measured data, are presented in this chapter. The old data set distribution fits are presented and discussed, where after the results of the new data set are presented. A summary of the measured parameter's selected PDF, range of values and probability of occurrence, is given in Table 10 in Section 7.5 and Table 19 at the end of the chapter, for both the old and new data set, respectively. The old data set's post compressor pressure and temperature, as well as the exhaust temperature, PP-plots are shown below in Figure 57, Figure 58 and Figure 59 respectively.

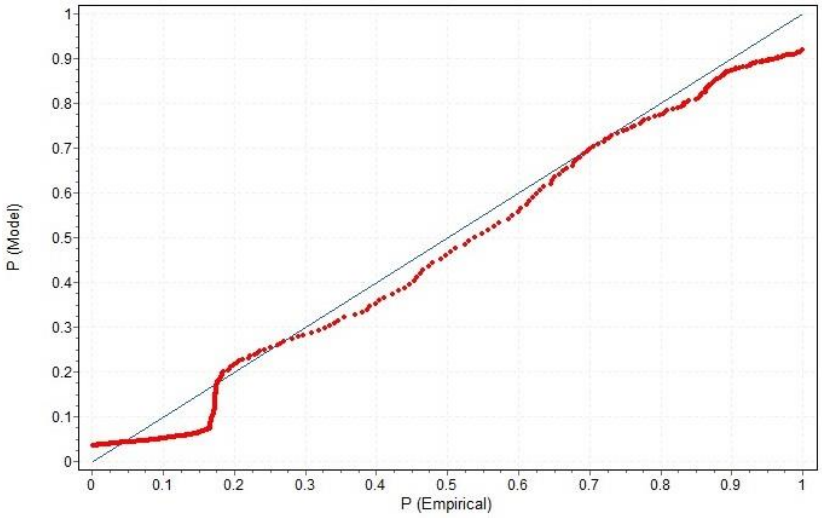

Figure 57: P-P plot of post-compressor pressure, old data set

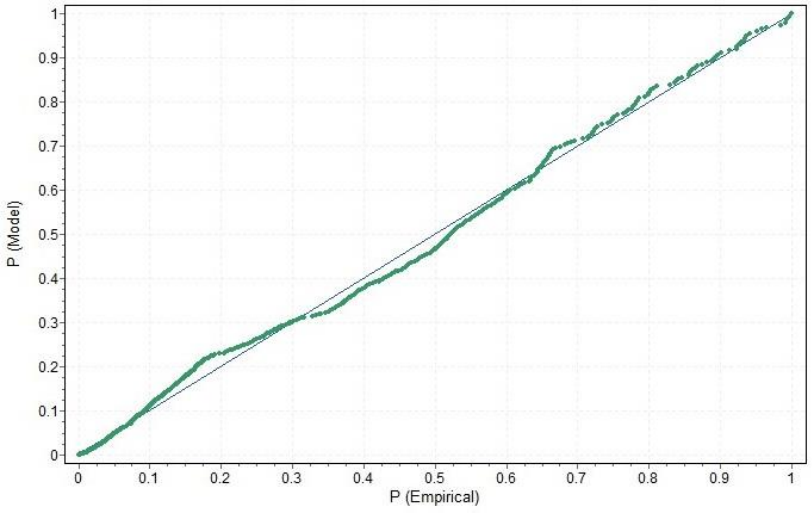

Figure 58: P-P plot of post-compressor temperature, old data set

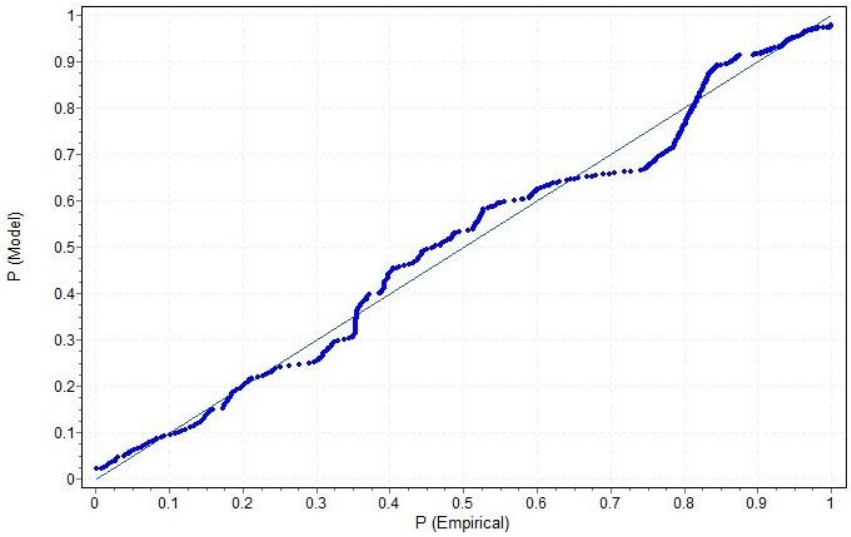

Figure 59: P-P plot of exhaust temperature, old data set

The PDFs represent the post compressor pressure and temperature adequately at high probabilities, but the exhaust temperature shows a greater deviation. This could be due to the scatter in the data of the exhaust gas temperature, or due to the fact that the temperature is actually an average between three measured values at the outlet of the gas turbine.

The new data set's combustor delivery pressure, post compressor temperature and exhaust temperature PP-plots are shown below in Figure 60, Figure 61 and Figure 62 respectively.

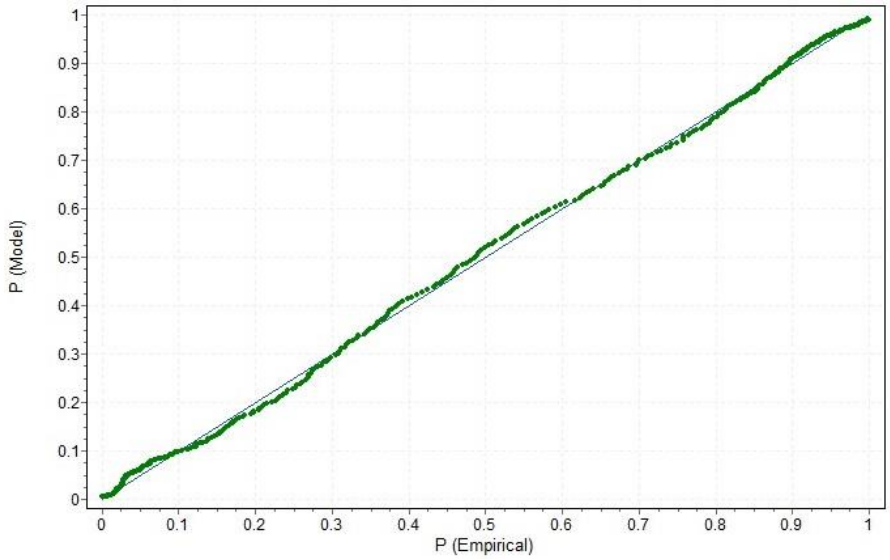

Figure 60: P-P plot of post-compressor pressure (combustor delivery pressure), new data set

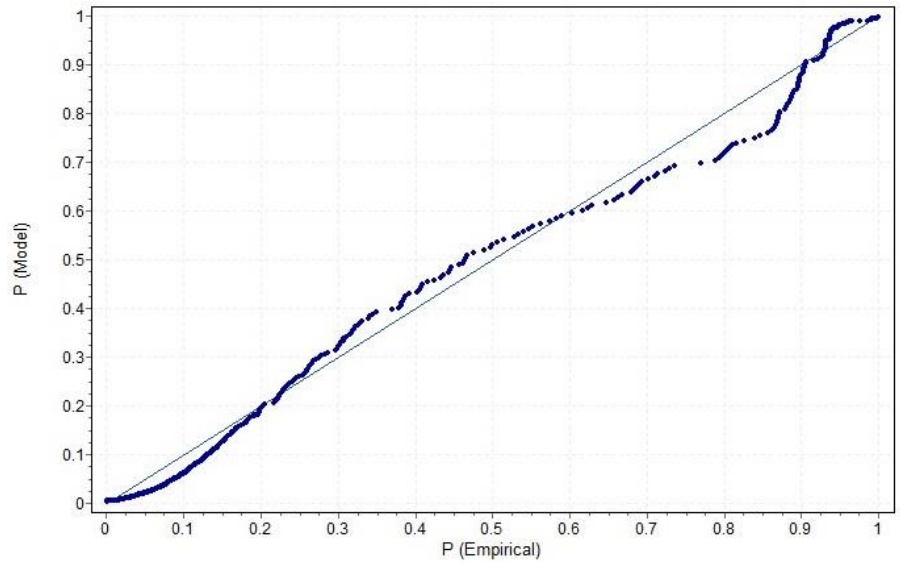

Figure 61: P-P plot of post-compressor temperature, new data set

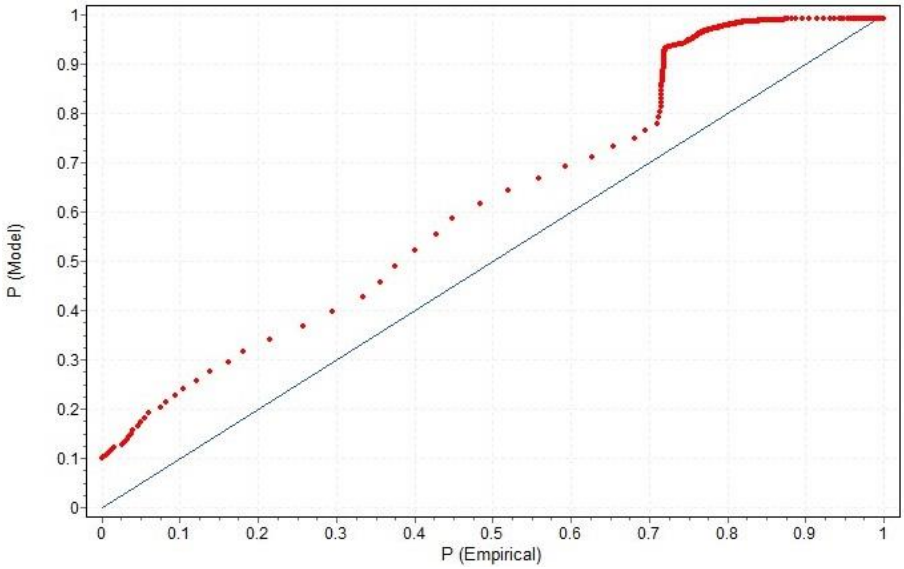

Figure 62: P-P plot of exhaust temperature, new data set

Again the PDFs represent the post compressor pressure and temperature relatively well at high probabilities. The exhaust temperature, however, is not accurately represented even by the best possible fit. It is suspected that, in order to obtain a PDF that represents the exhaust temperature accurately, a much larger data sample is required. The exhaust temperature was not used for CFD validation, as neither the old or new data set could be represented well enough by a PDF. The PDF of the old data set exhaust temperature were better represented and is given as an indication of what could be expected.

The value ranges of the new data set, within a 90 % confidence band, are presented in Table 19. Note that the exhaust gas temperature was omitted from Table 19, due to inaccurate representation by the PDF.

Table 19: Experimental testing results summary: After Overhaul

Measured Parameter	Probability Distribution	Value Range	Probability of Occurrence
ΔP_{inlet} [kPa]	Pearson 5	2.19-2.49	90.52 %
P_{2b} [kPa]	Log-Logistic	150-161	90.66 %
T_2 [°C]	Kumaraswamy	190-215	91.01 %
T_8 [°C]	Inaccurately represented, refer to Table 10		

The value ranges in Table 10 and Table 19, of the old and new data set, were compared and overlapping values were taken as the final test result range. The measured parameter's final value range is shown in Table 13, where it is used to validate flow results predicted by CFD simulations.

Appendix F: Flow Domain Assembly Clarification

The gas turbine main air casing, as well as relevant inner components, were reverse engineered to obtain CAD models of all the components. From the CAD models, the flow domains of all the components were created. By subtracting the inner flow domain from the domain of the main air casing, the flow domain required for CFD analysis was created. The components that form the inner domain assembly are shown in Figure 63 below.

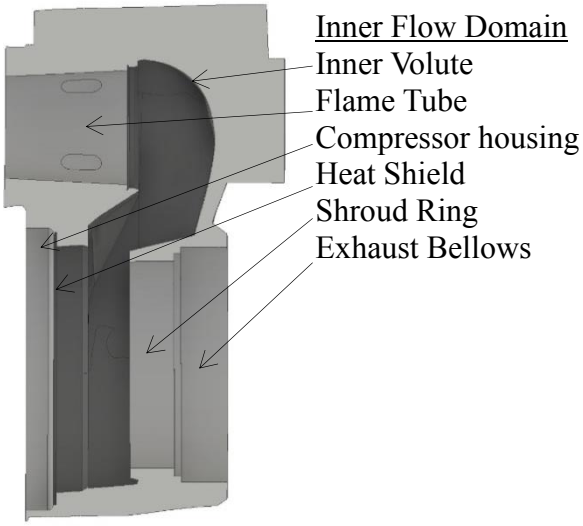

Figure 63: Inner flow domain clarification

The compressor housing, heat shield, shroud ring and exhaust bellows were created by measuring the geometries and simplifying the CAD models thereof. After creating the flow domain, the domain was meshed, as described in Section 8.2.1.

Appendix G: First Boundary Layer Height Calculation

The turbulent boundary layer is captured by implementing inflation control in the main air casing. The first cell layer height is calculated as follow (Cengel and Cimbala, 2010):

The Reynolds number is determined first by Equation 4.9. An average value for the density, ρ, and the dynamic viscosity, μ, was established from the results obtained in the Flownex simulations. The flow velocity, V, was derived from the Mach number obtained by the simulations of Luiten (2015). Assuming a fully developed turbulent profile, the first layer height of the boundary layer is determined by calculating the local friction coefficient:

$$\frac{c_f}{2} = \frac{0.0287}{Re_x{}^{0.2}} \qquad \text{G.1}$$

The friction velocity, u_τ, is then determined by:

$$u_\tau = \sqrt{\frac{c_f u_\infty{}^2}{2}} \qquad \text{G.2}$$

where the free stream velocity, u_∞, is assumed to be identical to the flow velocity, V. Assuming y^+ = 100, Equation G.3 can be re-written to determine the first layer height, y.

$$y^+ = \frac{y u_\tau}{\nu} \qquad \text{G.3}$$

The results obtained from the method discussed above are given in Table 20. The first layer height, y, was specified in the meshing application to create the necessary refinements along the boundary of the flow domain.

Table 20: Y-plus calculation results

Parameter	Value	Obtained from:
ρ [kg/m^3]	2.234	Flownex
μ [kg/ms]	1.86e^{-5}	Flownex
V [m/s]	31	Derived from (Luiten, 2015)
Re	1051351.04	Equation 4.9
c_f	0.003725	Equation G.1
u_τ	1.31259	Equation G.2
y [mm]	0.635	Equation G.3

Appendix H: Simulation Results

The results discussed in Chapter 9 are presented to some extent in this chapter. It contains the mesh independence of Design Case B and the flow results of Design Case A, implementing the new compressor.

H.1 Mesh Independence

The mesh independence of Design Case B was determined by comparing the mass flow rate to the number of elements in the mesh, for various mesh sizes. A graphical representation of the results is shown in Figure 64.

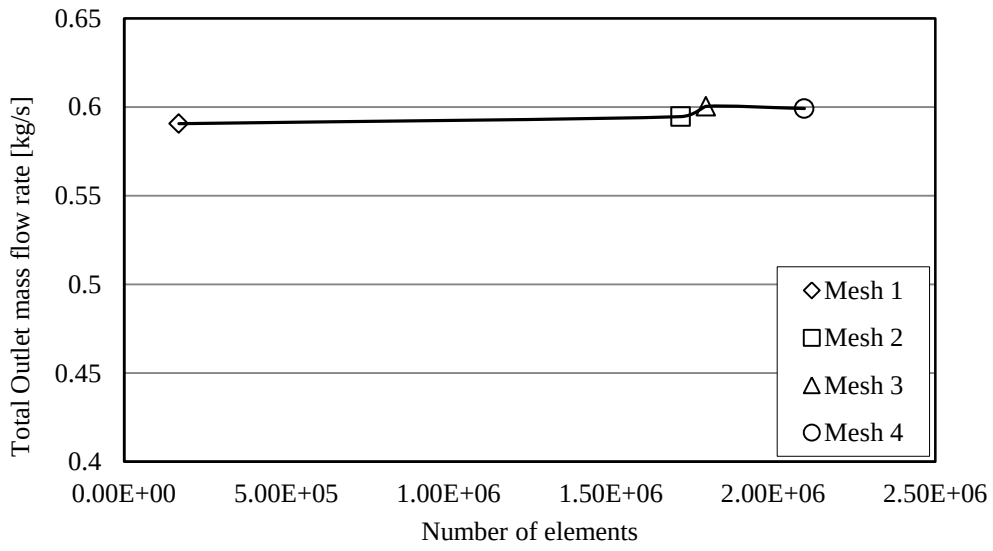

Figure 64: Mesh independence of Design Case B

As seen in Figure 64, further refinement in the mesh does not alter the value of the solution and mesh independence is thus achieved. Mesh 3 was used in subsequent flow predictions pertaining to Design Case B.

H.2 Flow Results of Design Case A

The flow predictions for Design Case A, implementing the new compressor, are presented hereafter. Design Case A was found to be less optimal for further analysis, but the results shown below could be used as a comparative, should the new compressor be manufactured and tested.

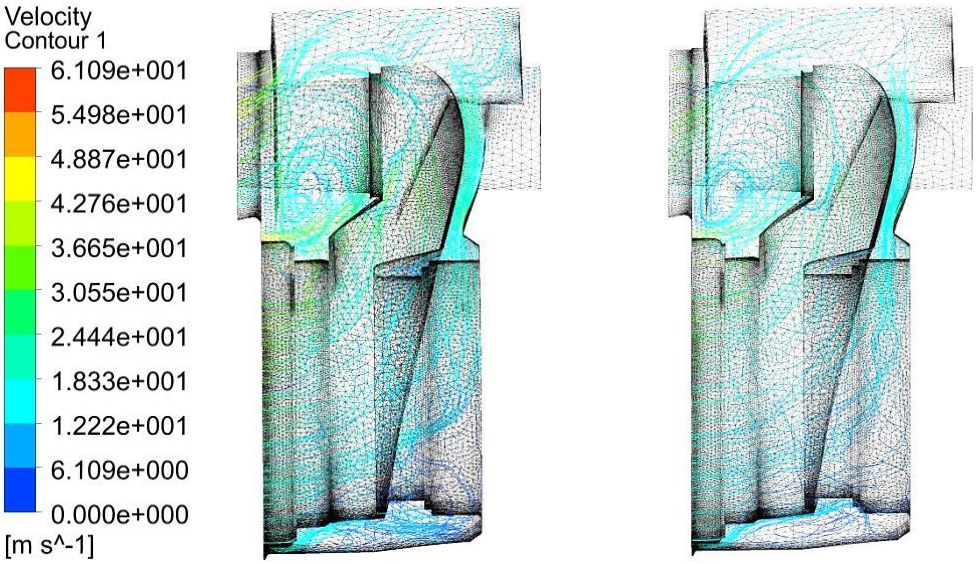

Figure 65: Comparison of the velocity streamlines between the old (a) and new compressor (b)

An increased inlet pressure reduces the velocity of the air flow inside the gas turbine, as shown in Figure 65 (b). This is confirmed by investigating the velocity contours, shown in Figure 66.

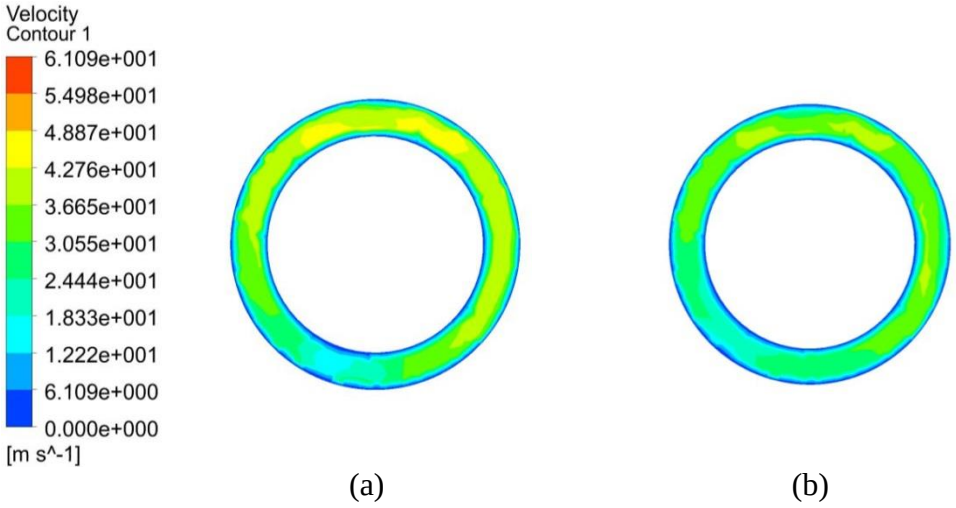

Figure 66: Comparison of the velocity contours between the old (a) and new compressor (b)

The pressure profile, shown in Figure 66 (b), seems fairly uniform in comparison to Figure 66 (a). This is largely due to the same scale being used for both cases. In contrast to this, the pressure profiles were scaled locally in each individual case, as shown in Figure 67.

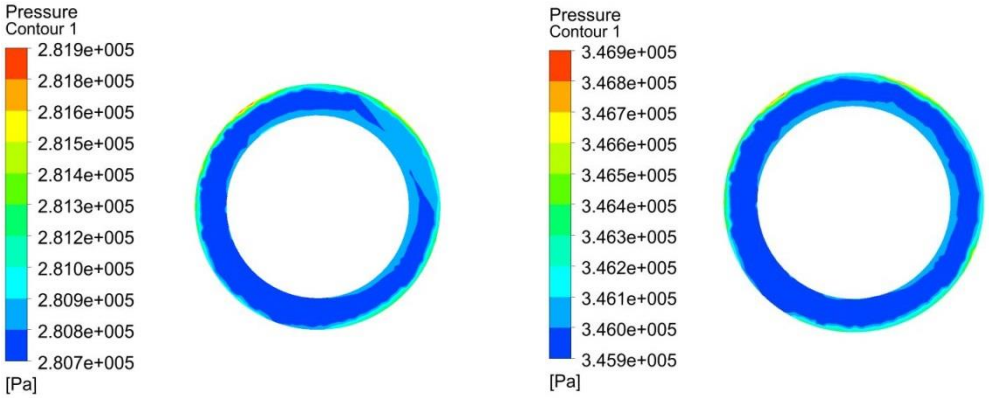

(a) (b)

Figure 67: Comparison of the pressure contours between the old (a) and new compressor (b)

The pressure profiles were uniform, as the pressure magnitudes did not vary over a large range, as shown in Figure 67 (a) and Figure 67 (b) respectively. These results were merely included in the current document, to enable future experimental comparison, should the new compressor be manufactured and installed on the current test bench.

Appendix I: Data Sheets of Commercial Gas Turbines

Extracts from the data sheets, for the gas turbines investigated in Chapter 11, are presented in this chapter. The Mercury 50 and Mars 100 turbines are sold by Solar Turbines Incorporated (2013) and the data sheets are presented below.

Mercury 50 data sheet extraction

Nominal Performance*

Output Power	4600 kWe
Heat Rate	9350 kJ/kWe-hr (8865 Btu/kWe-hr)
Exhaust Flow	63 700 kg/hr (140,400 lb/hr)
Exhaust Temperature	365°C (690°F)

ASSUMPTIONS

Nominal rating – per ISO
At 15°C (59°F), sea level
No inlet/exhaust losses
Relative humidity 60%
Natural gas fuel with
LHV = 35 MJ/Nm³ (940 Btu/scf)
No accessory losses
Engine efficiency: 38.5%
(measured at generator terminals)

Mars 100 data sheet extraction

Performance

Output Power	11 350 kWe
Heat Rate	10 935 kJ/kWe-hr (10,365 Btu/kWe-hr)
Exhaust Flow	153 245 kg/hr (337,850 lb/hr)
Exhaust Temp.	485°C (905 °F)

Both the full data sheets are available from Solar Turbines Incorporated (2013). The SGT-series gas turbines are produced by Siemens (2015), where both full data sheets are available. SGT-700 data sheet extraction:

Technical specifications

Overview

- Power generation: 31.21MW(e)
- Frequency: 50/60 Hz
- Electrical efficiency: 36.4 %
- Heat rate: 9,882 kJ/kWh (9,367 Btu/kWh)
- Turbine speed: 6,500 rpm
- Compressor pressure ratio: 18.6:1
- Exhaust gas flow: 94 kg/s (208lb/s)
- Exhaust temperature: 528° C (983° F)
- NO_x emissions (with DLE corrected to 15 % O_2 dry)
  - Gas fuel: ≤15 ppmV
  - Liquid fuel: ≤42 ppmV

SGT6 – 2000E data sheet extraction

Performance SGT-2000E series*

		SGT5-2000E	SGT6-2000E
Grid frequency	[Hz]	50	60
Power output	[MW]	166	112
Efficiency	[%]	34.7	33.9
Heat rate	[kJ/kWh]	10,375	10,619
Heat rate	[Btu/kWh]	9,834	10,066
Exhaust temperature	[°C/°F]	541/1,005.8	540/1,004
Exhaust mass flow	[kg/s]	525	365
Exhaust mass flow	[lb/s]	1,157	804
Pressure ratio		12	12.1
Length x width x height	[m]	10 x 12 x 7.5**	8.3 x 10 x 6.25**
Weight	[t]	234**	163**
Generator type			

* Gross values, standard design, ISO conditions, natural gas fuel ** Dimensions and weight incl. combustion chambers